

**ATYPICAL MASS SPECTROMETRY APPROACHES FOR UNKNOWN  
ANALYTE IDENTIFICATION IN COMPLEX MIXTURES**

by

**Leah F. Easterling**

**A Dissertation**

*Submitted to the Faculty of Purdue University*

*In Partial Fulfillment of the Requirements for the degree of*

**Doctor of Philosophy**



Department of Chemistry

West Lafayette, Indiana

August 2020

**THE PURDUE UNIVERSITY GRADUATE SCHOOL**  
**STATEMENT OF COMMITTEE APPROVAL**

**Dr. Mary Wirth, Chair**  
Department of Chemistry

**Dr. Garth Simpson**  
Department of Chemistry

**Dr. Julia Laskin**  
Department of Chemistry

**Dr. Christine Sahley**  
Department of Biology

**Approved by:**  
Dr. Christine A. Hrycyna

*To Dr. R. Mitch “Lambo” Lambert,  
For showing me that science is the best kind of magic.*

## ACKNOWLEDGMENTS

No thesis happens in a vacuum. Therefore, I would like to acknowledge the people without whom this thesis would not be what it is today. First, I would like to thank all my fellow graduate students who contributed to the work in this thesis, from helping train me to performing the chemical calculations to back up my theories: Dr. Mark Romanczyk, Laurance Cain, Kawthar Alzarieni, and Wanru Li. Without them, this research would have taken exponentially longer. Additionally, I'd like to thank my collaborators Jeremy Manheim, Swapnil Deshmukh, and Ravikiran Yerabola. Their work was instrumental to this research. Finally, I would like to thank my dearest friends here at graduate school: Rashmi Kumar, Jacob Milton, and Aria Bredt. They have been my sounding board and anchor throughout my entire graduate school experience.

I would also like to offer my sincerest thanks to my friends and family back home—especially Andrea Whaley-Palumbo and PJ Errera—for supporting me through some of the most trying and difficult years of my life. I would not have made it through graduate school without their unerring support and unconditional love. Last, but certainly not least, I would like to specially thank my partner Graham Akeson, who made sure I ate three meals every day while writing this thesis and who always believed in me, even when I no longer did.

# TABLE OF CONTENTS

LIST OF TABLES.....	8
LIST OF FIGURES.....	9
ABSTRACT.....	12
CHAPTER 1. INTRODUCTION.....	14
1.1 Introduction.....	14
1.2 Thesis Overview.....	14
1.3 References.....	16
CHAPTER 2. INSTRUMENTATION DESCRIPTIONS AND FUNDAMENTALS FOR THE LINEAR QUADRUPOLE ION TRAP MASS SPECTROMETER AND HYBRID ORBITRAP MASS SPECTROMETER.....	17
2.1 Introduction.....	17
2.2 Ionization.....	18
2.2.1 Electrospray Ionization.....	18
2.2.2 Atmospheric Pressure Chemical Ionization.....	20
2.3 Linear Quadrupole Ion Trap (LQIT) Mass Spectrometer.....	21
2.3.1 Ion Source and API Stack.....	22
2.3.2 Ion Optics.....	23
2.3.3 Linear Quadrupole Ion Trap.....	25
2.4 Functions of the Linear Quadrupole Ion Trap.....	26
2.4.1 Ion Trapping.....	26
2.4.2 Ion Isolation.....	30
2.4.3 Ion Excitation and Activation.....	31
2.4.4 Ion Ejection.....	33
2.5 Ion Detection.....	34
2.6 Orbitrap.....	35
2.6.1 Ion Injection.....	36
2.6.2 Motion in the Orbitrap.....	37
2.6.3 Ion detection in the Orbitrap.....	38
2.7 References.....	38

CHAPTER 3. FACTORS AFFECTING THE LIMIT OF DETECTION OF ION-MOLECULE REACTIONS IN MASS SPECTROMETRY .....	42
3.1 Introduction .....	42
3.2 Methods and Materials.....	43
3.2.1 Materials .....	43
3.2.2 Sample Preparation .....	43
3.2.3 Instrumentation .....	44
3.2.4 Calculating Reaction Efficiencies.....	47
3.2.5 Calculating Proton Affinities .....	49
3.3 Results and Discussion .....	51
3.3.1 Ion-molecule Reactions (MS <sup>2</sup> experiments) .....	51
3.3.2 Detection Limits.....	53
3.4 Limiting Factors .....	57
3.4.1 Ion Molecule Reaction Theory .....	58
3.4.2 Analyte Proton Affinity .....	59
3.4.3 Reaction Efficiency .....	60
3.5 Ion-molecule Reactions Followed by CAD (MS <sup>3</sup> Experiments) .....	61
3.6 Aberrant Result.....	65
3.7 Conclusions and Future Outlook.....	66
3.8 References.....	67
CHAPTER 4. A STUDY OF ELECTROSPRAY IONIZATION-INDUCED OXIDATION OF SULFUR-CONTAINING COMPOUNDS .....	72
4.1 Introduction .....	72
4.2 Materials and Methods.....	74
4.3 Results and Discussion .....	76
4.3.1 Reactions of Ethanethiol During Atypical ESI.....	76
4.3.2 Mechanism of Thiol Ion Ozonolysis .....	80
4.3.3 Trends in Sulfur-Compound Oxidation.....	83
4.3.4 Controlling the extent of oxidation.....	88
4.4 Conclusions .....	96
4.5 References.....	97

CHAPTER 5. ANALYTICAL CHARACTERIZATION OF SELENIUM AND TELLURIUM DISSOLVED IN AMINE-THIOL SOLVENT SYSTEMS .....	101
5.1 Introduction .....	101
5.2 Experimental.....	103
5.2.1 Materials .....	103
5.2.2 Ink Generation.....	104
5.2.3 Electrospray Ionization Mass Spectrometry Experiments .....	105
5.2.4 Other Spectroscopic Characterization .....	108
5.3 Analysis of Se and Te Solutions in Monoamine- and Diamine-Thiol Solvent Systems .	109
5.3.1 Selenium Dissolution in Monoamine vs Diamine Solutions .....	109
5.3.2 Tellurium Dissolution in Diamine Solutions .....	117
5.3.3 Co-dissolution of Selenium and Tellurium .....	120
5.4 Effect of Thiol Concentration on Chalcogen Dissolution .....	125
5.4.1 Effect of Thiol Concentration on Selenium Dissolution .....	126
5.4.2 Effect of Thiol Concentration on Te Dissolution .....	133
5.4.3 Effect of Thiol Concentration on Se Te Codissolution .....	134
5.5 Using New Understanding to Guide Alloy Synthesis.....	138
5.6 Conclusions .....	139
5.7 References.....	140
VITA.....	145
PUBLICATIONS .....	147

## LIST OF TABLES

Table 3.1 Model compounds (m/z values of protonated compounds in parenthesis), detected reaction products (m/z values) and the corresponding measured reaction efficiencies. ....	52
Table 3.2 Model compounds (m/z), the calculated proton affinities for the most basic site, and the measured detection limits.....	57
Table 3.3 The TDMAB ion-molecule reaction detection limits and the MS <sup>3</sup> (product ion isolation and fragmentation) detection limits for model mixture one. <sup>a</sup> .....	65
Table 5.1 Elemental composition of ions detected using (-) ESI-MS for Se in BA-ET and Se in EN-ET. ....	116
Table 5.2 Elemental composition of ions detected using (-) ESI-MS for Te solutions in EN-ET. ....	120
Table 5.3 Elemental composition of ions detected using (-) ESI-MS for Se-Te solutions in BA-ET and in EN-ET. ....	124
Table 5.4 Elemental composition of ions detected using (-) ESI-MS for Se solutions in BA-ET and EN-ET with minimum thiol used for dissolution. ....	133
Table 5.5 Elemental composition of ions detected using (-) ESI-MS for Se-Te solutions in BA-ET with a thiol:Se molar ratio of 0.3. ....	135
Table 5.6 Elemental composition of ions detected using (-) ESI-MS for Se-Te solutions in BA-ET with a thiol:Se molar ratio of 0.3. ....	138

## LIST OF FIGURES

Figure 2.1 A schematic of electrospray ionization (ESI) and an ESI probe. ....	19
Figure 2.2 An example of the types of ion-molecule reactions that lead to analyte cation formation in APCI positive ion mode. ....	21
Figure 2.3 Simplified schematic of the Thermo Scientific Linear Quadrupole Ion Trap mass spectrometer. ....	22
Figure 2.4 Standard DC potentials of various components within the Thermo Scientific Linear Quadrupole Ion Trap mass spectrometer. ....	25
Figure 2.5 A schematic of the ion trap. The ion trap consists of four hyperbolic rods, each divided in three different sections: front, center, and back. ....	26
Figure 2.6 Simplified Mathieu stability diagram for a linear quadrupole ion trap. ....	29
Figure 2.7 Mathieu stability diagrams illustrating the process of isolating ions of a single $m/z$ within the linear ion trap. ....	31
Figure 2.8 Simplified schematic of collision activated dissociation as shown on a Mathieu stability diagram. ....	33
Figure 2.9 Location and simplified schematic of one detector in the Thermo Scientific Linear Quadrupole Ion Trap mass spectrometer. ....	35
Figure 2.10 Simplified schematic of the Thermo Scientific LQIT/Orbitrap hybrid instrument. ...	36
Figure 3.1 HPLC extracted ion chromatogram of model mixture one at a concentration of 500 nM. ....	45
Figure 3.2 Calibration curve of albendazole sulfoxide, showing the correlation between the mass spectrometer instrument response (in normalized level “NL”) and the analyte concentration. ....	46
Figure 3.3 Generated graph of the log of the relative abundance of albendazole sulfoxide ions ( $m/z$ 282), protonated TDMAB ( $m/z$ 144), and albendazole reaction products ( $m/z$ 327, 380) as a function of time. ....	48
Figure 3.4 A) PA values of the most basic sites in omeprazole (shown as protonated) calculated at the B3LYP/6-31G++(d,p) level of theory. ....	50
Figure 3.5 On the following page, there are four sets of HPLC chromatograms (top of each spectra collection) and MS spectrum (bottom of each spectra collection) for albendazole sulfoxide. ....	54
Figure 3.6 Typical extracted ion current HPLC chromatogram and a corresponding set of mass spectra used to determine the limits of detection for sulindac. ....	56
Figure 3.7 Example of a Brauman double-well potential energy surface for an exothermic ion-molecule reaction. ....	58

Figure 3.8 MS <sup>2</sup> and MS <sup>3</sup> spectra for albendazole sulfoxide (m/z 282) at a concentration of 500 nM. .....	63
Figure 4.1 Negative mode ESI (top) and positive mode ESI (bottom) mass spectra of pure ethanethiol. ....	77
Figure 4.2 Photograph of the plasma discharge during an ethanethiol experiment with a negative mode ESI voltage of 3 kV and an ethanethiol flow rate of 10 μL/min. ....	78
Figure 4.3 Comparison of negative ESI (top) and APCI (bottom) mass spectra of pure ethanethiol (deprotonated ethanethiol has m/z of 61). ....	80
Figure 4.4 Previously proposed mechanism for the reaction between ozone and a negatively charged sulfur, based on Wang et al. and Williams et al. <sup>3,28</sup> .....	81
Figure 4.5: Potential energy surfaces (enthalpies in kcal/mol) for the formation of a) ethanethiol and ozone; b: transition state; c: product before CAD; d: final products after CAD. ....	83
Figure 4.6 Low resolution (-)ESI MS spectra measured for neat (A) ethanethiol, (B) propanethiol, (C) ethanedithiol, (D) tetrahydrothiophene, and (E) cysteine in water. ....	84
Figure 4.7 Low-resolution atypical condition (-)ESI mass spectrum of ethanethiol taken with (a) oxygen and (b) nitrogen as the sheath and auxiliary gas. ....	89
Figure 4.8 Relative abundances of oxygen-containing ions when analyzed by ESI using (a) nitrogen and (b) oxygen gas. ....	90
Figure 4.9 Relative abundances of oxygen containing and non-oxygen containing ions as a function of the syringe injection flow rate of pure ethanethiol in (-) ESI. ....	92
Figure 4.10 (-)ESI mass spectra of pure ethanethiol at sheath/auxiliary flow rates of (top) 20/ 10, (middle) 40/20, and (bottom) 70/35. ....	93
Figure 4.11 Low-resolution atypical condition (-)ESI mass spectrum of ethanethiol dissolved in methanol (top) and acetonitrile (bottom). ....	94
Figure 4.12 Low-resolution atypical condition (+)ESI mass spectrum of ethanethiol dissolved in methanol (top) and acetonitrile (bottom). ....	96
Figure 5.1 Schematic of the syringe setup used for the introduction of the solutions into the mass spectrometer. ....	105
Figure 5.2 Overlay of the experimental (solid blue line) and theoretical (dashed orange line) isotopic abundance for the HSe <sub>4</sub> ion. ....	107
Figure 5.3 Fragmentation pattern of the HSe <sub>4</sub> ion collected from a sample of 10 mM Se in 1:1 (v/v) BA:ET. ....	108
Figure 5.4 Raman spectrum of Se in BA-ET (top) and EN-ET (bottom). ....	110
Figure 5.5 NMR Spectrum of Se in BA-ET. Only the area of interest (from 0.6-3 ppm) is shown. ....	112

Figure 5.6 NMR Spectrum of Se in EN-ET. Only the area of interest (from 1-3 ppm) is shown. .....	113
Figure 5.7 XAS spectra for Se in BA-ET (black trace) and EN-ET (red trace). ....	114
Figure 5.8 (-)ESI-MS spectra of Se in BA-ET (top) and EN-ET (bottom).....	115
Figure 5.9 Raman spectra of Tellurium powder (black trace) and Tellurium in EN-ET (red trace). .....	118
Figure 5.10 (-)ESI-MS spectrum of tellurium in EN-ET. ....	119
Figure 5.11 Raman spectra for the co-dissolved Se and Te in both BA-ET (top red trace) and EN- ET (bottom black trace).....	122
Figure 5.12 (-)ESI-MS spectra of SeTe dissolved in BA-ET (top) and in EN-ET (bottom). ....	123
Figure 5.13 Raman spectra of Se in BA-ET at four different ET:Se mol ratios. ....	127
Figure 5.14 (-)ESI-MS spectra of Se in BA-ET. ....	129
Figure 5.15 Raman spectra of Se in BA-ET at four different ET:Se mol ratios. ....	131
Figure 5.16 (-)ESI-MS spectra of Se in EN-ET.....	132
Figure 5.17 (-)ESI-MS spectra of SeTe in BA-ET. ....	135
Figure 5.18 (-)ESI-MS spectra of SeTe in EN-ET at two different concentrations of thiol. ....	137

## ABSTRACT

This dissertation details three studies which utilize nontraditional applications of electrospray ionization mass spectrometry. The first study explores and discusses the limitations of identifying unknown drug metabolites using ion-molecule reactions performed inside a mass spectrometer and coupled with high performance liquid chromatography. Ultimately, it was concluded that some highly-efficient, MS<sup>2</sup> ion-molecule reactions coupled with some drug metabolites would be sufficiently sensitive for *in vivo* drug metabolism studies. However, this study also concluded that the rate of false-positives and false-negatives may be higher than previous publications suggest.

The next study analyzed sulfur-containing compounds under atypical negative-mode electrospray ionization mass spectrometry conditions. After noting that low analyte flow rates during electrospray ionization experiments on ethanethiol resulted in significant oxygen incorporation, the aim of this study was to understand the chemistry behind the oxygen incorporation and search for ways to experimentally limit the degree of oxygen inclusion. The atypical conditions were ultimately shown to induce significant ozonolysis and other oxidation reactions. Ultimately, only the use of high flow rates or switching to a different ionization technique were successful in mitigating the oxidation product formation. A new reaction mechanism for the oxidation of ethanethiol with ozone was proposed. Quantum chemical calculations were used to support the mechanism.

Finally, electrospray ionization mass spectrometry was used to analyze mixtures of selenium and/or tellurium in amine-thiol solvent systems. Selenium and tellurium are essential components in many thin film solar cells and other photovoltaics and amine-thiol solvent systems have been identified as a key solution processing strategy for synthesizing selenium and tellurium thin films. However, the reaction between selenium/tellurium and the amine-thiol solvent system is poorly understood and requires detailed study before large-scale industrial synthesis can be achieved. In this study, the dissolution mechanisms for selenium and tellurium in two different amine-thiol solvent systems were explored and discussed. The role of the basicity of the amine, the relative concentration of the thiol, and the presence of co-dissolved chalcogens were all studied and used to propose dissolution mechanisms. The results of the experiments were used to control the

synthesis of lead-selenium-tellurium alloy nanoparticles and could inform further studies on controlling metal chalcogenide synthesis through the appropriate choice of amine-thiol solvents.

# CHAPTER 1. INTRODUCTION

## 1.1 Introduction

Mass spectrometry has long been used to analyze both organic and inorganic compounds. In particular, mass spectrometry is often used to identify the chemical formula and the chemical structure of unknown analytes. When optimized properly, ionization methods produce just one molecular ion peak ( $m/z$  value) for every component in a mixture. Because of this, mass spectrometry has emerged as one of the most powerful instrumental techniques for identifying the individual components in complex mixtures. It's current applications in complex mixture analysis include petroleomics,<sup>1</sup> forensics,<sup>2</sup> and pharmaceutical research<sup>3</sup> amongst others.

When analyzing complex mixtures, a two-pronged approach is often used. First, high resolution mass spectrometry techniques, including the recently-developed hybrid Orbitrap instrument, are used to determine the elemental composition of each unknown analyte. This can be accomplished because these high-resolution measurements are so precise that the elemental composition of each unknown analyte can be easily derived from its corresponding  $m/z$  value. However, the elemental composition cannot be used alone to determine the structure of an unknown compound. Therefore, a second approach is used to identify or posit the structure of each compound in the mixture. The most common technique for accomplishing this is collision activated dissociation (CAD), which reproducibly fragments the individual ions, producing ion fragmentation patterns that can be used to reconstruct the possible structures or can be matched against the fragmentation patterns of pure standards for positive identification.

However, some analytes and mixtures are particularly complex or otherwise ill-suited to this traditional two-pronged mass spectrometric work flow. Other types of mixtures have not been extensively studied using this approach and their performance is not yet rigorously verified. This thesis focuses on three such cases.

## 1.2 Thesis Overview

The research in this thesis focuses on two mixtures and one set of pure compounds analyzed by a linear quadrupole ion trap mass spectrometer or by a hybrid linear quadrupole ion trap/Orbitrap mass spectrometer. Each mixture or set of compounds represents a deviation from

the traditional two-pronged mass spectrometric identification approach. The theory behind the deviations and the techniques developed to analyze the mixtures are presented here.

Chapter 2 describes the theory and operation of the mass spectrometers used in this thesis: the Thermo Scientific Linear Quadrupole Ion Trap Mass Spectrometer (LTQ) and the Thermo Scientific high-resolution hybrid LTQ/Orbitrap Mass Spectrometer. Additionally, the theory behind the ionization methods used in this thesis (electrospray ionization and atmospheric chemical ionization) are also presented in this chapter.

Chapter 3 discusses a study used to determine the limit of detection of ion molecule reactions when coupled with tandem mass spectrometry. The use of ion molecule reactions conducted inside of mass spectrometers has gained recent popularity for identifying functional groups in unidentified pharmaceutical metabolites. While an unconventional mass spectrometric method, the development of these functional group identification reaction has been met with some success. Currently these reactions are being put forth as a fast, cheaper alternative to traditional pharmaceutical metabolite identification techniques. However, it has not been previously established that these ion molecule reactions are sensitive and reproducible enough to be used to identify unknown metabolites at physiologically relevant concentrations. This chapter details the research used to determine the limit of detection for several ion molecule reactions and discusses the factors which affect the limit of detection of these reactions. A version of this chapter is published in the journal of Analytical Chemistry published by the American Chemical Society. This work was conducted with the help of Rashmi Kumar, Ravikiran Yerabolu, and Kawthar Alzarieni from Purdue University.

Chapter 4 details a study of the products produced when organic sulfur-containing compounds are analyzed under oxidizing electrospray ionization conditions. Sulfur compounds are often found in petroleum and pharmaceutical applications, but their behavior when analyzed using electrospray ionization is not rigorously understood. It has been assumed that sulfur-containing compounds such as thiols will produce one mass spectral peak ( $m/z$  value) and therefore can be analyzed using the aforementioned two-pronged approach. However, under oxidizing conditions, the electrospray ionization source not only functions as an electrochemical cell, but also produced ozone at the tip of the electrospray needle. The oxidizing environment and the ozone lead to highly oxidized sulfur species and numerous reaction products for each individual sulfur-containing compound. The implications of this fundamental research on analyzing complex

mixtures that contain organosulfur compounds are discussed. This work was done with the assistance of graduate students Jeremy Manheim, Wanru Li, and Jacob Milton from Purdue University.

Chapter 5 discusses the analysis of complex mixtures of metallic compounds and organometallic compounds by electrospray ionization high-resolution mass spectrometry and additional techniques. Metallic and organometallic compounds are not traditionally analyzed by organic mass spectrometers. Additionally, these mixtures were made using a unique solvent composed of amines and thiols, which is atypical for electrospray ionization. These mixtures were analyzed using both high-resolution mass spectrometric measurements and collision activated dissociation to identify compounds in the mixtures. The identified compounds were then used to posit the structural changes that occur when these solutions are made or altered. A version of this chapter is published in the journal of Inorganic Chemistry published by the American Chemical Society. This work was completed in collaboration with Swapnil Deshmukh, Jeremy Manheim, Nicole LiBretto, Kyle Weideman, and Jeffrey Miller from Purdue University.

### 1.3 References

1. Marshall, A.G.; Rodgers, R.P. Petroleomics: Chemistry of the Underworld. *Proc. Natl. Acad. Sci. USA*. **2008**, *105* (47), 18090 – 18095.
2. Maurer, H.H. Mass Spectrometry for Research and Application in Therapeutic Drug Monitoring or Clinical and Forensic Toxicology. *Ther. Drug Monit.* **2018**, *40* (4), 389 – 393.
3. Belas, F.J.; Blair, I.A. Mass Spectrometry in Pharmaceutical Analysis. *J. Liposome Res.* **2001**, *11* (4), 309 – 342.

## **CHAPTER 2. INSTRUMENTATION DESCRIPTIONS AND FUNDAMENTALS FOR THE LINEAR QUADRUPOLE ION TRAP MASS SPECTROMETER AND HYBRID ORBITRAP MASS SPECTROMETER**

### **2.1 Introduction**

Mass spectrometers are powerful analytical instruments used in a variety of fields, from forensics<sup>1</sup> to pharmaceuticals<sup>2</sup> to archaeology.<sup>3</sup> The field of mass spectrometry is therefore quite diverse and covers a wide range of instruments with significant variations in design, use, and application. However, all mass spectrometers operate along the same general principles, and any mass spectrometry experiment typically requires the same three general steps. First, the analytes being studied must be transformed to gas-phase ions. Second, the ions must be separated, usually in time or in space, by their mass-to-charge ratio ( $m/z$ ). Finally, each individual ion must be detected and transformed to a measurable signal with both the associated  $m/z$  of the ion and the corresponding signal intensity (how many individual ions of the given  $m/z$  were measured). A mass spectrum is therefore a collection of these measurable signals, with the mass-to-charge ratio along the x-axis and the relative intensity along the y-axis.

One major difference in instrumental design and operation is the ability to add additional steps to the mass spectrometry experiment between separating the ions by their  $m/z$  and detecting them. Some instruments are able to perform ion-molecule reactions inside the mass spectrometer during this time.<sup>4,5</sup> Others may fragment the ions before detection or contain elaborate means of removing unwanted ions,<sup>6</sup> while some others have no inherent ability to do anything additional.<sup>7</sup> The two instruments used in this dissertation are the linear quadrupole ion trap (LQIT) fitted with a home-built manifold for performing ion-molecule reactions and a linear quadrupole ion trap coupled to an orbitrap detector (LQIT/Orbitrap) for high-resolution measurements. This chapter describes the underlying theory and operation of the ionization methods used, the LQIT, and the orbitrap high-resolution detector. The theory of ion-molecule reactions will be discussed in further detail in chapter 3.

## **2.2 Ionization**

The first step in a mass spectrometry experiment is to transform the analytes into gas-phase ions. In early mass spectrometer designs, electron impact (EI)<sup>8</sup> and chemical ionization (CI)<sup>9</sup> were for ionization, but were limited to gas-phase analytes. Therefore, for less volatile analytes, thermal heating was therefore often required prior to using these ionization techniques, limiting the techniques to analytes that were thermally stable and at least minimally volatile.<sup>10</sup> Since those early days, the number of available ionization techniques has greatly expanded, and techniques now exist for analytes in any phase.<sup>11-14</sup> The work performed for this dissertation focuses on analytes in solution, for which electrospray ionization (ESI) and atmospheric pressure chemical ionization (APCI) were used. These two techniques are therefore described in the following sections.

### **2.2.1 Electrospray Ionization**

Electrospray ionization (ESI) is a modern atmospheric pressure ionization technique used to evaporate analytes in solution and then ionize the resulting gas-phase molecules. This technique is considered "soft," meaning that it is suitable for thermally labile compounds and does not generally induce extensive fragmentation during the ionization process.<sup>15,16</sup> However, ESI is generally only suited for analytes that are at least moderately polar, since it usually involves protonating or deprotonating the analyte. Therefore, the analyte must have a sufficiently basic site for protonation or acidic site for deprotonation.<sup>17</sup> Due to these limitations, ESI is traditionally used for pharmaceutical and biological applications, where acidic and basic sites are fairly common.

While the mechanism of ESI has been extensively studied, there is no one unified theory for how ESI ionizes and evaporates analyte molecules. However, it is generally agreed that there are three main steps in the evaporation/ionization of ESI. First, charged droplets are formed at the tip of a highly-charged metal capillary, called the ESI capillary tip or needle. Second, the droplets begin to evaporate, producing highly charged nanodroplets. Finally, gas-phase analyte ions are generated from these charged nanodroplets. A schematic of these steps is included below.

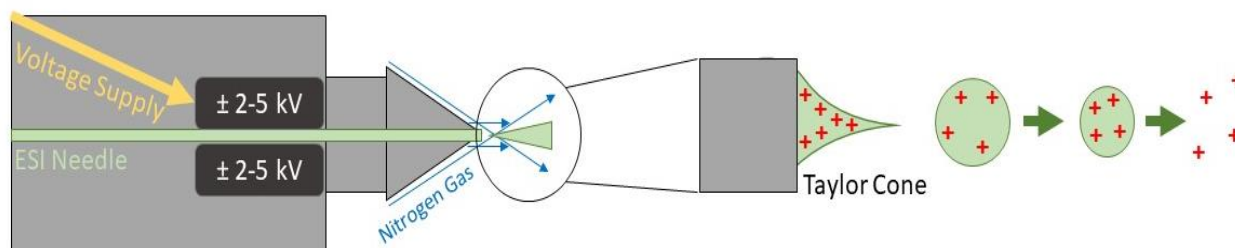


Figure 2.1 A schematic of electrospray ionization (ESI) and an ESI probe. The ESI needle delivers the analyte solution. A high voltage is applied to the end of the ESI needle. Nitrogen gas (shown as blue arrows) flows around the head of the ESI probe (auxiliary gas) and in a cylinder around the tip of the ESI needle (sheath gas). The analyte solution is charged at the tip of the needle, resulting in a charged Taylor cone (inset). Small charged droplets (not drawn to scale) emerge from the tip of the Taylor cone. As the solvent evaporates, the droplets shrink until they are so small that charged analytes (+) are produced. These charged analytes then enter the mass spectrometer for analysis.

ESI requires a steady stream of charged droplets. To accomplish this, the analyte must be a liquid or dissolved in a liquid or solution. Typically, acetonitrile, methanol, and water are used, alone or in combination, to dissolve the analyte.<sup>18</sup> The analyte solution is then introduced to the ESI probe, either through liquid chromatography or injected using a syringe pump. The analyte solution flows through the ESI capillary, the tip of which is highly charged (usually  $\pm 2\text{-}5\text{ kV}$ ).<sup>16</sup> To generate positive ions, a positive charge is applied to the tip, while negative ions are generated by applying a negative charge. Since the orifice of the mass spectrometer is held at ground, the charged ESI capillary induces an electric field between the ESI probe and the mass spectrometer. As the solution flows through this highly charged capillary, the induced electric field charges the surface of the solution, resulting in an elongated cone of liquid at the tip of the capillary called a Taylor cone, from which small droplets are then formed.<sup>19</sup> Nitrogen gas is often used to assist in nebulizing the solution spray into a fine cohesive mist and to assist in solvent evaporation.<sup>20</sup> As the droplets evaporate and become smaller, the charges on each droplet become increasingly dense. At a certain charge density, called the Rayleigh limit, the repulsion between the charges overcomes the surface tension of the droplet and the droplet undergoes jet fission to produce numerous smaller droplets.<sup>21-23</sup> This process of evaporation and jet fission is repeated numerous times until charged nanodroplets are formed. Collectively, the continuous evaporation and fission of the droplets is called a Coulombic explosion.<sup>23</sup>

While the formation of the charged nanodroplets is well-established in the literature, there is

still considerable debate concerning how the analyte ions are formed from these charged nanodroplets.<sup>24</sup> Three main theoretical models exist: the charge residue model, the ion evaporation model, and the chain ejection model. In the charge residue model, by the time the charged droplets evaporate down to a nanodroplet, the nanodroplet contains just one analyte molecule. As the final solvent evaporates from the nanodroplet, the charge is transferred to the analyte molecule, producing the final analyte ion.<sup>25</sup> It is thought that this model best describes the ionization of large and/or multiply-charged ions, most notably proteins.<sup>26</sup> The ion evaporation model posits that the electrostatic repulsion on the surface of the charged nanodroplets is high enough to cause the spontaneous emission of solvated analyte ions, which then evaporate to dryness.<sup>27</sup> This model is believed to best fit the behavior of small, singly-charged analytes, including organic compounds such as pharmaceuticals and drug metabolites.<sup>28</sup> Finally, the chain ejection model is thought to explain the behavior of unfolded proteins. As the unfolded proteins are solvated in ever-shrinking nanodroplets, the hydrophobic portions of the proteins are less favorably solvated in the highly charged, hydrophilic droplet. At a given point, a hydrophobic end will be ejected from the droplet, bringing the rest of the protein with it.<sup>29</sup>

### **2.2.2 Atmospheric Pressure Chemical Ionization**

Like electrospray ionization, atmospheric pressure chemical ionization (APCI) is a "soft" ionization technique that usually results in a protonated analyte ion in positive ion mode or a deprotonated analyte ion in negative ion mode.<sup>30</sup> Unlike ESI, APCI is a gas-phase technique that is better suited to thermally stable analytes with nonpolar or semi-polar characteristics.<sup>30, 31</sup> In APCI, the analyte begins in the form of a solution which is then passed through a heated fused silica transfer capillary. Nitrogen gas flows around the capillary to help keep the flow concerted and aid in desolvation. As the solution passes through the capillary, ceramic heaters and the nitrogen gas vaporize the sample to gas-phase analyte and solvent molecules. The nitrogen gas then pushes these molecules towards a corona discharge needle.<sup>32</sup> This needle is highly charged (usually 2-5 kV) and is responsible for inducing ionization.<sup>33</sup> The ionization is thought to be a multi-step process and involve ion-molecule reactions.<sup>34</sup> First, the corona discharge needle ionizes the ambient gas within the ion source, which is mostly nitrogen, to form primary nitrogen ions. These primary ions then proceed to react with other species in the ion source, the most abundant of which is the solvent molecules. In a series of ion-molecule reactions, numerous types of

secondary ions are formed. Finally, the secondary ions react with the analyte molecules to produce analyte ions. These reactions are usually proton transfer reactions, resulting in a pseudomolecular ion. The figure below shows one possible series of reactions at the corona discharge needle which could result in the production of a positively-charged analyte ion.

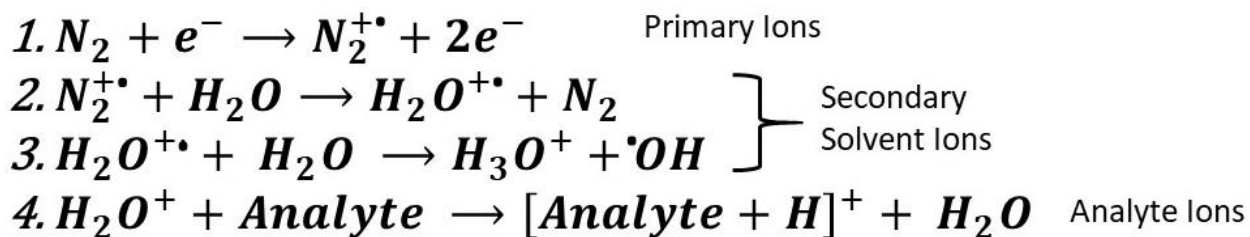


Figure 2.2 An example of the types of ion-molecule reactions that lead to analyte cation formation in APCI positive ion mode. For this simplified example, it is assumed that nitrogen is the primary constituent of the atmosphere inside the source and that water is the solvent used to dissolve the analyte. In the first step, nitrogen gas is ionized at the corona discharge needle and forms radical cations. These radical nitrogen cations then react with water (the next most abundant species present at the needle) to produce the radical cation of water and regenerate neutral nitrogen. The radical cation water can then further react with water to produce protonated water and a hydroxy radical. The protonated water can then react with the analyte in a proton-transfer reaction to produce protonated analyte ions and water.

### 2.3 Linear Quadrupole Ion Trap (LQIT) Mass Spectrometer

Since the invention of the 3D quadrupole ion trap (Paul Trap), quadrupole ion traps have been used extensively both as traditional mass spectrometers and to study chemical reactions and gas-phase ion chemistry.<sup>35</sup> Quadrupole ion traps is a mass spectrometer capable of trapping ions in space and performing additional reactions or fragmentations prior to ion detection. The linear quadrupole ion trap (LQIT) is now much more common than the original 3D trap, in large part due to its increased sensitivity and ion storage capacity.

The LQIT used for the research in this dissertation was the Thermo Scientific LQIT, the schematic of which is presented below. The LQIT is made of five general sections: the ion source, the API stack, the ion optics, the ion trap itself, and the detector. The ion source is located at the front of the instrument and contains the ionization probe (in this case ESI or APCI). For detailed information on the ionization techniques used for this dissertation, see sections 2.2.1 and 2.2.2. This ion source operates at atmospheric pressure (760 Torr). The next region is the API stack,

which is operated at 1 Torr and serves as a region for ion transfer and as a vacuum baffle between the atmospheric pressure of the ion source and the high vacuum of the ion optics and ion trap in the mass spectrometer. The low pressure is achieved through two Edwards E2M30 rotary-vane mechanical pumps. The next region is the ion optics region, in which the ion beam is guided into the ion trap. The pressure in this region decreases from 0.5 Torr down to  $1 \times 10^{-5}$  Torr, which is achieved using a triple ported Leybold TW220/150/15S turbomolecular pump. The final section of the LQIT is the ion trap region, where ion trapping, manipulation, and detection occur. This region is held at a pressure of  $1 \times 10^{-5}$  Torr and is evacuated using the turbomolecular pump's third port. Pressures within the instrument can be monitored by the user in real time via digital readouts from a convection pressure gauge (for the ion source), an ion gauge (for regions between the source and the gate lens) and a compact cold cathode inverted magnetron gauge (for the ion trap region behind the gate lens).

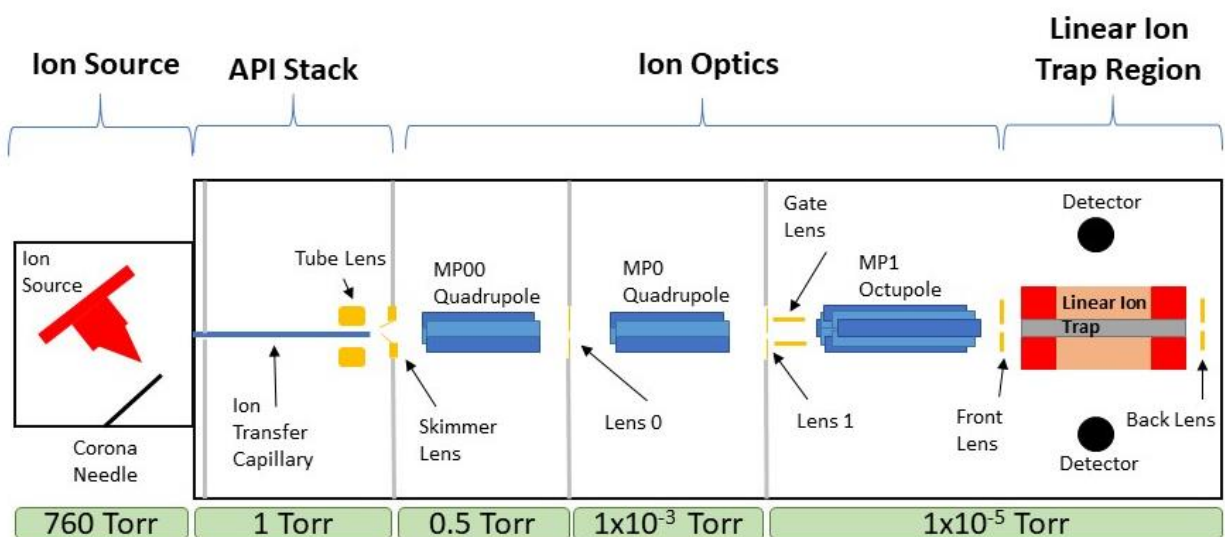


Figure 2.3 Simplified schematic of the Thermo Scientific Linear Quadrupole Ion Trap mass spectrometer. Important components are labeled. The operating pressures of the various sections are labeled in green. The four different regions of the mass spectrometer are labeled in black above the figure.

### 2.3.1 Ion Source and API Stack

The ion source contains the ionization source for the mass spectrometer. While the Thermo LQIT can be equipped with several different ionization sources, the sources used for this

dissertation were ESI and APCI. For further details on ESI and APCI, please see sections 2.2.1 and 2.2.2, respectively. The ion source is kept at atmospheric pressure and the ionization is achieved by applying a high voltage (usually  $\pm 2\text{-}5$  kV) to the spray needle of the ion source, through which the analyte solution flows. The orifice of the mass spectrometer is kept at electrical ground. The high voltage of the source and the grounded orifice create an electric field which draws the ions and charged droplets generated in the ion source into the mass spectrometer. A sweep cone surrounds the orifice. When necessary, a sweep gas of dry nitrogen is blown out from the sweep cone and around the orifice to help prevent neutral molecules from entering the mass spectrometer.

After entering through the orifice, the ions are located inside the API stack region of the mass spectrometer. Ions enter through the ion transfer capillary, which is heated to remove excess solvent from the ions. The lower pressure inside the API stack (approximately 1 Torr) creates a pressure gradient that helps guide the ions through the API stack and deeper into the mass spectrometer. A DC voltage applied to the ion transfer capillary creates a voltage gradient that also guides the ions down the transfer tube and out the tube lens. Directly after the tube lens is a skimmer lens, which is located slightly off-center and higher than the tube lens. A voltage is applied to the tube lens to bend the ion beam upward and through the skimmer lens. Any neutral molecules that have managed to make it this far into the instrument are therefore extinguished because their trajectory is not bent by the tube lens voltage and their path remains straight, putting them on a collision course with the inner walls of the mass spectrometer.

### **2.3.2 Ion Optics**

The ion optics region of the mass spectrometer is a series of four lenses and three multipoles meant to focus and guide the ions from the API stack to the ion trap.<sup>36</sup> The four lenses are lens 0, lens 1, the gate lens, and the front lens. The multipoles located in the ion optics region include two quadrupoles, Q00 and Q0, and one octopole, Q1. As ions move from Q00 to Q0 and finally to Q1, the pressure within the instrument decreases from approximately 0.5 Torr to  $1 \times 10^{-3}$  Torr to  $1 \times 10^{-5}$  Torr. Between each multipole, there is a lens. The lenses act both as vacuum baffles between the different multipoles and as ion focusers, helping to refocus the ion beam into a cohesive stream for proper ion transmission. Lens 0 is located between Q00 and Q0; lens 1 and the gate lens are located between Q0 and Q1, and the front lens is located between Q1 and the ion trap.

To transmit ions effectively through the ion optics, a radio frequency (RF) voltage is applied to the multipoles. The RF voltage applied to each rod in a given multipole are always of the same amplitude. However, adjacent rods will always have an RF frequency exactly  $180^\circ$  out of phase. For quadrupoles Q00 and Q0, there will always therefore be one pair of rods with a positive polarity and one pair with a negative polarity. The phase oscillates, such that the polarity on a given set of rods is continually switching, generating a quadrupolar field. In the case of a positive ion, the ion is attracted to the negative-polarity rod and begins to move towards it. However, as it approaches the rod, the phase of the rod shifts to a positive polarity, repelling the positive ion and pushing it back towards the center of the quadrupole. At the same time, the decreasing pressure and a DC voltage gradient give the ions additional kinetic energy and guide them in the axial direction (deeper into the mass spectrometer). Ultimately, the ions adopt a circular oscillatory movement that resembles a corkscrew. A schematic of typical DV voltages applied within the mass spectrometer are illustrated below.

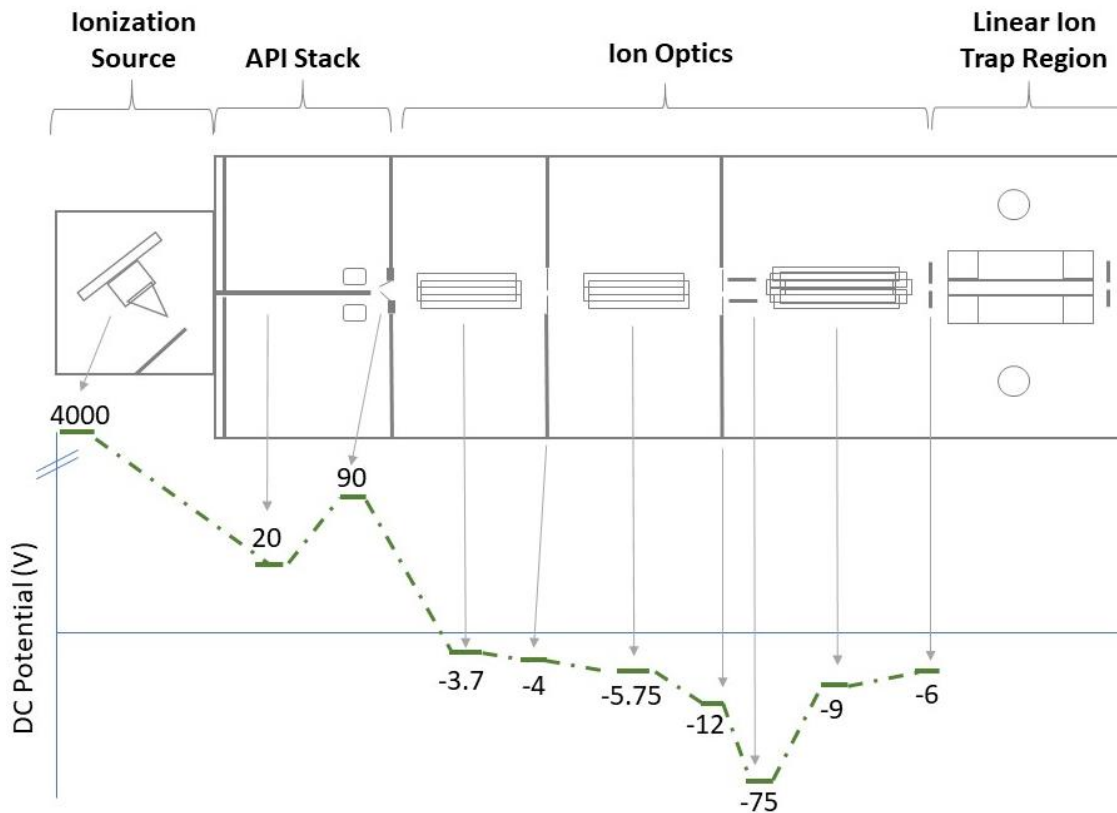


Figure 2.4 Standard DC potentials of various components within the Thermo Scientific Linear Quadrupole Ion Trap mass spectrometer. The decreasing voltage gradient aids in accelerating ions in the axial direction (deeper into the mass spectrometer) and guiding the ions through the ion optics region. DC voltages are also applied in the linear ion trap region but are not shown in the figure (see Section 2.3.3).

### 2.3.3 Linear Quadrupole Ion Trap

After traveling through the ion optics region of the mass spectrometer, the ions enter the linear ion trap through the front lens. The linear ion trap is a specially designed quadrupole composed of four hyperbolic rods, each divided into three sections. The front and back sections of each rod are 12 mm long and are responsible for trapping the ions in the axial direction while the middle section of each rod is 37 mm long and is responsible for trapping in the radial direction. Specially cut slits in the middle sections of two rods allow the ions to be ejected from the trap for detection. Within the LQIT mass spectrometer, the linear ion trap is used for four main purposes: ion trapping, ion isolation, ion activation, and ion ejection for detection. Each of these four functions are explained in further detail in the following sections.

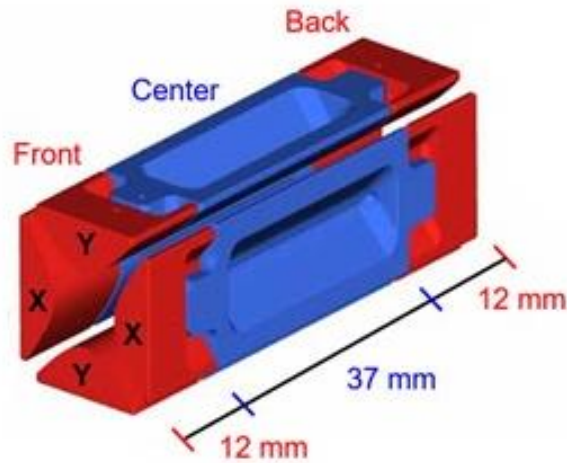


Figure 2.5 A schematic of the ion trap. The ion trap consists of four hyperbolic rods, each divided in three different sections: front, center, and back. The front and back sections are both 12 mm long while the center section is 37 mm. The x rods (labeled x) contain exit slits in the center section for ion ejection. Figure was altered from reference 37 with permission.

## 2.4 Functions of the Linear Quadrupole Ion Trap

### 2.4.1 Ion Trapping

Ion trapping within the linear ion trap is accomplished using a combination of DC and RF potentials and helium gas. Each of the three trapping components serves a different role, and in combination trap the ions both axially and radially.

#### *Axial Ion Trapping (z-direction)*

Trapping ions in the axial direction prevents them from exiting the linear ion trap through the two ends of the quadrupole. To accomplish this, the front and back sections on each rod are held at a higher DC potential than the middle section. For example, positive ions are commonly trapped using DC potentials of -9, -12, and -7 applied to the front, middle, and back sections, respectively. The lower potential applied to the middle section of each rod creates a potential energy well in the center of the trap, which restricts the ion movement to the center of the trap.

The helium buffer gas inside the ion trap helps to keep the ions in a cohesive packet within the center of the trap.<sup>38</sup> When an ion collides with a helium atom, the ion imparts some of its energy to the helium in a process called momentum transfer. The collisions are not energetic enough to cause ion fragmentation. Since the ions will collide many times with the helium gas, they lose

considerable kinetic energy and are further focused within the center of the ion trap in a process referred to as collisional cooling. This focusing serves several roles. First, keeping the ions at relatively low kinetic energy in the center of the trap increases the ion lifetime within the ion trap by reducing the number of ions which collide with the ion trap itself and are therefore neutralized and cannot be detected. This ultimately increases the sensitivity of the instrument by preserving the largest number of ions. Second, focusing of the ions in the center of the trap aids in cohesive ion ejection (see section 2.4.4). Ion ejection is achieved by increasing the RF voltage in the ion trap to systematically destabilize and eject ions. The applied voltage required to eject a given ion is calculated based on the assumption that the ion is located in the center of the trap. Ions located elsewhere will be ejected at a slightly different RF frequency and can lead to instrumental noise and low instrument resolution. Therefore, collisional cooling also helps to increase the resolution of the instrument.<sup>35,38</sup>

### ***Radial Ion Trapping (x- and y-directions)***

Trapping ions in the radial direction requires both RF and DC potentials be applied to the rods of the linear ion trap to create a quadrupolar potential ( $\Phi$ ).<sup>39,40</sup> This quadrupolar potential is related to the applied electric potential ( $\Phi_0$ ), the radius of the quadrupole rods ( $r_0$ ), and three weighted ( $\lambda$ ,  $\sigma$ , and  $\gamma$ ) coordinates ( $x$ ,  $y$ , and  $z$ ). The equation for the quadrupolar field is given below.<sup>39</sup>

$$\Phi = \frac{\Phi_0}{r_0^2} (\lambda x^2 + \sigma y^2 + \gamma z^2) \quad (2.1)$$

For an ion trap,  $\lambda$  and  $\sigma$  are both equal to one while  $\gamma$  is -2. Therefore, the quadrupolar potential for a linear ion trap can be rewritten as:<sup>39</sup>

$$\Phi = \frac{\Phi_0}{r_0^2} (x^2 + y^2 - 2z^2) \quad (2.2)$$

Next, a substitution will be made for the applied electric potential ( $\Phi_0$ ), which is related both the DC potential ( $U$ ) and the RF voltage applied to the rods ( $V\cos\omega t$ ). The RF voltage oscillates as a function of time ( $t$ ) and is related to the amplitude of the voltage applied ( $V$ ) and the angular frequency ( $\Omega$ ). Ultimately, the applied electric potential ( $\Phi_0$ ) is expressed as follows:<sup>39</sup>

$$\pm \Phi_0 = \pm(U - V\cos\Omega t) \quad (2.3)$$

After substituting equation 2.3 into equation 2.1 and differentiating with respect to  $x$ , the

quadrupolar field in the x direction can be rewritten as:<sup>39</sup>

$$\frac{\delta\phi}{\delta x} = \frac{2x}{r_0^2} (U + V\cos\Omega t) \quad (2.4)$$

The partial derivative with respect to y will follow the same pattern as equation 2.4.

An ion with a mass m and charge z will experience a certain force within this quadrupolar field. This force is defined as:

$$F_x = m \frac{d^2x}{dt^2} = -ze \frac{d\phi}{dx} \quad (2.5)$$

$$F_y = m \frac{d^2y}{dt^2} = -ze \frac{d\phi}{dy} \quad (2.6)$$

where e is the elementary charge ( $1.602 \times 10^{-19}$  C).

After substituting the partial derivative from equation 2.4 into equation 2.5 (and the equivalent partial derivative for y into equation 2.6), the force on an ion in a quadrupolar field can be expressed as:<sup>41</sup>

$$\frac{d^2x}{dt^2} + \frac{2ze}{mr_0^2} (U - V\cos\Omega t)x = 0 \quad (2.7)$$

$$\frac{d^2y}{dt^2} + \frac{2ze}{mr_0^2} (U - V\cos\Omega t)y = 0 \quad (2.8)$$

A solution for differential equations of this form can be found by referring to the Mathieu equation (2.9), which was originally introduced by the mathematician Mathieu to describe the vibration of elliptical drumheads.<sup>41</sup>

$$\frac{d^2u}{d\xi^2} + (a_u - 2q_u \cos 2\xi)u = 0 \quad (2.9)$$

By defining the parameter  $\xi$  as  $\Omega t/2$  and substituting into equation 2.7 and 2.8, these two equations can be rewritten in the form of the Mathieu equation, where  $q_u$  and  $a_u$  are stability parameters.<sup>41</sup>

$$a_u = a_x = (-)a_y = \frac{8zeU}{mr_0^2\Omega^2} \quad (2.10)$$

$$q_u = q_x = (-)q_y = \frac{4zeV}{mr_0^2\Omega^2} \quad (2.11)$$

The stability parameters describe the motions of ions of a given m/z inside the ion trap's quadrupolar field and are inversely proportional to the m/z of the ion. In other words, for a given DC and RF voltage, ions with a smaller m/z will have higher  $a_u$  and  $q_u$  values. To determine

whether an ion has a stable trajectory within the ion trap, a Mathieu stability diagram must be examined. A sample Mathieu stability diagram is given in the figure below. This diagram is a graphical representation of which  $a_u$  and  $q_u$  values correspond to stable motion. The areas of overlap indicate regions where the ion has stable x and y trajectories and can therefore be successfully trapped within the ion trap. While several areas exist, ion traps are most easily and efficiently operated at a DC potential of zero, so only the area of stability along the x-axis is used for the linear ion trap.

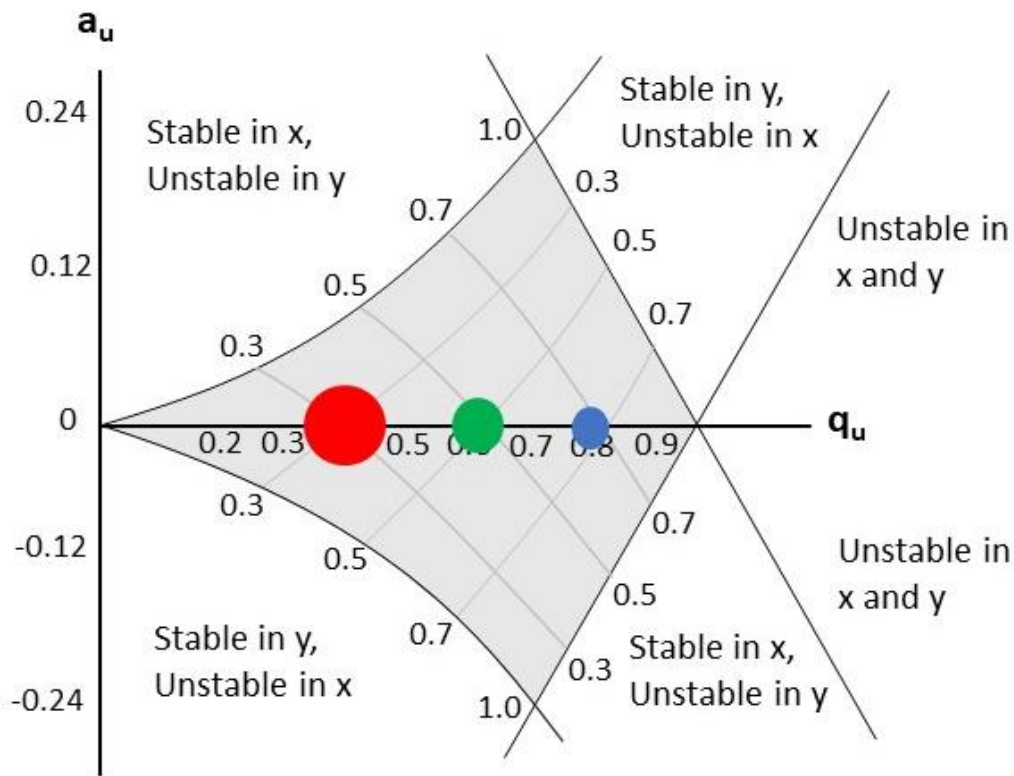


Figure 2.6 Simplified Mathieu stability diagram for a linear quadrupole ion trap. The diagram shows the overlapping region of simultaneous x- and y-direction ion trajectory stability (shown in grey). The x-axis corresponds to the  $q_u$  stability parameter while the y-axis corresponds to the  $a_u$  stability parameter. The three colored circles represent three ions of different masses with an assumed charge of one. The heaviest ion (red) has the lowest  $q_u$  value while the lightest ion (blue) has the highest  $q_u$  value at the given operating parameters. It is important to note that the Mathieu stability diagram in no way represents the ions physical location within the trap: ions of different  $m/z$  are not segregated within the trap as they are in the stability diagram. The relative location of ions within the stability diagram can be manipulated by changing the DC voltage applied to the rods ( $a_u$  value) or the RF voltage applied to the rods ( $q_u$  value).

## 2.4.2 Ion Isolation

After trapping ions within the linear ion trap, it is often necessary to isolate ions of a specific  $m/z$  while ejecting all other ions. This is a necessary first step when performing tandem mass spectrometry or ion molecule reactions. Isolating ions relies on the fact that ions oscillate at a frequency that is dependent on their  $m/z$  value. Tailored RF waveforms can therefore remove unwanted ions while leaving the desired  $m/z$  ions within the trap. This process requires two steps. In the first step, the RF voltage on the rods is ramped until the ion of interest reaches a  $q_u$  stability parameter value of 0.803. By ramping the RF voltage to this point, nearly all ions that have a  $m/z$  lower than the ion being isolated are destabilized and ejected from the instrument. The second step is to remove the remaining unwanted ions, most of which will have larger  $m/z$  values. This is accomplished by applying an AC voltage in the form of a broad-band excitation waveform, also called dipolar excitation. This waveform consists of frequencies from approximately 5-500 kHz but does *not* include the frequency which corresponds to the  $q_u$  of 0.803, where the ion of interest resides. The broad-band excitation waveform excites all of the ions except the ion being isolated, ejecting the unwanted ions from the trap and effectively isolating the ions with the chosen  $m/z$ .

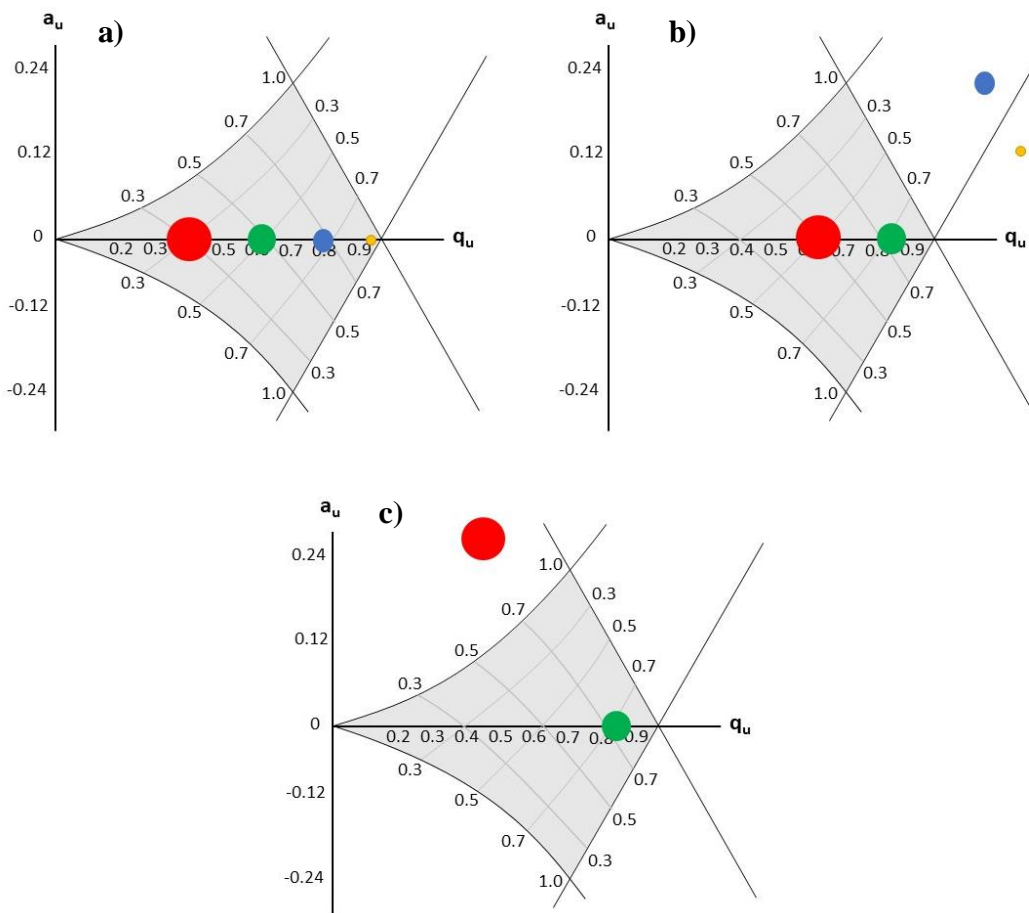


Figure 2.7 Mathieu stability diagrams illustrating the process of isolating ions of a single  $m/z$  within the linear ion trap. In this simplified example, four ions of differing  $m/z$  are first introduced into the trap. Their corresponding  $q_u$  values are shown in (a) and are a function of their  $m/z$ . In (b), the RF voltage on the rods is increased until the ion being isolated (green circle) has a  $q_u$  value of 0.803. At this point, the ions with smaller  $m/z$  values (blue and yellow circles) have such high  $q_u$  values that their trajectories are unstable and they are ejected from the trap. To remove the larger  $m/z$  ion (red circle), a broadband excitation waveform without the RF corresponding to  $q_u$  of 0.803 is applied (not shown), which destabilizes all remaining ions within the trap (c).

### 2.4.3 Ion Excitation and Activation

After isolating ions in the ion trap (section 2.4.2), one option is to excite and activate the ions to induce fragmentation. In the linear quadrupole ion trap, this process occurs through collision activated dissociation (CAD) which is sometimes called collision induced dissociation (CID); both

terms are synonymous. In this process, the ions isolated in the trap undergo numerous collisions with helium gas in the ion trap. As the collisions occur, the ions gain enough energy to induce fragmentation. A CAD experiment in a linear ion trap occurs in two steps. First, the  $q_u$  value of the trapped ions must be decreased. During ion isolation, the ions being isolated are brought to a  $q_u$  value of 0.803. For a CAD experiment, this value is decreased to approximately 0.25 by decreasing the amplitude of the RF voltage. The  $q$  value is decreased because the resulting fragments will have lower  $m/z$  values than the parent ion. If the  $q_u$  value remained at 0.803 for the fragmenting ion, the fragments would likely have  $q_u$  values high enough that their trajectories would be unstable and they would be spontaneously ejected from the ion trap without trapping or detection. The starting  $q_u$  value can be altered in the instrument software depending on the desired outcome. Higher  $q_u$  values require fewer collisions to fragment but introduce a higher mass cutoff (the lowest  $m/z$  value that can be trapped and detected during the experiment). Lower  $q_u$  values require a higher number of collisions to fragment but have a lower mass cutoff.

Regardless of the chosen  $q_u$  value, the next step is to kinetically excite the ions. This occurs by introducing a supplementary RF voltage, formally called a dipolar resonance excitation and informally called a “tickle voltage.” The supplementary RF voltage increases the kinetic energy of the ion and results in increased amplitude of motion in the  $x$ - $y$  plane. As the ion’s movement increases, collisions with the helium buffer gas occur more frequently and at higher energies. With each collision, some of the ion’s kinetic energy is transformed into internal energy, which is then distributed throughout the ion. After many collisions, the ion has a high enough internal energy that its weakest bond(s) break and the ion fragments. This process is highly repeatable so long as the experimental conditions are not changed. Therefore, the fragmentation patterns can be used for compound identification or for proposing likely structures for unknown compounds.

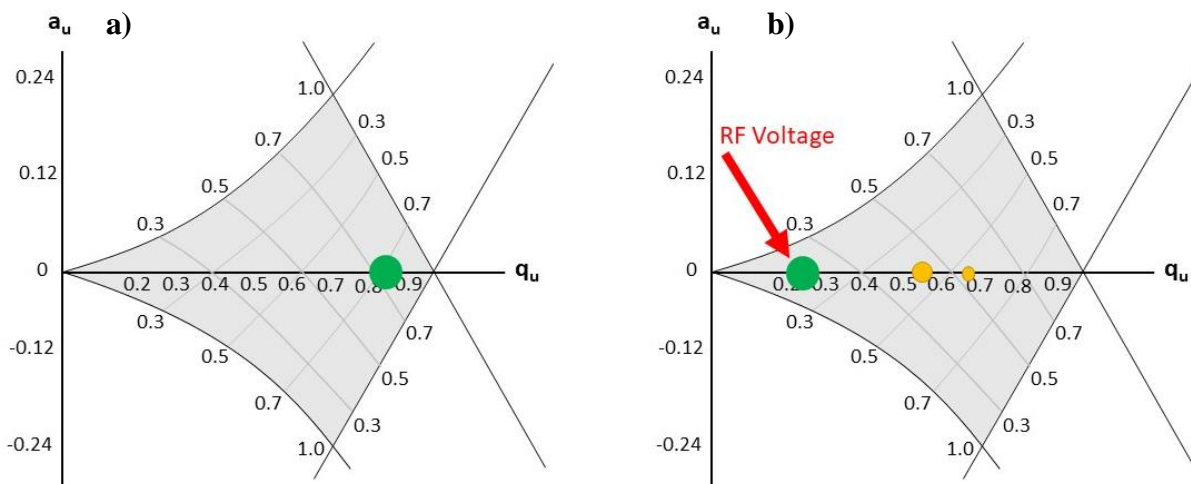


Figure 2.8 Simplified schematic of collision activated dissociation as shown on a Mathieu stability diagram. First, the ion of interest or “parent ion” (green circle), is isolated within the trap at a  $q_u$  value of 0.803 (a). Next (b), the ion’s  $q_u$  value is decreased to 0.25. A supplementary RF voltage, colloquially called a “tickle voltage” is applied to excite the ion until it fragments, producing one or more smaller  $m/z$  fragment ions (yellow circles). Because the parent ion (green circle) was fragmented at a low  $q_u$  value, the smaller  $m/z$  fragments are sufficiently trapped by the linear ion trap. If fragmentation took place in (a), neither fragment ions would have stable trajectories within the trap and would not be detected.

#### 2.4.4 Ion Ejection

To successfully detect ions, the ions must be ejected from the ion trap in a controlled and systematic manner. This systematic ejection can be accomplished in the LQIT in two different ways. The first type of ejection is an axial instability scan. In this scan type, the RF voltage is increased to systematically bring the  $q_u$  value of the ions to 0.908, which is the value at which the ions become unstable in the  $x$  direction. Once the ions are unstable in the  $x$ -direction, they are ejected from the trap along the  $x$  axis. The middle section of the  $x$ -direction quadrupole rods have exit slits cut into them, which allow the ions to exit the trap. As the RF voltage is systematically increased, ions of higher and higher  $m/z$  are ejected and detected. The  $m/z$  of each ion detected is therefore calculated by the instrument software based on the RF voltage at which it was ejected from the trap. However, this method can have low sensitivity, because some ions are lost during this process.<sup>42</sup>

The second type of ion ejection is  $x$ -electrode dipolar resonance ejection. In this ejection mode, a supplemental RF voltage of fixed frequency is applied just to the  $x$ -rods (the  $x$ -direction

quadrupole rods containing the exit slits). Then, the main RF voltage is systematically increased, exactly as in an axial instability scan. However, the major difference is the voltage and corresponding  $q_u$  value at which the ions become unstable. In an axial instability scan, instability is reached at a  $q_u$  of 0.908, but dipolar resonance ejection lowers this value to 0.88. At 0.88, the ions are in resonance with the supplemental RF voltage on the x-rods. The resonance increases the ions kinetic energy and therefore increases the radius of their oscillations. At a certain point, the ions oscillation takes them in a cohesive packet through the exit slits of the x-rods and out of the ion trap so they can be detected. This use of dipolar resonance ejection increases both the sensitivity of the mass spectrometer and the resolution.

## **2.5 Ion Detection**

After ions are ejected from the ion trap, they must be detected. The linear quadrupole ion trap mass spectrometer has two detectors, which are located near the exit slits of the x-rods, through which the ions are ejected. Each individual detector is composed of a conversion dynode and an electron multiplier. When an ion is ejected, it is electrically attracted towards the cup-shaped conversion dynode. For positive ions, the conversion dynode has a -15 kV potential applied to it, while the conversion dynode has a +15 kV potential applied when detecting negative ions. When an ion collides with the conversion dynode, secondary ions are produced. For positive ions, the secondary ions are negative ions and electrons. For negative ions, the secondary ions produced are positive ions. The cup shape of the conversion dynode focuses the secondary ions into a cohesive packet. The charge on the conversion dynode, which is always the same as the charge of the produced secondary ions, accelerates the secondary ions away from the dynode and towards the electron multiplier.

The role of the electron multiplier is to turn the secondary ions produced at the conversion dynode into a cascade of electrons which produce a signal proportionate to the number of ions which exited the linear ion trap. Secondary ions first strike the cone-shaped lead oxide cathode, which releases electrons upon impact. The released electrons then travel further down the cone, striking the walls and producing more electrons. This process is repeated numerous times, creating a cascade of electrons which is proportionate to the original number of secondary electrons which struck the cathode. Eventually, the electrons make it down the cathode and strike the anode, which records and transmits the current produced by the electrons. The relative current produced by each

$m/z$  (see section 2.4.1 for how the  $m/z$  is determined) is translated into the relative abundance of the ion at each  $m/z$ .

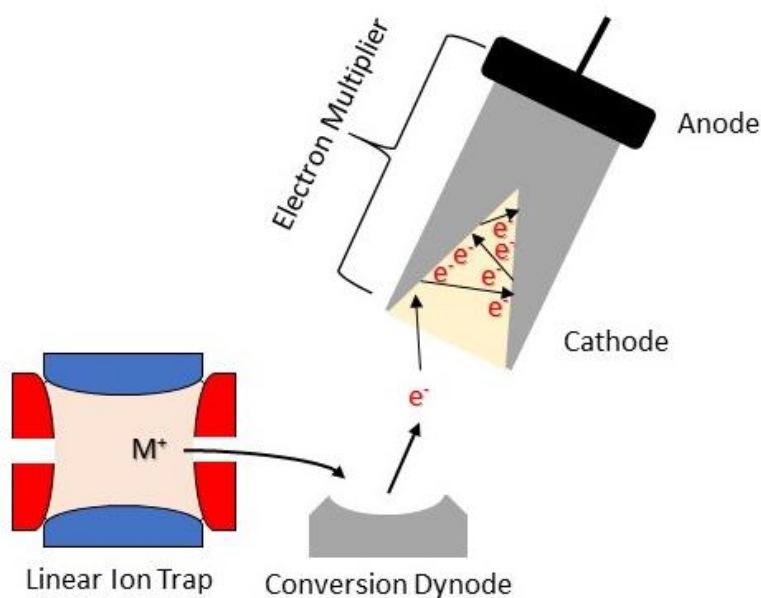


Figure 2.9 Location and simplified schematic of one detector in the Thermo Scientific Linear Quadrupole Ion Trap mass spectrometer. The detector is located in the same general plane as the exit slits on the x rods (shown in red). Ions (shown as  $M^+$ ) are ejected from the exit slits and are attracted to the conversion dynode. After striking the dynode, secondary particles are ejected (shown here as  $e^-$ ). The secondary particles are attracted to the cathode of the electron multiplier where the initial collision results in an electron cascade. The anode of the electron multiplier measures the resulting current.

## 2.6 Orbitrap

The linear quadrupole ion trap operates at unit resolution, meaning that has enough resolution to distinguish ions with mass to charge ratios that differ by a whole unit. However, the resolution of the ion detection can limit the utility of the instrument, particularly when the same contains isobaric ions. Isobars are ions that have the same nominal  $m/z$  but different elemental makeup, meaning their  $m/z$  values may differ by tenths or hundredths of a  $m/z$  unit. In this case, alternative mass analyzers or mass spectrometers with higher resolution are required. The orbitrap, an electrostatic mass analyzer, is capable of separating isobars and then using the unique image current generated by each isobar for detection. In the hybrid LQIT/Orbitrap instrument, an additional orbitrap mass analyzer is integrated into the instrument and can be used when higher resolution is required. A schematic for the LQIT/Orbitrap instrument is located below.

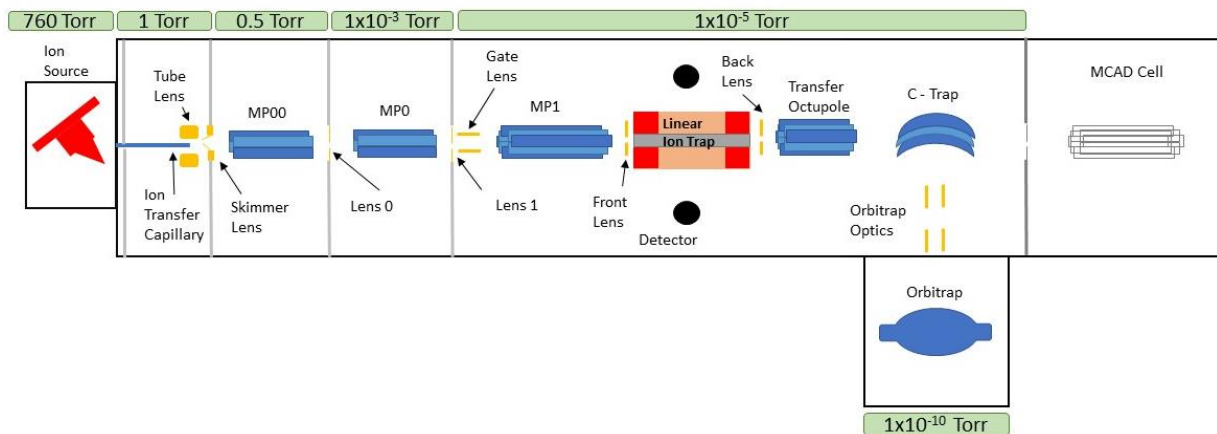


Figure 2.10 Simplified schematic of the Thermo Scientific LQIT/Orbitrap hybrid instrument. The instrument from the ion source through to the linear ion trap is identical to the Thermo Scientific Linear Quadrupole Ion Trap discussed previously. The addition of the transfer octupole, C-trap, Orbitrap, and MCAD cell are unique to the hybrid instrument. The MCAD cell is shown in grey because it was not used for this dissertation and will not be discussed.

The orbitrap uses electrostatic fields to induce very specific ion motion within the orbitrap.<sup>43</sup> The frequency at which ions oscillate within the orbitrap varies based on the  $m/z$  value. The orbitrap therefore measures an image current of the ion oscillation and converts the oscillation frequencies into the  $m/z$  values and relative abundance of each of the oscillating ions. The injection into the orbitrap is highly specialized, and the ion motion and detection within the orbitrap are distinct: all three topics are discussed in the following sections.

## 2.6.1 Ion Injection

In a hybrid LQIT/orbitrap such as the one used for this thesis, ion generation and transfer into the ion trap is identical to the LQIT previously discussed. However, when using the orbitrap as the detector, the ions' journey does not end with the linear ion trap. Instead, after exiting the ion trap, the ions are transferred through an octupole and into a C-trap, which is an RF only quadrupole bent into the shape of a shallow C. The C-trap is maintained at a higher pressure of approximately 1 mTorr. The nitrogen gas used to fill the C-trap cools the ions through numerous collisions. A high DC voltage focuses the cooled ions into a tight packet, which is then injected off-center into the orbitrap. The ions are injected into the orbitrap off-center to induce axial motion around the center spindle of the orbitrap.

## 2.6.2 Motion in the Orbitrap

The orbitrap mass analyzer is made of two separate electrodes. The outer electrode has a football shape while the inner electrode has a spindle shape. An electrostatic field exists between the two electrodes because of an applied DC current. The electrostatic field depends on the angular and axial coordinates ( $r$  and  $z$ , respectively), the field curvature constant  $k$ , a constant  $C$ , and the radius of the ion's characteristic motion ( $R_m$ ). The relationship is defined below.<sup>44, 45</sup>

$$U(r, z) = \frac{k}{2}(z^2 - r^2) + \frac{k}{2}(R_m)^2 \ln \left[ \frac{r}{R_m} \right] + C \quad (2.12)$$

The electrostatic field induces a characteristic three-dimensional motion for each ion injected into the orbitrap. Ions with the exact same mass-to-charge ratio have the same characteristic motion and frequency, but ions of different mass-to-charge ratio will have different frequencies. The three-dimensional motion involves radial motion ( $\omega_r$ ), axial oscillations ( $\omega_z$ ), and rotation around the spindle electrode ( $\omega_\phi$ ). For a given mass and charge ( $m$  and  $q$ ), the motions are described by the following three equations (radial, axial, and rotation, respectively):<sup>43</sup>

$$\frac{d}{dt} \left( r^2 \frac{\partial \phi}{\partial t} \right) = 0 \quad (2.13)$$

$$\frac{\partial^2 z}{\partial t^2} = -kz \frac{q}{m} \quad (2.14)$$

$$\frac{\partial^2 r}{\partial t^2} - \left( \frac{\partial \phi}{\partial t} \right)^2 = -\frac{q}{m} \frac{k}{2} \left[ \frac{R_m^2}{r} - r \right] \quad (2.15)$$

Only equation 2.14 (axial motion) is independent of the position,  $r$ , and energy,  $\phi$ , of the ion. Therefore, only the axial motion is recorded and transformed into a signal for ion mass-to-charge and abundance. The axial motion can be simplified if viewed as a simple harmonic oscillator with an initial amplitude ( $z_0$ ), axial kinetic energy ( $E_z$ ), and axial oscillation frequency ( $\omega$ ), which is further dependent on the ion charge ( $q$ ), ion mass ( $m$ ), and a constant  $k$ .<sup>43</sup>

$$z(t) = z_0 \cos(\omega t) + \left( \frac{2E_z}{k} \right)^{1/2} \sin(\omega t) \quad (2.16)$$

$$\omega = \sqrt{\left( \frac{q}{m} \right) k} \quad (2.17)$$

As can be seen, the oscillation in the  $z$  direction (axial) is inversely related to the mass-to-charge ratio of the ion and independent of the position within the orbitrap.

### 2.6.3 Ion detection in the Orbitrap

Since all ions of the same  $m/z$  have the same oscillation frequency (see equation 2.17), they form thin rings around the inner electrode and produce an induced current. The outer electrode can measure the current produced by the rotating ions as an image current signal.<sup>46</sup> The recorded signal is then amplified by a signal amplifier. Next, the time-domain signal is transformed into a frequency domain using a fast Fourier transform (FFT). Finally, using an internal calibration, the frequency domain signal is transformed into a mass spectrum.<sup>46</sup>

## 2.7 References

1. Maurer, H.H. Mass Spectrometry for Research and Application in Therapeutic Drug Monitoring or Clinical and Forensic Toxicology. *Ther. Drug Monit.* **2018**, *40*, 389 – 393.
2. Kong, J.Y.; Yu, Z.; Easton, M.W.; Niyonsaba, E.; Ma, X.; Yerabolu, R.; Sheng, H.; Harrell, T.M.; Zhang, Z.; Ghosh, A.K.; Kenttämaa, H.I. Differentiating Isomeric Deprotonated Glucuronide Drug Metabolites via Ion/Molecule Reactions in Tandem Mass Spectrometry. *Anal. Chem.* **2018**, *90*, 9426-9433.
3. Conte, S.; Arletti, R.; Mermati, F.; Gratuze, B. Unravelling the Iron Age Glass Trade in Southern Italy: The First Trace-Element Analyses. *Eur. J. Mineral.* **2016**, *28*, 409-433.
4. Bjarnason, A.; Taylor, J. W.; Kinsinger, J. A.; Cody, R. B.; Weil, D. A. Isomer Discrimination of Disubstituted Benzene Derivatives through Gas-Phase Iron (I) Ion Reactions in a Fourier-Transform Mass Spectrometer. *Anal. Chem.* **1989**, *61*, 1889–1894.
5. Kong, J. Y.; Yu, Z.; Easton, M. W.; Niyonsaba, E.; Ma, X.; Yerabolu, R.; Sheng, H.; Jarrell, T. M.; Zhang, Z.; Ghosh, A. K. Differentiating Isomeric Deprotonated Glucuronide Drug Metabolites via Ion/Molecule Reactions in Tandem Mass Spectrometry. *Anal. Chem.* **2018**, *90*, 9426–9433.
6. Vogel, J.S.; Turteltaub, K.W.; Finkel, R.; Nelson, D.E. Accelerator Mass Spectrometry. *Anal. Chem.* **1995**, *67*, 353-359.
7. Guilhaus, M. Principles and Instrumentation in Time-of-Flight Mass Spectrometry: Physical and Instrumental Concepts. *J. Mass Spectrom.* **1995**, *30*, 1519-1532.
8. Nier, A. O. A Mass Spectrometer for Isotope and Gas Analysis. *Rev. Sci. Instrum.* **1947**, *18*, 398–411.
9. Munson, M. S.; Field, F.-H. Chemical Ionization Mass Spectrometry. I. General Introduction. *J. Am. Chem. Soc.* **1966**, *88*, 2621–2630.
10. Vestal, M. L. Methods of Ion Generation. *Chem. Rev.* **2001**, *101* (2), 361–375.

11. Karas, M.; Hillenkamp, F. Laser Desorption Ionization of Proteins with Molecular Masses Exceeding 10,000 Daltons. *Anal. Chem.* **1988**, *60*, 2299–2301.
12. Cody, R.B.; Laramée, J.A.; Durst, H.D. Versatile New Ion Source for Analysis of Materials in Open Air Under Ambient Conditions. *Anal. Chem.* **2005**, *77*, 2297 – 2302.
13. Hirata, T.; Ohno, T. In-situ Isotopic Ratio Analysis of Iron Using Laser Ablation-Multiple Collector-Inductively Coupled Plasma Mass Spectrometry (LA-MC-ICP-MS). *J. Anal. At. Spectrom.* **2001**, *16*, 487-491.
14. Takats, Z.; Wiseman, J.M.; Gologan, B.; Cooks, R.G. Mass Spectrometry Sampling Under Ambient Conditions with Desorption Electrospray Ionization. *Science*, **2004**, 471 – 473.
15. Smith, R. D.; Loo, J. A.; Edmonds, C. G.; Barinaga, C. J.; Udseth, H. R. New Developments in Biochemical Mass Spectrometry: Electrospray Ionization. *Anal. Chem.* **1990**, *62*, 882–899.
16. Cech, N. B.; Enke, C. G. Practical Implications of Some Recent Studies in Electrospray Ionization Fundamentals. *Mass Spectrom. Rev.* **2001**, *20*, 362–387.
17. Hsu, H.J.; Oung, J.N.; Kuo, T.L.; Wu, S.H.; Shiea, J. Using Electrospray-Assisted Pyrolysis Ionization/Mass Spectrometry for the Rapid Characterization of Trace Polar Components in Crude Oil, Amber, Humic Substances, and Rubber Samples. *Rapid Commun. Mass Spectrom.* **2007**, *21*, 375-384.
18. R. B. Cole, *Electrospray and MALDI Mass Spectrometry*, John Wiley & Sons, New Jersey, NJ, USA, 2010.
19. Wilm, M.S.; Mann, M. Electrospray and Taylor-Cone Theory, Dole's Beam of Macromolecules at Last? *Int. J. Mass Spectrom. Ion Processes* **1994**, *136*, 167-180.
20. Covey, T. R.; Thomson, B. A.; Schneider, B. B. Atmospheric Pressure Ion Sources. *Mass Spectrom. Rev.* **2009**, *28*, 870–897.
21. Rayleigh, L. On the Equilibrium of Liquid Conducting Masses Charged with Electricity, *Philosophical Magazine*, **1882**, 184–186.
22. Gomez, A.; Tang, K. Charge and Fission of Droplets in Electrostatic Sprays. *Phys. Fluids*, **1994**, *6*, 404-414.
23. Duft, D.; Achtzehn, T.; Müller, R.; Huber, B.A.; Leisner, L. Coulomb Fission: Rayleigh Jets from Levitated Microdroplets. *Nature*, **2003**, *421*, 128.
24. Kebarle, P. A Brief Overview of the Present Status of the Mechanisms Involved in Electrospray Mass Spectrometry. *J. Mass Spectrom.* **2000**, *35*, 804-817.
25. Iavarone, A. T.; Williams, E. R. Mechanism of Charging and Supercharging Molecules in Electrospray Ionization. *J. Am. Chem. Soc.* **2003**, *125*, 2319–2327.

26. De La Mora, J. F. Electrospray Ionization of Large Multiply Charged Species Proceeds via Dole's Charged Residue Mechanism. *Anal. Chim. Acta* **2000**, *406*, 93–104.
27. Konermann, L.; Ahadi, E.; Rodriguez, A. D.; Vahidi, S. Unraveling the Mechanism of Electrospray Ionization. *Anal. Chem.* **2013**, *85*, 2–9.
28. Iribarne, J. V.; Thomson, B. A. On the Evaporation of Small Ions from Charged Droplets. *J. Chem. Phys.* **1976**, *64*, 2287–2294.
29. Konermann, L.; Rodriguez, A. D.; Liu, J. On the Formation of Highly Charged Gaseous Ions from Unfolded Proteins by Electrospray Ionization. *Anal. Chem.* **2012**, *84*, 6798–6804.
30. Proctor, C.J.; Todd, J.F.J. Atmospheric Pressure Ionization Mass Spectrometry. *Org. Mass Spectrom.* **1983**, *18*, 509-516.
31. Sunner, J.; Nicol, G.; Kebarle, P. Factors Determining Relative Sensitivity of Analytes in Positive Mode Atmospheric Pressure Ionization Mass Spectrometry. *Anal. Chem.* **1988**, *60*, 1300–1307.
32. De Hoffmann, E.; Stroobant, V. *Mass Spectrometry: Principles and Applications*, 3rd ed.; West Sussex, 1997.
33. Thomson, B.A. Atmospheric Pressure Ionization and Liquid Chromatography/Mass Spectrometry—Together at Last. *J. Am. Soc. Mass Spectrom.* **1998**, *9*, 187-193.
34. Carroll, D. I.; Dzidic, I.; Stillwell, R. N.; Haegele, K. D.; Horning, E. C. Atmospheric Pressure Ionization Mass Spectrometry. Corona Discharge Ion Source for Use in a Liquid Chromatograph-Mass Spectrometer-Computer Analytical System. *Anal. Chem.* **1975**, *47*, 2369–2373.
35. Orient, O.J.; Chutjian, A. A Compact, High-Resolution Paul Ion Trap Mass Spectrometer with Electron-Impact Ionization. *Rev. Sci. Instrum.* **2002**, *73*, 2157.
36. Schwartz, J. C.; Senko, M. W.; Syka, J. E. A Two-Dimensional Quadrupole Ion Trap Mass Spectrometer. *J. Am. Soc. Mass Spectrom.* **2002**, *13*, 659–669.
37. Romanczyk, M. Developing Mass Spectrometric Methods for Distinguishing Isomers, Characterizing Complex Mixtures and Determining the Capability of Organic Compounds to Swell Aircraft O-Ring Seals. Ph.D. Dissertation, Purdue University, West Lafayette, IN, 2019.
38. Xu, W.; Song, Q.; Smith, S.A.; Chappell, W.J.; Ouyang, Z. Ion Trap Mass Analysis at High Pressure: A Theoretical View. *J. Am. Soc. Mass Spectrom.* **2009**, *20*, 2144 – 2153.
39. March, R. E. An Introduction to Quadrupole Ion Trap Mass Spectrometry. *J. Mass Spectrom.* **1997**, *32*, 351–369.
40. March, R. E.; Todd, J. F. J. *Quadrupole Ion Trap Mass Spectrometry*, 2nd ed.; WileyInterscience: Hoboken, N.J., 2005.

41. Douglas, D. J.; Frank, A. J.; Mao, D. Linear Ion Traps in Mass Spectrometry. *Mass Spectrom. Rev.* **2005**, *24*, 1–29
42. Schwartz, J. C.; Syka, J. E. P.; Jardine, I. J. High Resolution on a Quadrupole Ion Trap Mass Spectrometer. *Am. Soc. Mass Spectrom.* **1991**, *2*, 198–204.
43. Makarov, A. Electrostatic Axially Harmonic Orbital Trapping: A High Performance Technique of Mass Analysis. *Anal. Chem.* **2000**, *72*, 1156 – 1162.
44. Makarov A. A U.S. Patent 5,886,346, 1999.
45. Gillig KJ.; Bluhm BK.; Russell DH. Ion Motion in a Fourier Transform Ion Cyclotron Resonance Wire Ion Guide Cell. *Int. J. Mass Spectrom.* **1996**, *157/158*, 129–147.
46. Makarov, A.; Denisov, E.; Kholomeev, A.; Balschun, W.; Lange, O.; Strupat, K.; Horning, S. Performance Evaluation of a Hybrid Linear Ion Trap/Orbitrap Mass Spectrometer. *Anal. Chem.* **2006**, *78*, 2113 – 2120.

## CHAPTER 3. FACTORS AFFECTING THE LIMIT OF DETECTION OF ION-MOLECULE REACTIONS IN MASS SPECTROMETRY

### 3.1 Introduction

Traditionally, NMR and X-ray crystallography have been used to identify unknown drug metabolites in the pharmaceutical industry. Recently, diagnostic ion-molecule reactions coupled with high performance liquid chromatography mass spectrometry (HPLC/MS) have emerged as a faster, cheaper alternative to these traditional identification techniques.<sup>1,2,3</sup> Ion-molecule reactions have proven capable of identifying and differentiating functional groups found in small organic molecules and in drug metabolites.<sup>4,5,6</sup> Since these ion-molecule reactions are still in the developmental stages and not approved for regulatory use, the concentrations used in these studies have been intentionally high, commonly ranging from 1.0  $\mu\text{M}$  to 1.0  $\text{mM}$ .<sup>2-4, 6-12</sup>

While high metabolite concentrations may adequately model *in vitro* metabolism study concentrations, they are not applicable to *in vivo* studies. *In vitro* concentrations tend to be quite high by design, since high concentration studies tend to produce more consistent results. The metabolites produced during these studies therefore have correspondingly high concentrations.<sup>13,14</sup> The pharmaceuticals being tested are usually incubated with human cells (traditionally human liver microsomes) at concentrations in the micromolar to millimolar range.<sup>15,16</sup> However, metabolism occurs in many organs and can vary based on a wide range of factors, from sex to interindividual genetic differences.<sup>17,18</sup> Therefore, *in vitro* studies result only in potential metabolites and cannot adequately predict all metabolites which may occur during human drug trials.<sup>15,16</sup> For this reason, *in vivo* studies are required in order to receive drug approval. When testing is performed *in vivo*, the metabolite concentrations encountered tend to be orders of magnitude lower than those seen during *in vitro* testing.<sup>19</sup> Parent drugs (the pharmaceutical being tested) are usually present in the blood stream at levels between 200 and 1000  $\text{ng/mL}$ , with only a portion of that concentration ultimately being metabolized to the metabolite of interest.<sup>1,20,21</sup> To identify metabolites during *in vivo* studies, ion-molecule reactions must be sensitive and reproducible enough at physiologically relevant concentrations.

This research presents the first study assessing the applicability of ion-molecule reactions for drug metabolite identification at physiologically relevant concentrations. Ion-molecule reactions were carried out for a series of small molecule model compounds at nanomolar and picomolar

concentrations. The detection limit for each ion-molecule reaction was determined. Based on the results, the following potential limiting factors for the detection limits of ion-molecule reactions are discussed: analyte proton affinity, ion-molecule reaction efficiency, and the number of subsequent mass spectrometer isolations required for identification. A discussion including strategies for improving the detection limits of ion-molecule reactions is presented in light of the findings.

## **3.2 Methods and Materials**

### **3.2.1 Materials**

All drug metabolites (omeprazole, omeprazole N-oxide, omeprazole sulfone, sulindac, olanzapine, albendazole sulfoxide, and quetiapine sulfoxide) were purchased from Toronto Research Chemicals (Toronto, Ontario, Canada). All other model compounds (diphenyl sulfoxide, methyl phenyl sulfone, dibenzothiophene sulfone, and butyl sulfoxide) were purchased from Sigma-Aldrich (St Louis, MO), as was the HPLC grade formic acid and the neutral reagents tris(dimethylamino)borane and trimethyl borate. All chromatographic solvents (HPLC grade water, acetonitrile, water, and isopropanol) were purchased from Fisher Scientific (Pittsburg, PA). All materials were used as received. A Phenomenex (Torrance, CA) Synergi Hydro-RP column (150 x 2 mm, 4 $\mu$ m) and an Agilent Technologies (Santa Clara, CA) Zorbax SB-C18 column (4.6 x 250 mm, 5 $\mu$ m) were used for HPLC studies.

### **3.2.2 Sample Preparation**

A stock solution of each model compound was made at 5.0 mM concentration in methanol. Quetiapine sulfoxide was made at a concentration of 8.02 mM. When calculating the concentration of each solution, the sample purity provided on each certificate of analysis was used as a correction factor. For some compounds, brief sonication at ambient temperatures was needed to fully dissolve the compound. Using the compound stock solutions, two model mixtures were prepared: model mixture 1 and model mixture 2. Model mixture 1 included 0.50 mM of each of the following compounds: omeprazole, omeprazole N-oxide, omeprazole sulfone, sulindac, olanzapine, albendazole sulfoxide, and quetiapine sulfoxide. These compounds were chosen for model mixture 1 because they have been well-studied and their reactions with the neutral reagent TDMAB have

been previously described. Additionally, each model compound has approximately the same reaction efficiency towards TDMAB (all less than 1.5 %) while covering a wide range of proton affinities. Model mixture 2 contained 0.50 mM of each of the following compounds: diphenyl sulfoxide, methyl phenyl sulfone, dibenzothiophene sulfone, and butyl sulfoxide. These compounds were chosen because sulfones and sulfoxides have dramatically different reaction efficiencies towards the neutral reagent TMB. When preparing dilutions of the equimolar model mixtures, a solvent of 50:50 (v/v) water:methanol was used. All solutions were stored refrigerated.

### 3.2.3 Instrumentation

For each experiment (except where explicitly stated otherwise), the model mixture was first separated by a Thermo Scientific Surveyor HPLC. For both model mixtures, the injection volume was set at 10  $\mu$ L in a partial loop injection. Mobile phases were 0.1 % formic acid in water (mobile phase A) and 0.1% formic acid in methanol (mobile phase B) for both model mixtures.

Model mixture 1 used a Zorbax SB-C18 column (4.6x250 mm, 5 $\mu$ m). This column was selected because it is designed to separate relatively large analyte molecules with significant differences in polarity. The nonlinear gradient was as follows: 0-2 minutes isocratic at 50% B; 15 minutes 100% B; 20 minutes 100% B; 20.1 minutes 50% B; 25 minutes 50% B. The flow rate was set at 300  $\mu$ L/min, the column temperature was maintained at 30  $^{\circ}$ C, and 400  $\mu$ L of a 50:50 (v/v) water: methanol wash solvent was used to prevent carryover.

Model mixture 2 used a Phenomenex Synergi Hydro-RP column (4.6x250 mm, 5 $\mu$ m). Since model mixture 2 consisted of much smaller analytes with very similar polarity, the hydro-RP column was chosen to maximize the separation. This column has a slightly-polar packing material that is used to maximize the separation of compounds with similar overall polarity. The nonlinear gradient was as follows: 0-2 minutes isocratic at 10% B; 10 minutes 60% B; 12 minutes 60% B; 12.1 minutes 10% B; 18 minutes 10% B. The flow rate was set at 300  $\mu$ L/min, the column temperature was 30  $^{\circ}$ C, and the wash solvent used was 50:25:25 (v/v/v) isopropyl alcohol: methanol: acetonitrile to prevent carryover.

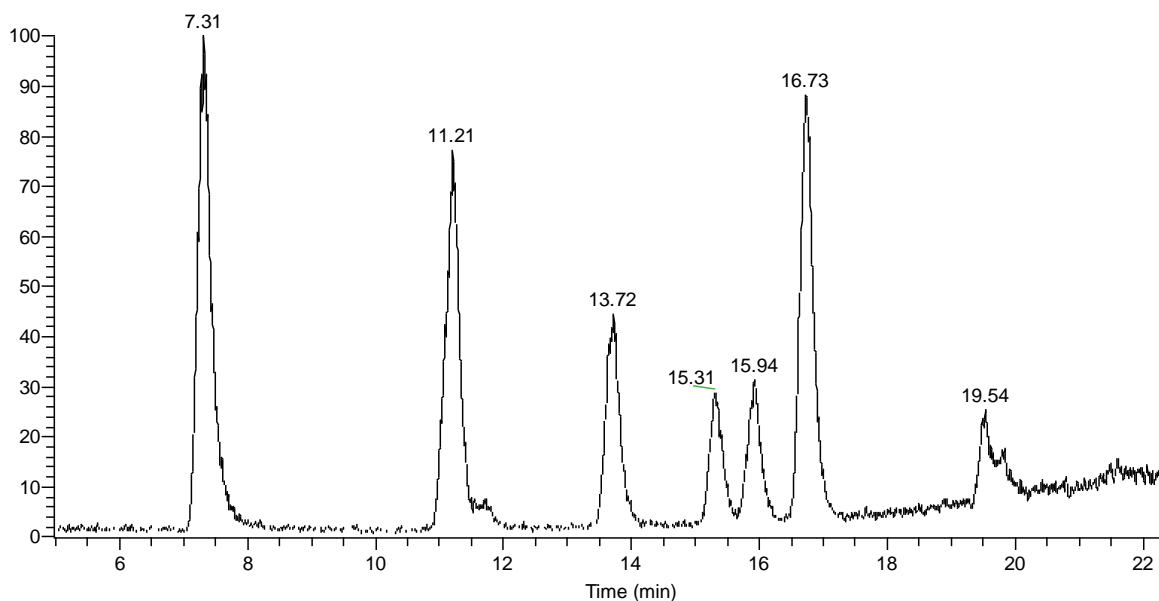


Figure 3.1 HPLC extracted ion chromatogram of model mixture one at a concentration of 500 nM. The extracted ions were the protonated forms of olanzapine (7.31 min), quetiapine sulfoxide (11.21 min), albendazole sulfoxide (13.72 min), omeprazole N-oxide (15.31 min), omeprazole (15.94 min), omeprazole sulfone (16.73 min), and sulindac (19.54 min).

All mass spectrometry measurements were performed on a Thermo Scientific LTQ linear quadrupole ion trap (LQIT) mass spectrometer. After HPLC separation, positive mode electrospray ionization (ESI) was used to generate protonated molecules. The ESI spray voltage was 5.0 kV and the ion capillary temperature was 275 °C. Nitrogen was used as the sheath and auxiliary gases at a flow rates of 50 and 10 (arbitrary units), respectively. An isolation window of 2 m/z was used to trap the ions. For model mixture 1, all protonated model compounds were reacted with TDMAB for 300 ms. For model mixture 2, reaction times between the protonated model compounds and TMB varied from 30 to 2000 ms depending on the analyte. Thermo XCalibur 2.0 software was used for all data collection and processing.

To demonstrate that the developed HPLC/MS method was valid, the mass spectrometer signal was plotted as a function of concentration. A valid method should have an approximately linear relationship between the mass spectrometer signal intensity and the concentration. An example of this plot is shown below for albendazole sulfoxide. In this case, the response is clearly linear, with an  $R^2 = 0.9988$ . The first two data points (75 and 100 nM, respectively) had nearly equal signals. This is because 100 nM was determined to be the limit of detection (see section 3.3.2).

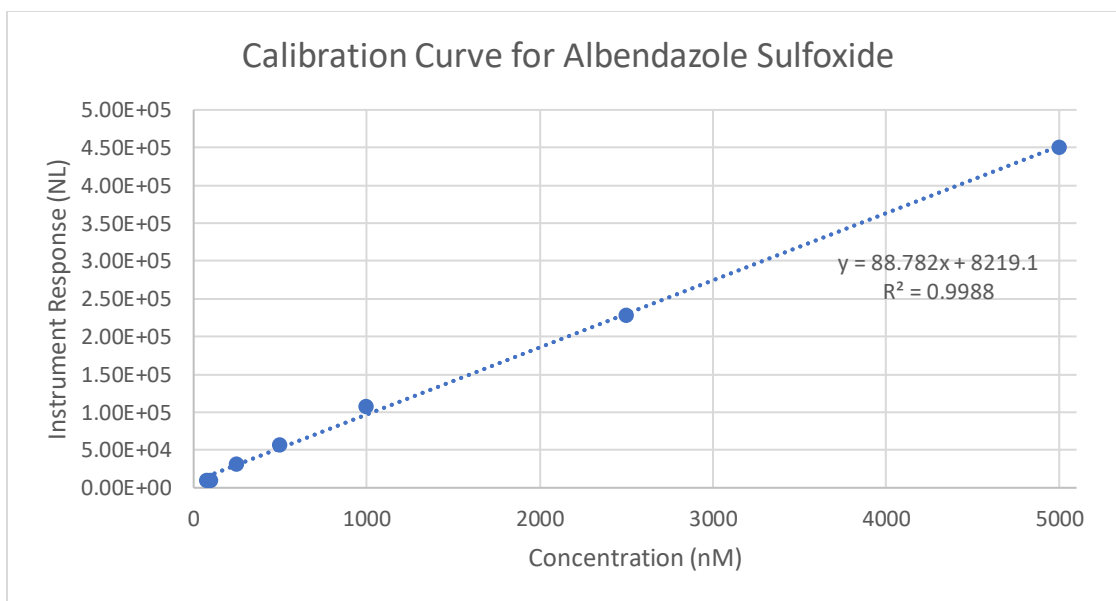


Figure 3.2 Calibration curve of albendazole sulfoxide, showing the correlation between the mass spectrometer instrument response (in normalized level “NL”) and the analyte concentration. The calibration curve is highly linear ( $R^2 = 0.9988$ ), showing good correlation and a valid instrument method.

TDMAB and TMB were introduced into the mass spectrometer ion trap through a home-built manifold which has been previously described.<sup>22</sup> The manifold flow rate for TDMAB was 4-6  $\mu\text{L/hr}$  while the flow rate for TMB was 12  $\mu\text{L/hr}$ . To fully evaporate the liquid reagents, TDMAB was heated to approximately 90  $^\circ\text{C}$  and TMB was heated to approximately 70  $^\circ\text{C}$ . Since TDMAB and TMB are not charged, the concentration of the compounds in the ion trap cannot be directly measured by the mass spectrometer. To monitor the neutral reagent in the trap, ionized methanol is introduced through the ESI probe into the mass spectrometer and isolated in the ion trap. The reaction between the neutral reagent and an infusion of 400  $\mu\text{L/min}$  of methanol is then monitored and no further experimentation takes place unless the product is stable and at a relative abundance of approximately 20 %. Since the methanol is injected at the same flow rate every time, the relative abundance is an indication of the amount of neutral reagent within the ion trap. For cleaning, the manifold was isolated from the rest of the instrument, placed under vacuum, and heated to remove any remaining reagent.

All MS<sup>3</sup> CAD experiments started with isolating a pre-chosen product ion formed from a reaction between the model compound and the neutral reagent. The product ion itself is observed

in the MS<sup>2</sup> ion-molecule reaction spectra. When fragmenting the product ion, a  $q$  value of 0.25, an activation time of 30 ms, and a normalized collision energy of 20 (arbitrary units) was used.

### 3.2.4 Calculating Reaction Efficiencies

Reaction efficiency is the fraction of collisions which result in a reaction. The reaction efficiency of each model compound ion-molecule reaction was calculated based on experimental measurements as previously described in the literature.<sup>12,23,24</sup> First, the model compound was introduced as a neat solution (5 mM) through the ESI probe and into the mass spectrometer. Since the neutral reagent concentration is much larger than the model compound ion concentration in the trap, the neutral reagent concentration is assumed constant and subsequent calculations are based on pseudo-first order reaction kinetics. Ultimately, the reaction efficiency is calculated by dividing the experimental rate constant ( $k_{\text{exp}}$ ) by the theoretical rate constant ( $k_{\text{coll}}$ ). To calculate  $k_{\text{exp}}$ , the natural log of the relative abundance of the ionized model compound is monitored and plotted as a function of time. The slope of the model compound disappearance (obtained from the graph) equals the rate constant multiplied by the neutral reagent concentration. A sample graph for determining  $k_{\text{exp}}$  is presented in the figure below.

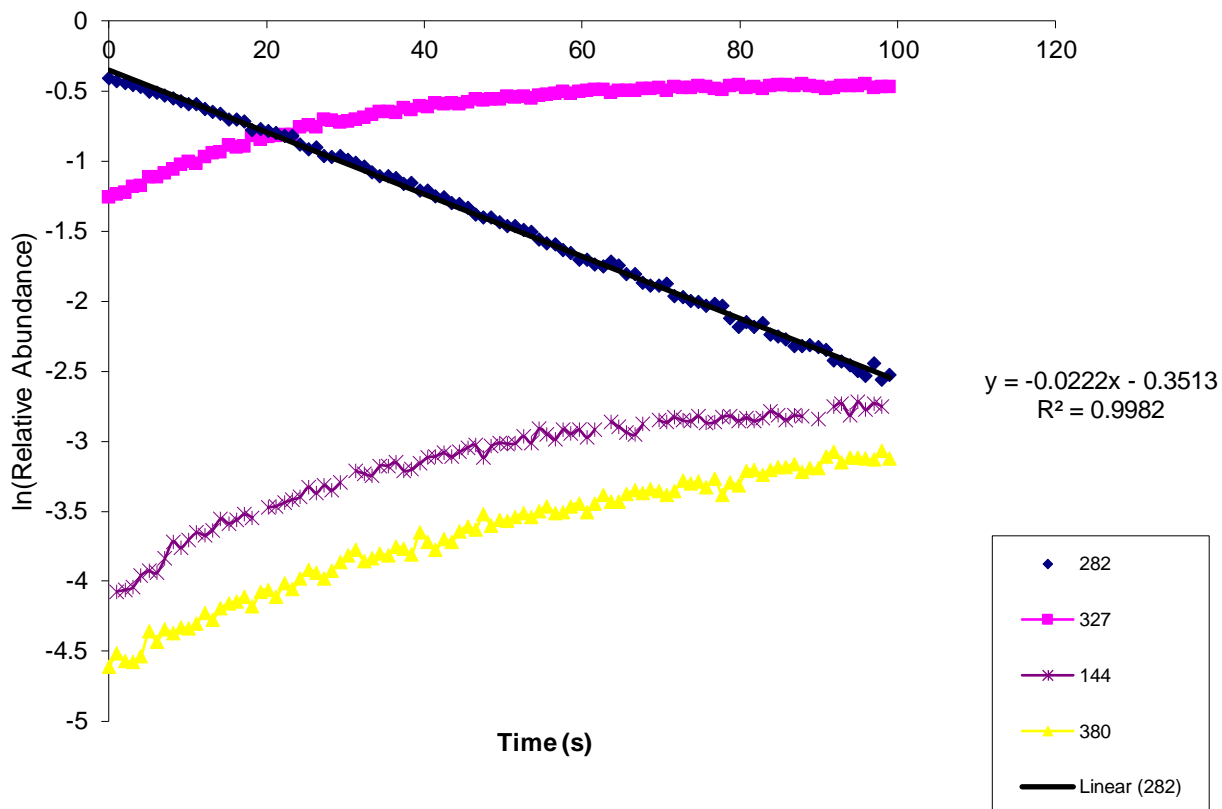


Figure 3.3 Generated graph of the log of the relative abundance of albandazole sulfoxide ions (m/z 282), protonated TDMAB (m/z 144), and albandazole reaction products (m/z 327, 380) as a function of time. The slope of the disappearance of albandazole sulfoxide ( -0.0222) is the experimental rate constant for the reaction.

Next, the theoretical collision rate constant ( $k_{\text{coll}}$ ) is approximated using experimental measurements of a collision rate-limited reaction. To do this, acetone is protonated using ESI and introduced to the ion trap. The protonated acetone and the neutral reagent react through exothermic proton transfer, which is assumed to be 100 % efficient. The slope obtained from plotting the natural log of the protonated acetone abundance as a function of time equals the theoretical collision rate constant multiplied by the neutral reagent concentration.

Finally, to calculate the reaction efficiency, the slope of the first experiment (model compound reaction) is divided by the slope of the second experiment (acetone reaction). Since both slopes contain the unknown neutral reagent concentration, dividing the two slopes negates the need to know the exact neutral reagent concentration. All reported reaction efficiencies were the average of two trials. The differences in measured reaction efficiency between trials was

always less than 0.1 %. All reaction efficiencies except for albendazole sulfoxide and quetiapine sulfoxide were calculated by Dr. Ravikiran Yerabolu.

### **3.2.5 Calculating Proton Affinities**

The proton affinities for omeprazole and omeprazole N-oxide were calculated for this chapter using previously described methods.<sup>2,26</sup> The lowest energy conformers of both the neutral and protonated compounds were calculated using Maestro 7.0.113. Gaussian<sup>25</sup> 6.0.16 at the B3LYP/6-31G++(d,p) level of theory was used to conduct both the structural optimization and the single point energy calculations. All proton affinity calculations were performed by graduate student Kawthar Zeyad Alzarieni.

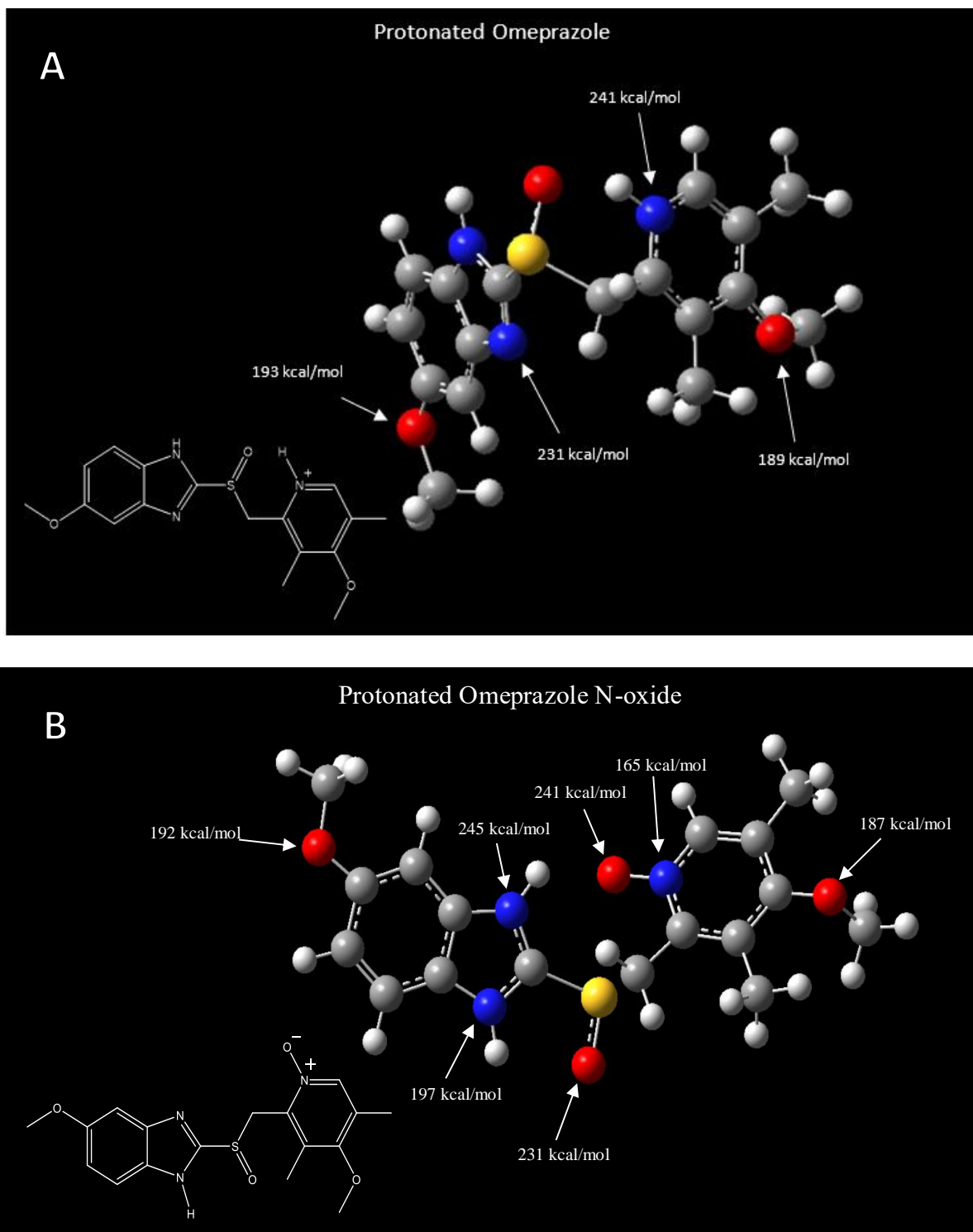


Figure 3.4 A) PA values of the most basic sites in omeprazole (shown as protonated) calculated at the B3LYP/6-31G++(d,p) level of theory. Protonation on the sulfoxide group results in the proton moving to the pyridine nitrogen atom. B) Proton affinities calculated for different protonation sites in omeprazole N-oxide at the B3LYP/6-31G++(d,p) level of theory. The site with the highest proton affinity in omeprazole N-oxide is the nitrogen in the imidazole ring the higher proton affinity of the imine nitrogen can be attributed to intramolecular hydrogen bonding (not shown).

### 3.3 Results and Discussion

#### 3.3.1 Ion-molecule Reactions (MS<sup>2</sup> experiments)

To study the factors which affect the limit of detection in gas-phase ion-molecule reactions, two model mixtures: neutral reagent pairings were chosen. The first model mixture (Table 1) consisted of seven pharmaceutical drugs and drug metabolites. The seven analytes included functional groups such as amines, alcohols, sulfones, sulfoxides, N-oxides, and carboxylic acids. The neutral reagent chosen to react with these seven compounds was tris(dimethylamino)borane (TDMAB). TDMAB is known to react with a wide variety of protonated functional groups through an addition reaction. However, TDMAB reacts differently with some specific protonated functional groups. Protonated oxygen-containing functionalities such as carboxylic acids form a TDMAB adduct followed by the elimination of methanol, as do some protonated amines. Protonated sulfones form a primary dimethylamine (DMA) adduct. In the case of protonated sulfoxides and N-oxides, TDMAB reacts to form an adduct which then loses one or two DMA molecules.<sup>4, 27</sup>

The second model mixture (Table 1) consisted of four small molecules containing either a sulfone or a sulfoxide. The neutral reagent chosen was trimethyl borate (TMB). TMB was chosen because it reacts with sulfones very differently than it reacts with sulfoxides. When reacting with protonated sulfoxides or most other protonated oxygen-containing functional groups, a TMB adduct or a TMB adduct which has lost methanol is formed. For sulfones on the other, a unique product is formed: a TMB adduct which has lost a dimethyl ether.<sup>2</sup>

When performing the ion-molecule reactions, an injection of the chosen model mixture at the desired concentration was chromatographically separated by HPLC, ionized by positive-mode electrospray ionization (ESI), and reacted with the neutral reagent of interest in the ion trap of the mass spectrometer. As each model compound eluted from the column, the resulting ions were isolated in the trap and reacted with the appropriate neutral reagent. The analyte ion and its reaction product ions were detected and recorded by the mass spectrometer in an MS<sup>2</sup> spectrum. All analytes tested here produced the expected product ions (Table 1) except for olanzapine (see Aberrant Result).

Table 3.1 Model compounds (m/z values of protonated compounds in parenthesis), detected reaction products (m/z values) and the corresponding measured reaction efficiencies. Reaction efficiencies were measured using neat compounds. The olanzapine dimethylamine (DMA) adduct was a previously unobserved reaction that appears to only occur at nanomolar and lower concentrations. The reaction efficiency could not be measured because the low concentrations at which the reaction occurs do not provide consistent enough data for efficiency measurements to be collected. <sup>a</sup> Reference 2.

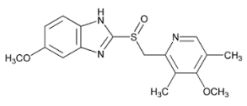
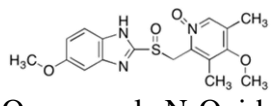
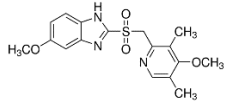
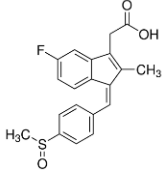
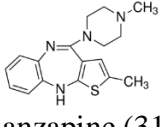
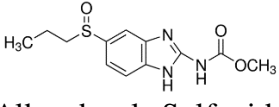
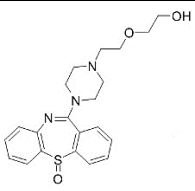
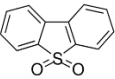
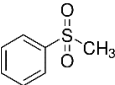
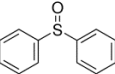
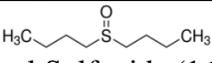
Model Mixture	Analyte (m/z)	Neutral Reagent	Product ions (m/z)	Reaction Efficiency
1	 Omeprazole (346)	TDMAB	DMA Adduct (390) TDMAB Adduct-DMA (444) TDMAB Adduct-2DMA (399)	< 1 %
	 Omeprazole N-Oxide (362)	TDMAB	DMA Adduct (406) TDMAB Adduct-DMA (460) TDMAB Adduct-2DMA (415)	< 1 %
	 Omeprazole Sulfone (362)	TDMAB	DMA Adduct (406)	< 1 %
	 Sulindac (357)	TDMAB	DMA Adduct (402) TDMAB Adduct (499) TDMAB Adduct-DMA (455)	1.4 %
	 Olanzapine (313)	TDMAB	DMA Adduct (357)	Not measured
	 Albendazole Sulfoxide (282)	TDMAB	DMA Adduct (327) TDMAB Adduct-DMA (380)	1.1 %
	 Quetiapine Sulfoxide (400)	TDMAB	DMA Adduct (444) TDMAB Adduct-DMA (498) TDMAB Adduct-2DMA (453)	< 1 %

Table 3.1 continued

2	 Dibenzothiophene Sulfone (217)	TMB	TMB Adduct (321) TMB Adduct-MeOH (289) TMB Adduct-Me <sub>2</sub> O (275)	104 % <sup>a</sup>
	 Methylphenyl Sulfone (157)	TMB	TMB Adduct (261) TMB Adduct-MeOH (229) TMB Adduct-Me <sub>2</sub> O (215)	107 % <sup>a</sup>
	 Diphenyl Sulfoxide (203)	TMB	TMB Adduct-MeOH (275)	< 1 % <sup>a</sup>
	 Butyl Sulfoxide (163)	TMB	TMB Adduct-MeOH (235)	< 1 % <sup>a</sup>

### 3.3.2 Detection Limits

Several different limits of detection were defined for the purpose of this study. First, the instrument limit of detection was defined as the lowest concentration where three replicate injections of the analyte produced an HPLC peak and a mass spectral peak with a signal-to-noise ratio of at least three. The instrument detection limit is a measure of the combined sensitivity of the HPLC and the mass spectrometer used. Since different mass spectrometers and HPLCs can produce different limits of detection (due to differences such as ion transfer efficiency etc), the same make and model of HPLC and mass spectrometer was used for all experiments. For a given model mixture, the exact same instrumentation was used for all measurements. The figure below shows the HPLC chromatograms (top) and corresponding averaged mass spectrum (bottom) of albendazole sulfoxide at four different concentrations. It is clear that 100 nM is the last concentration tested at which the signal-to-noise ratio of both the HPLC chromatogram and the mass spectral peak are at least three. At 75 nM, neither a defined HPLC peak nor a consistent mass spectral signal were detected.

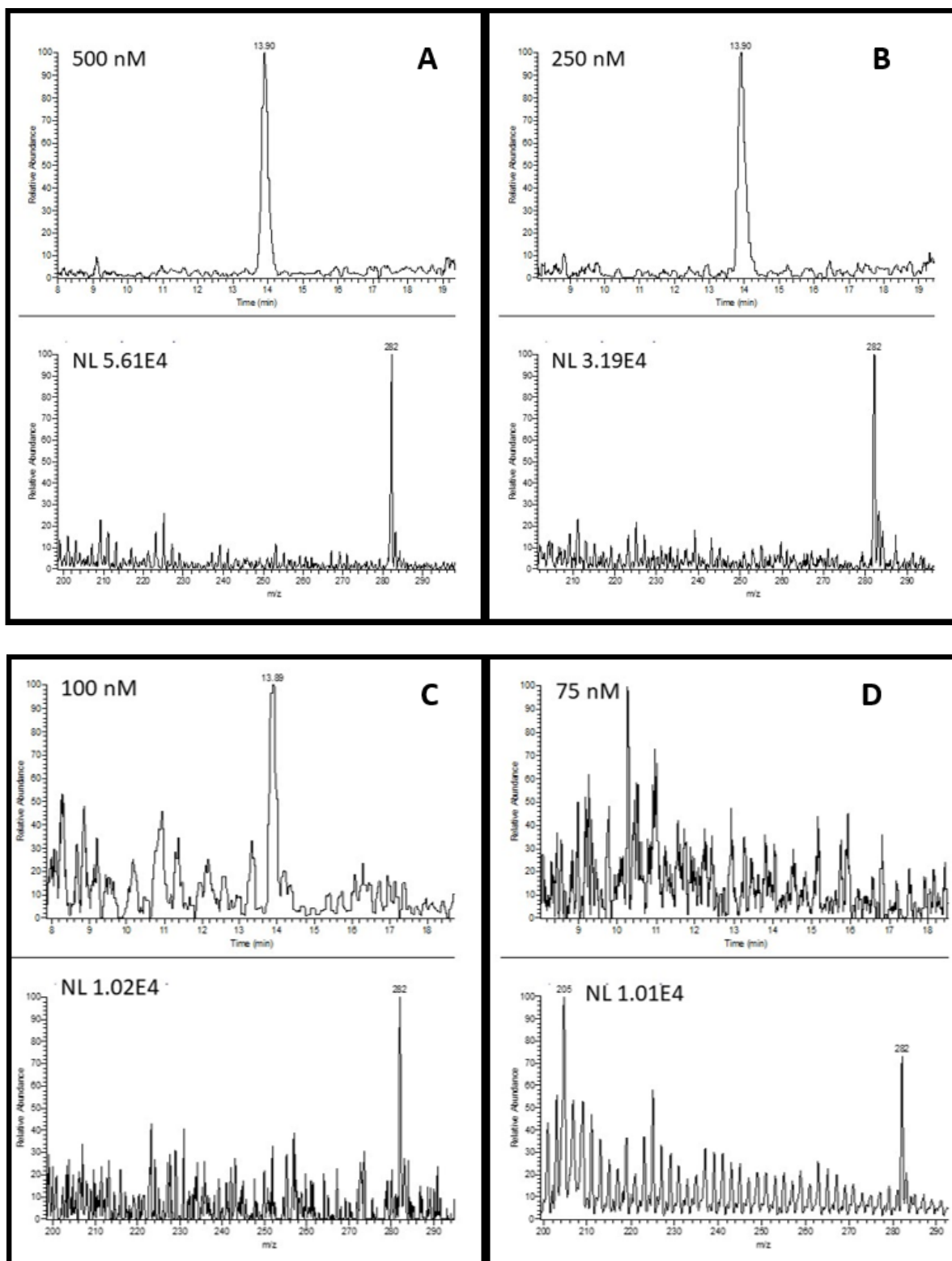


Figure 3.5 Four sets of HPLC chromatograms (top of each spectra collection) and MS spectrum (bottom of each spectra collection) for albendazole sulfoxide. The HPLC analyte peak is at 13.9 minutes and the molecular ion is at m/z 282. Each spectrum was taken at a different analyte concentration. It is clear to see that 100 nM is the limit of detection.

Next, the limit of detection for the ion-molecule reactions was established. This limit was defined as the lowest concentration where three replicate injections produced an analyte HPLC peak and mass spectral peak with a signal-to-noise of at least three AND a mass spectral peak(s) corresponding to the ion-molecule reaction products with a consistent signal-to-noise ratio of at least three.

The sensitivity of the instrumentation is the ultimate limiting factor for an ion-molecule reaction. That is, a fully-optimized ion-molecule reaction could be reproducibly seen at the instrument detection limit. An unoptimized or inefficient ion-molecule reaction would not be reproducible or observable at the instrument detection limit.

Figure 3.6 presents a typical extracted ion current HPLC chromatogram and a corresponding set of MS<sup>2</sup> spectra used to determine a limit of detection. Table 2 presents the measured instrument and ion-molecule reaction limits of detection for each analyte studied. When determining the instrument limit of detection, analytes had detection limits from 250 nM down to 50 pM, with most compounds having a detection limit between 50 and 100 nM. When measuring the ion-molecule reaction limits of detection, the analytes had detection limits within the same range: 250 nM to 50 pM with an average of 50-100 nM. Even the highest detection limit measured (250 nM), is within the previously-established range of *in vivo* concentrations, meaning that at least some ion-molecule reactions are consistent and reproducible at physiologically relevant concentrations. Considering the low reaction efficiency of many of the reactions, it was surprising that the limits of detection for the instrument and for the ion-molecule reactions were so similar. The reasoning behind this is likely because both the instrument and the ion-molecule reaction limits are dependent on the background noise in the corresponding mass spectra. The ion-molecule reaction spectra have improved signal-to-noise ratios due to the ion isolation necessary to perform the experiment. This ion isolation preserves the signal intensity of the isolated ion while drastically decreasing the background noise in the mass spectrum.

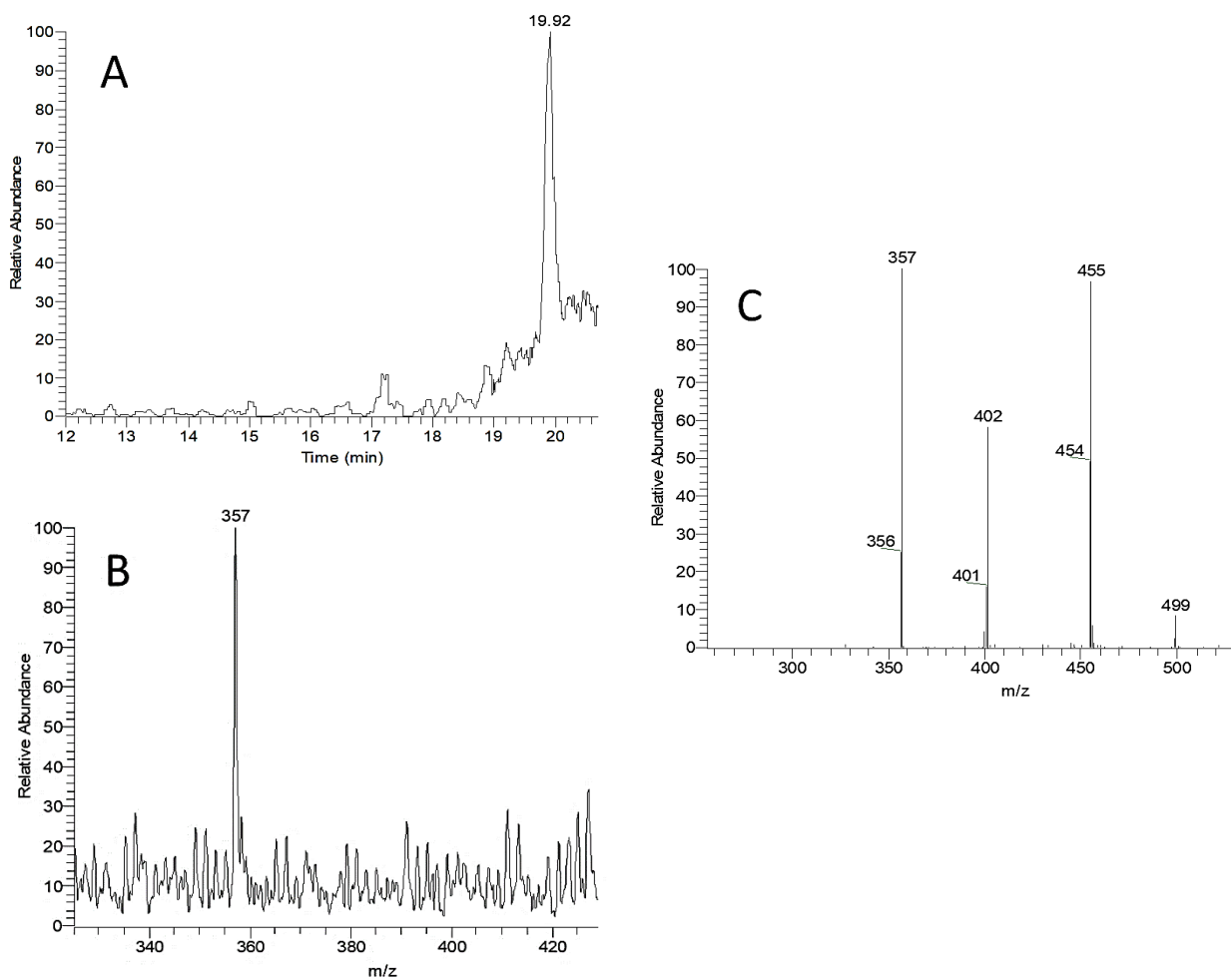


Figure 3.6 Typical extracted ion current HPLC chromatogram and a corresponding set of mass spectra used to determine the limits of detection for sulindac. The instrument detection limit is determined from: a) extracted ion HPLC chromatogram (19.80 minutes) of sulindac ( $m/z$  357) at 250 nM concentration and b) the corresponding mass spectrum of sulindac ( $m/z$  357) when no neutral reagent is present in the ion trap. Here, the ion detection (b) is the limiting factor. This was the lowest concentration tested where the signal-to-noise ratio of the  $m/z$  357 peak was at least three. The ion molecule reaction detection limit is determined from: c) the MS<sup>2</sup> spectrum of sulindac reacting with TDMAB. The peaks present correspond to protonated sulindac ( $m/z$  357) and the TDMAB reaction products [DMA adduct ( $m/z$  402), TDMAB adduct which lost a DMA ( $m/z$  455), and a TDMAB adduct ( $m/z$  499)].

Table 3.2 Model compounds (m/z), the calculated proton affinities for the most basic site, and the measured detection limits. All detection limits were determined as previously described. The proton affinities for omeprazole and omeprazole N-oxide had not been previously published and were calculated for this study (see Section 3.2.5). TDMAB and TMB proton affinities are 230 and 195 kcal/mol, respectively.<sup>3 a</sup> Reference 7. <sup>b</sup> Reference 4. <sup>c</sup> Reference 2. <sup>d</sup> The reaction of TDMAB with protonated olanzapine was only observed at nanomolar concentrations, so no limit of detection is reported.

Mixture	Compound	Neutral Reagent	PA (kcal/mol)	Instrument Detection Limit	Ion-Molecule Reaction Detection Limit
1	Omeprazole	TDMAB	241	100 nM	100 nM
	Omeprazole N-Oxide	TDMAB	245	100 nM	100 nM
	Omeprazole Sulfone	TDMAB	238 <sup>a</sup>	50 nM	50 nM
	Sulindac	TDMAB	224 <sup>b</sup>	250 nM	250 nM
	Olanzapine	TDMAB	246 <sup>b</sup>	100 nM	Not Measured <sup>d</sup>
	Albendazole Sulfoxide	TDMAB	230 <sup>b</sup>	100 nM	100 nM
	Quetiapine Sulfoxide	TDMAB	246 <sup>b</sup>	50 nM	50 nM
2	Diphenylsulfoxide	TMB	220 <sup>c</sup>	500 pM	100 nM
	Methylphenyl Sulfone	TMB	201 <sup>c</sup>	5.0 nM	5.0 nM
	Dibenzothiophene Sulfone	TMB	205 <sup>c</sup>	50 pM	50 pM
	Butyl Sulfoxide	TMB	222 <sup>c</sup>	5.0 nM	75 nM

### 3.4 Limiting Factors

Table 2 clearly shows that most ion-molecule reactions in this study had detection limits equal to the instrument detection limits. However, two compounds—diphenylsulfoxide and butyl sulfoxide—had ion-molecule detection limits that were much higher than the instrument detection limits. This finding suggests that there are factors which can inhibit the detection of ion-molecule reactions in some cases and thereby increase the limit of detection for the ion molecule reaction.

### 3.4.1 Ion Molecule Reaction Theory

Before experimentally testing the factors which might affect the limit of detection in gas-phase ion-molecule reactions, it is important to begin with a fundamental understanding of the energetics and theory of ion-molecule reactions.

The energetics of gas-phase ion molecule reactions are best described by a Brauman double-well potential energy surface, an example of which is shown below. Since the reaction takes place in the gas phase, the energy is highest for the separated reactants. When an ion and a neutral molecule collide, a lower energy reactant complex is formed. The energy reduction occurs due to the solvation energy between the ion and molecule. At this point, a chemical reaction has yet to occur. The complex can dissociate back into the separated ion and molecule reactants or the reaction can proceed. The complex can dissociate back into the separated ion and molecule reactants or the reaction can proceed.

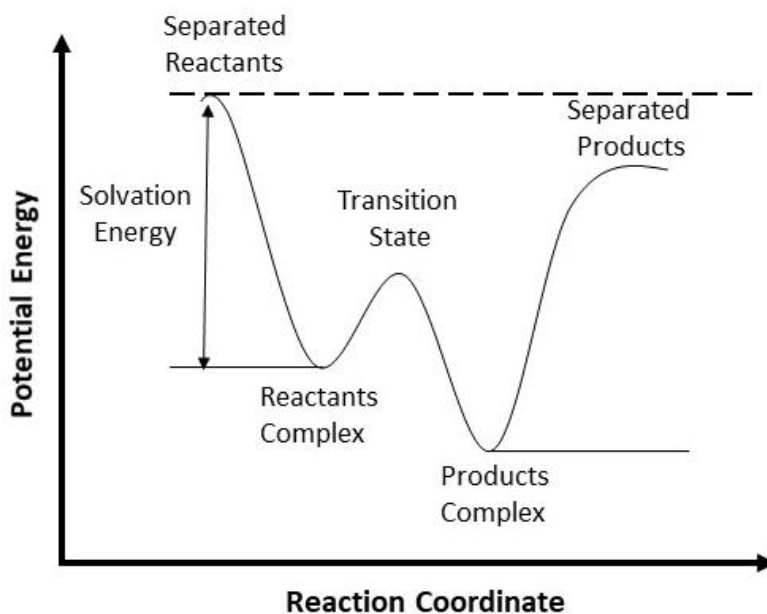


Figure 3.7 Example of a Brauman double-well potential energy surface for an exothermic ion-molecule reaction.

The first step in most ion-molecule reactions is proton transfer from the ion to the neutral molecule. For the proton transfer to occur, the gas phase basicity of the ion must be similar or lower than the gas phase basicity of the neutral molecule. This is because gas phase basicity is a measure of the stability of the protonated molecule. If the protonated analyte is significantly more stable than the protonated neutral reagent, the reaction will not occur. Since endothermic reactions

cannot occur in the vacuum of a mass spectrometer, the convention is to compare the proton affinity of the ion and the neutral molecule. Since proton affinity is the enthalpic component of the gas phase basicity, if the proton affinity of the neutral reagent is much higher than the proton affinity of the protonated analyte, the reaction is more likely to occur and will be more exothermic.

When the proton transfer occurs, most ion-molecule reactions have a transition state barrier that must be overcome. Since the gas-phase reactions for this thesis were performed inside a mass spectrometer, which is akin to performing the reactions in a vacuum, the total energy of the system cannot change during the reaction. The reaction can only proceed if the transition state and the separated products are lower in energy than the separated reactants.

Some collisions that make the reaction energetically favorable still may not result in product formation. In these cases, entropy constraints may be the culprit. A tight transition state can be the reason that product formation does not occur. In a tight transition state, the analyte ion and the neutral molecule must be in one of a minimal number of very specific orientations for a reaction to occur. In other words, the steric requirements for a reaction are very strict. By contrast, a loose transition state has less steric requirements: there are many orientations that neutral molecule and the analyte ion can be in during a collision that successfully results in product formation. If the reaction has a tight transition state, fewer collisions will meet the very specific steric requirements and proceed to product formation. From this basic understanding of ion-molecule reactions, two potential limiting factors were chosen for experimental studies: analyte proton affinity and overall reaction efficiency.

### **3.4.2 Analyte Proton Affinity**

Theoretically, during electrospray ionization, an analyte will be protonated on the most basic site within the molecule. Since the difference in proton affinity between the protonated analyte and the neutral reagent (in this case TDMAB or TMB) is of energetic importance in the reaction, it was an important factor to study. If the protonated analyte's proton affinity is too high compared to that of the neutral reagent, the reaction may not occur at all or may occur with low efficiency. In either case, the detection limit should be greatly affected and be much higher than the instrument detection limit. If the proton affinity of the neutral reagent is higher than that of the protonated analyte, then the reaction is more favorable. The greater this difference, the greater the percentage of collisions that result in a product.

To test the effect of proton affinity on the limit of detection, mixture one was studied with the TDMAB reagent (see Table 1). Mixture one was designed for this purpose because the overall TDMAB reaction efficiencies are nearly identical for each analyte (all less than 1.5%). Therefore, the differences in analyte proton affinity should be the most important factor contributing to any measured differences in ion-molecule reaction detection limits.

Proton affinities for the most basic site of each analyte (Table 2) ranged from 224 kcal/mol (sulindac) to 246 kcal/mol (olanzapine and quetiapine sulfoxide). When compared to TDMAB's proton affinity of 230 kcal/mol,<sup>3</sup> the informed reader would hypothesize that the most energetically favorable reactions would be with sulindac and albendazole sulfoxide. At first glance, this appears to be corroborated by the slightly increased reaction efficiency for these two analytes—sulindac had the greatest reaction efficiency (1.4%), followed by albendazole sulfoxide (1.1%). However, in every case, regardless of the proton affinity, the ion-molecule detection limit was the same as the instrument detection limit. A higher analyte proton affinity did not appear to inhibit the reaction enough to raise the limit of detection. Therefore, it was concluded that there is no obvious trend between the analyte proton affinity and the detection limits. Since proton affinity is only the enthalpic component of the gas phase basicity, it is possible that reactions with TDMAB tend to have entropic constraints that are a more important limiting factor than the proton affinity. That is, even when the proton affinities would predict a enthalpically favorable reaction, entropy constraints may be so great that the reaction still proceeds slowly and with low efficiency. The universally low efficiency of each analyte in model mixture 1 with TDMAB would support the argument that another factor was limiting the reaction efficiency.

### 3.4.3 Reaction Efficiency

Reaction efficiency is a measure of the fraction of all collisions which result in a reaction. Reaction efficiency is influenced by the energetic and entropic variables in a reaction: the more energetically and entropically favorable the reaction, the higher the reaction efficiency. Proton affinity is just one of many variables that sum up to the total reaction efficiency. To test how reaction efficiency affects the limit of detection in ion-molecule reactions, the four analytes in model mixture two were reacted with TMB (see Tables 1 and 2). This mixture was designed to have two compounds with very low reaction efficiencies (diphenylsulfoxide and butyl sulfoxide) and two compounds with very high reaction efficiencies (dibenzothiophene sulfone and

methylphenyl sulfone). As expected, the two compounds with the lowest reaction efficiency also have higher proton affinities. However, the proton affinity differences between the four analytes (220, 222, 205, and 201 kcal/mol) compared to TMB (195 kcal/mol) are very similar to the differences observed in model mixture one. Therefore, it can be assumed that while proton affinity may likely play a role in these reaction efficiencies, it is not the only factor.

All analytes in model mixture two had instrument detection limits between 50 pM and 5.0 nM. The two sulfones, which have high reaction efficiencies, had ion-molecule detection limits equal to the instrument detection limits. The high-efficiency reactions produced enough reaction products to enable detection even at the lowest concentration of 50 pM. However, the sulfoxides, which have very low reaction efficiencies, had significantly higher limits of detection compared to the instrument detection limits. For diphenylsulfoxide, the ion-molecule detection limit was 200 times higher than the instrument detection limit (100 nM versus 500 pM). For butyl sulfoxide, the ion-molecule detection limit was 15 times higher than the instrument detection limit (75 nM versus 5.0 nM). In these cases, the detection limit appears to greatly depend on the efficiency of the ion-molecule reactions. However, in cases where the reaction efficiency is too low for consistent product formation to be detected, the relative reaction efficiency is likely not predictive of the detection limit.

### **3.5 Ion-molecule Reactions Followed by CAD (MS<sup>3</sup> Experiments)**

Some ion-molecule reactions are not immediately diagnostic. For many neutral reagents, two or more functional groups will react with the neutral reagent, producing isobaric product ions. To differentiate such functional groups, many published diagnostic ion-molecule reactions require a second step. This step includes isolating a specific product ion and then fragmenting it using collision activated dissociation (CAD) and looking for fragments that are specific to a particular functional group.<sup>4</sup> TDMAB is a good example of a neutral reagent that is used in this way. When TDMAB reacts with a sulfoxide or an N-oxide, the same products are formed: a TDMAB adduct that lost one and/or two DMA molecules. To differentiate these two functional groups, the TDMAB adduct-DMA product is isolated and fragmented. If the unknown analyte included an N-oxide, two major fragments will be seen: a loss of DMA and a loss of HO-B(N(CH<sub>3</sub>)<sub>2</sub>)<sub>2</sub>. If, on the other hand, the analyte included a sulfoxide, an additional fragment will be seen: a loss of OB(N(CH<sub>3</sub>)<sub>2</sub>). This additional fragment can be used to distinguish the two functional groups.<sup>4</sup>

Since many ion-molecule reactions require MS<sup>3</sup> (CAD fragmentation of a product ion), it was important to look at how MS<sup>3</sup> limits of detection compare to MS<sup>2</sup> limits of detection. Firstly, unless the reaction is 100 % efficient, the number of product ions is already lower than the number of reactant ions in the ion trap. Additionally, with each subsequent ion isolation event, the ion number density inside of the ion trap decreases. In other words, the trapping efficiency isn't 100%, so some of the ions are lost every time a new isolation event is added. Since the absolute number of ions decreases, so does the resulting signal intensity. If the reaction product being isolated already has a low signal intensity, isolating those few ions and fragmenting them has the potential to result in drastically decreased sensitivity and an increased limit of detection.

To test how large an effect the isolation and fragmentation has on the limit of detection, the compounds in model mixture one were chromatographically separated, ionized, and reacted with TDMAB as previously described. For each compound with a sulfoxide or N-oxide (omeprazole, omeprazole N-oxide, sulindac, albendazole sulfoxide, and quetiapine sulfoxide), the TDMAB adduct-DMA product was isolated and fragmented. The concentration at which the fragment ions were consistent and had a signal-to-noise ratio of at least three was considered the MS<sup>3</sup> limit of detection.

Testing the product ion fragmentation at nanomolar analyte concentrations was unexpectedly difficult, especially for omeprazole, omeprazole N-oxide, and quetiapine sulfoxide. The fragment ions overall had very low signals and were irreproducible. The first scan of the products could show one set of fragments and then an entirely new set of fragments would be seen 300 ms later during the next scan. The signal intensity and irreproducibility made it difficult to distinguish fragment ions from instrumental noise. Additionally, some consistent ions weren't fragments at all. For example, when determining the MS<sup>3</sup> detection limit for albendazole sulfoxide, the TDMAB adduct-DMA product (m/z 380) was isolated and fragmented. The most abundant and consistent fragment ion was m/z 335, which would correspond to a loss of DMA. To confirm the fragment ion, the extracted ion current for m/z 335 was compared to the extracted ion current of albendazole sulfoxide. Albendazole sulfoxide's retention time was 14.02 minutes. If m/z 335 was a true fragment of the albendazole TDMAB adduct-DMA, there should be a corresponding increase in signal intensity at 14.02 minutes, indicating that the m/z 335 being analyzed originated from the albendazole sulfoxide. Unfortunately, this was not the case: m/z 335 showed no signal increase at 14.02 minutes, suggesting that it was not a true fragment ion. It's possible that m/z 335

was background noise or originated from an isobaric ion that was simultaneously isolated along with the TDMAB adduct-DMA ion.

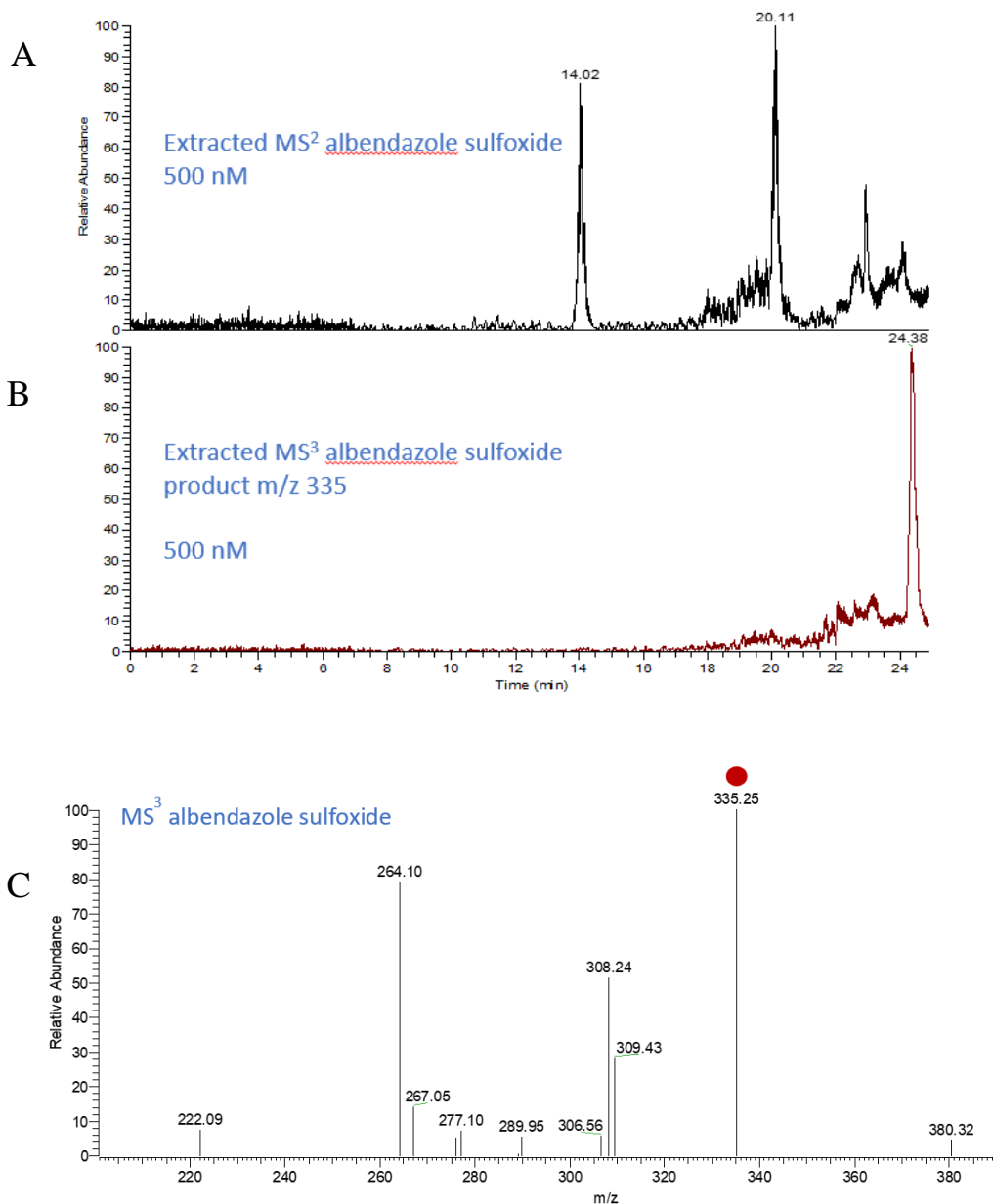


Figure 3.8 MS<sup>2</sup> and MS<sup>3</sup> spectra for albendazole sulfoxide (m/z 282) at a concentration of 500 nM. A) shows the extracted ion HPLC chromatogram, with albendazole sulfoxide eluting at 14.02 minutes. C) shows fragmentation (MS<sup>3</sup>) spectra of the albendazole sulfoxide TDMAB adduct-DMA ion (m/z 380). The most abundant fragment ion is m/z 335 (assumed to be a loss of DMA). B) is the extracted ion current of m/z 335. The ion abundance of m/z 335 does not increase at all during the elution time of albendazole sulfoxide, suggesting that it is not a real fragment ion.

For some analytes, including quetiapine sulfoxide, no HPLC/MS tests produced reproducible fragmentation. This may be because ion-molecule reactions are not developed using compounds eluting from HPLC. Therefore, for these analytes, the neat analyte solution was directly injected into the ion source for testing (see Table 3).

The measured limits of detection for the MS<sup>3</sup> experiments and for the corresponding MS<sup>2</sup> ion-molecule reaction experiments are shown in Table 3. In general, there was a dramatic difference between the ion-molecule and MS<sup>3</sup> detection limits. The MS<sup>3</sup> detection limits were up to two orders of magnitude higher than the ion-molecule reaction detection limits, suggesting that isolating and fragmenting an ion-molecule reaction product can dramatically decrease the sensitivity of the method. Therefore, this is considered a primary limiting factor. Sulindac was a notable exception because it had an MS<sup>3</sup> detection limit equal to both its ion-molecule and its instrument detection limit. A possible explanation is because sulindac had such a notably high instrument limit of detection, suggesting that the instrument detection (ionization efficiency and ion optic transfer efficiency) were the limiting factor for this particular analyte. If the ionization efficiency and ion optic transfer efficiency were improved, it is possible that the instrument and ion-molecule detection limits would be lower than the MS<sup>3</sup> detection limit.

One possible reason why model mixture one had MS<sup>3</sup> detection limits so much higher than the ion-molecule detection limits could be the reaction efficiencies of the analytes. When reacted with TDMAB, all of the analytes had reaction efficiencies of less than 1.5 %. This low reaction efficiency lead to products with correspondingly low abundances. Isolating and fragmenting an already low-abundance product is probably at least partially responsible for the dramatic difference between the ion-molecule and MS<sup>3</sup> detection limits.

To test whether the MS<sup>3</sup> detection limits are closer to the ion-molecule detection limits for efficient reactions, a separate small study was conducted using methyl phenyl sulfone from model mixture two. Methyl phenyl sulfone has a  $107 \pm 0.1$  % reaction efficiency when reacted with TMB (Table 1) and produces correspondingly large amounts of product ions. The reaction efficiency was measured at over 100 % due to the experimental approximation of the theoretical collision rate constant and would suggest that the literature approximation may need revising. While its reaction products do not need to be isolated and fragmented to identify the sulfone functionality, it was still possible to determine a detection limit based on fragmenting one of the product ions. The most abundant reaction product (TMB adduct -methanol) was isolated and fragmented. This

time, reproducible fragments were formed at much lower concentrations. The limit of detection for the fragmentation was 250 nM, five times the ion-molecule reaction detection limit. This was very similar to some of the model mixture one results, but much better than the micromolar detection limits seen for two of the model mixture one compounds. From this limited data, it can be concluded that MS<sup>3</sup> experiments will usually be a primary factor in determining the limit of detection, but that high-efficiency reactions may suffer less from this effect than low-efficiency reactions.

Table 3.3 The TDMAB ion-molecule reaction detection limits and the MS<sup>3</sup> (product ion isolation and fragmentation) detection limits for model mixture one. <sup>a</sup> Results obtained using direct injection. No reproducible MS<sup>3</sup> spectra could be obtained in HPLC/MS<sup>3</sup> experiments.

Analyte	Ion-Molecule Reaction Detection Limit	MS <sup>3</sup> Detection Limit
Omeprazole	100 nM	5.0 μM <sup>a</sup>
Omeprazole N-Oxide	100 nM	250 nM
Sulindac	250 nM	250 nM
Albendazole Sulfoxide	100 nM	250 nM
Quetiapine Sulfoxide	50 nM	5.0 μM <sup>a</sup>

### 3.6 Aberrant Result

This study purposefully included the analyte olanzapine in model mixture one to serve as a control. Olanzapine is a polyfunctional pharmaceutical and includes an amine but no oxygen-containing functional groups, which are the hallmark reaction sites for TDMAB. In previous studies, olanzapine has never reacted with TDMAB, and its lack of reactivity helped inform the understanding of how TDMAB reacts with different organic functional groups.<sup>4</sup> Therefore, it was assumed that olanzapine would be a good control for the study. Unfortunately, at low concentrations ( $\leq 100$  nM), olanzapine did react with TDMAB to form a DMA adduct, a reaction that had previously been assumed indicative of an oxygen-containing functionality, which olanzapine does not have.

Previous fundamental studies have indicated that polyfunctional analytes can have protomers which can be simultaneously separated and detected by mass spectrometry.<sup>28-30</sup> That is: one analyte can be protonated at more than one location, and any of those locations has the potential to react and react differently with a neutral molecule. The relative abundance of different protomers for an analyte can shift depending on solvent composition, analyte concentration, and other factors.<sup>31,32</sup> It's clear from our initial investigations that the reaction between TDMAB and olanzapine arises from an unanticipated protomer of olanzapine that is present only at low concentrations. However, the exact reason for the change in protomers at low concentrations has not been fully explained in the case of olanzapine and is the subject of current studies by Rashmi Kumar.

### 3.7 Conclusions and Future Outlook

Diagnostic gas-phase ion-molecule reactions inside a mass spectrometer have been put forth as a new way to identify the structures of unknown drug metabolites. This study, which coupled HPLC with ion-molecule reactions in an ion-trap mass spectrometer, has shown that at least some of these diagnostic reactions are sensitive and reproducible enough for use at physiologically relevant concentrations. Three potential factors which could affect the limit of detection in these ion-molecule reactions were studied. Both the reaction efficiency and the number of ion isolation steps ( $MS^2$  vs  $MS^3$ ) proved to be important in some cases. The analyte proton affinity, however, was not a predictive influence on the limit of detection. From the results of this study, the most successful ion-molecule reactions will have high reaction efficiencies and require only  $MS^2$  (no product isolation and fragmentation). For these optimal reactions, the detection limits could approach the instrument detection limits of most mass spectrometers.

However, the news is not all positive. This study has also highlighted some fundamental challenges with the use of ion-molecule reactions to identify specific functional groups. When preparing for this study, I noted that many papers on the topic did not include the analyte concentrations that were used or were decidedly vague on the topic.<sup>5,7,33-36</sup> Additionally, many of the “diagnostic” reactions in the literature included very few controls with analytes containing other functional groups,<sup>2,9,12</sup> suggesting that some of the accepted diagnostic reactions may not be as specific as their corresponding papers suggest. For example, in several publications, neutral reagents are said to be unreactive with a particular functional group based on the reaction with a single compound of that functionality.<sup>2,9,12</sup> Other publications included no controls at all, but only

used the reactions to separate two or three different functionalities without any additional testing.<sup>34,37</sup> Still others published limited tests that included false positives.<sup>4</sup> Without rigorous testing, it is my opinion that many of these ion-molecule reactions should not be considered diagnostic at this point in time.

The work presented here clearly indicates that MS<sup>3</sup> ion-molecule reactions—where the reaction product is isolated and then fragmented—are not generally suitable for use at physiological concentrations. Unfortunately, a large number of diagnostic reactions developed in this lab rely on MS<sup>3</sup> and therefore are not candidates for *in vivo* metabolite studies. Of the neutral reagents used to identify different functional groups in this lab, many require MS<sup>3</sup> for identification.<sup>2,7,10,38</sup> This drawback is not insignificant and highlights the need for developing new reactions that better address the needs of metabolite identification.

Finally, the aberrant case of olanzapine is an illustrative example of a fundamental flaw in the field of diagnostic ion-molecule reactions: the assumption that all ion-molecule reactions are initiated by proton-transfer at the most basic site in the analyte molecule. We now know that this is not always the case: olanzapine has different protomers at low concentrations than it does at higher concentrations. Other analytes that behave in this fashion have also been identified by other members of our research group, but the results have yet to be submitted for publication. The case of olanzapine suggests that some polyfunctional metabolites will react differently depending on their concentration. Without prior knowledge of the analyte's structure, proton affinities, and concentration, positively identifying such an unknown drug metabolite would be impossible. This huge potential for false positives or negatives should be considered of primary concern in this field, but as yet has not been addressed and no solutions have been found. Therefore, it is my belief that ion-molecule reactions should not be used as the only means of identifying a drug metabolite but should instead be used only in conjunction with other identification techniques.

### 3.8 References

1. Niyonsaba, E.; Easton, M.W.; Feng, E.; Yu, Z.; Zhang, Z.; Sheng, H.; Kong, J.; Easterling, L.F.; Milton, J.; Chobanian, H.R.; Deprez, N.R.; Cancilla, M.T.; Kilaz, G.; Kenttämä, H.I. Differentiation of Deprotonated Acyl-, *N*-, and *O*-Glucuronide Drug Metabolites by Using Tandem Mass Spectrometry Based on Gas-Phase Ion-Molecule Reactions Followed by Collision-Activated Dissociation. *Anal. Chem.* **2019**, *91*, 11388-11396.

2. Sheng, H.; Williams, P.E.; Tang, W.; Riedeman, J.S.; Zhang, M.; Kenttämää, H.I. Identification of the Sulfone Functionality in Protonated Analytes via Ion/Molecule Reactions in a Linear Quadrupole Ion Trap Mass Spectrometer. *J. Org. Chem.* **2014**, *79*, 2883-2889.
3. Zhang, M.; Eismin, R.; Kenttämää, H.I.; Xiong, H.; Wu, Y.; Burdette, D.; Urbanek, R. Identification of 2-Aminothiazolobenzazepine Metabolites in Human, Rat, Dog, and Monkey Microsomes by Ion-Molecule Reactions in Linear Quadrupole Ion Trap Mass Spectrometry. *Drug Metab. Dispos.* **2015**, *43*, 358-366.
4. Sheng, H.; Tang, W.; Yerabolu, R.; Max, J.; Kotha, R.R.; Riedeman, J.S.; Nash, J.J.; Zhang, M.; Kenttämää, H.I. Identification of *N*-Oxide and Sulfoxide Functionalities in Protonated Drug Metabolites by Using Ion-Molecule Reactions Followed by Collisionally Activated Dissociation in a Linear Quadrupole Ion Trap Mass Spectrometer. *J. Org. Chem.* **2016**, *81*, 575-586.
5. Tang, W.; Sheng, H.; Kong, J.Y.; Yerabolu, R.; Zhu, H.; Max, J.; Zhang, M.; Kenttämää, H.I. Gas-Phase Ion-Molecule Reactions for the Identification of the Sulfone Functionality in Protonated Analytes in a Linear Quadrupole Ion Trap Mass Spectrometer. *Rapid Commun. Mass Spectrom.* **2016**, *30*, 1435-1441.
6. Zhu, H.; Ma, X.; Kong, J.Y.; Zhang, M.; Kenttämää, H.I. Identification of Carboxylate, Phosphate, and Phenoxide Functionalities in Deprotonated Molecules Related to Drug Metabolites via Ion-Molecule Reactions with Water and Diethylhydroxyborane. *J. Am. Soc. Mass Spectrom.* **2017**, *28*, 2189-2200.
7. Yerabolu, R.; Kong, J.; Easton, M.; Kotha, R.; Max, J.; Sheng, H.; Gu, C.; Kenttämää, H.I. Identification of Protonated Sulfone and Aromatic Carboxylic Acid Functionalities in Organic Molecules by Using Ion-Molecule Reactions Followed by Collisionally Activated Dissociation in a Linear Quadrupole Ion Trap Mass Spectrometer. *Anal. Chem.* **2017**, *89*, 7398-7405.
8. Zhu, H.; Max, J.P.; Marcum, C.L.; Luo, H.; Abu-Omar, M.M.; Kenttämää, H.I. Identification of the Phenol Functionality in Deprotonated Monomeric and Dimeric Lignin Degradation Products via Tandem Mass Spectrometry Based on Ion-Molecule Reactions with Diethylmethoxyborane. *J. Am. Soc. Mass Spectrom.* **2016**, *27*, 1813-1823.
9. Sheng, H.; Tang, W.; Yerabolu, R.; Kong, J.Y.; Williams, P.E.; Zhang, M.; Kenttämää, H.I. Mass Spectrometric Identification of the *N*-Monosubstituted *N*-Hydroxylamino Functionality in Protonated Analytes via Ion/Molecule Reactions in Tandem Mass Spectrometry. *Rapid Commun. Mass Spectrom.* **2015**, *29*, 730-734.
10. Eismin, R.J.; Fu, M.; Yem, S.; Widjaja, F.; Kenttämää, H.I. Identification of Epoxide Functionalities in Protonated Monofunctional Analytes by Using Ion/Molecule Reactions and Collision-Activated Dissociation in Different Ion Trap Tandem Mass Spectrometers. *J. Am. Soc. Mass Spectrom.* **2012**, *23*, 12-22.
11. Habicht, S.C.; Vinueza, N.R.; Amundson, L.M.; Kenttämää, H.I. Comparison of Functional Group Selective Ion-Molecule Reactions of Trimethyl Borate in Different Ion Trap Mass Spectrometers. *J. Am. Soc. Mass Spectrom.* **2011**, *22*, 520-530.

12. Sheng, H.; Williams, P.E.; Tang, W.; Zhang, M.; Kenttämaa, H.I. Identification of the Sulfoxide Functionality in Protonated Analytes via Ion/Molecule Reactions in Linear Quadrupole Ion Trap Mass Spectrometry. *Analyst* **2014**, *139*, 4296-4302.
13. Jia, L.; Liu, X. The Conduct of Drug Metabolism Studies Considered Good Practice (II): In Vitro Experiments. *Curr. Drug. Metab.* **2007**, *8*, 822-829.
14. Roškar, R.; Lušin, T.T. Analytical Methods for Quantification of Drug Metabolites in Biological Samples, In *Chromatography, the Most Versatile Method of Chemical Analysis*, Calderon, L. (Ed); IntechOpen: London, **2014**, pp.79-126.
15. U.S. Department of Health and Human Services, Food and Drug Administration, Center for Drug Evaluation and Research. *Safety Testing of Drug Metabolites: Guidance for Industry*. **2016**.
16. Dudda, A.; Kuerzel, G.U. Metabolism Studies In Vitro and In Vivo, In *Drug Discovery and Evaluation: Safety and Pharmacokinetic Assays*, Vogel, H.G.; Maas, J.; Hock, F.J.; Mayer, D. (Eds); Springer: Berlin, **2013**, 1053-1094.
17. Duarte, J.D. A Look to the Future: Cardiovascular Pharmacoeigenetics, In *Pharmacogenomics*; Lam, Y-W. F.; Cavallari, L.H. (Eds); Academic Press: San Diego, **2013**, 183-189.
18. Field, M.J.; Harris, D.C.; Pollock, C.A. Drugs and the Kidney, In *The Renal System*, 2<sup>nd</sup> Ed., Churchill Livingstone: London, **2010**, 149-157.
19. Teasdale, A.; Elder, D.P. Analytical Control Strategies for Mutagenic Impurities: Current Challenges and Future Opportunities. *Trends Anal. Chem.* **2018**, *101*, 66-84.
20. Hiemke, C.; Baumann, P.; Bergemann, N.; Conca, A.; Dietmaier, O.; Egberts, K.; Fric, M.; Gerlach, M.; Greiner, C.; Gründer, G.; Haen, E.; Havemann-Reinecke, U.; Sirot, E.J.; Kirchherr, H.; Laux, G.; Lutz, U.C.; Messer, T.; Müller, M.J.; Pfuhlmann, B.; Rambeck, B.; Riederer, P.; Schoppek, B.; Stingl, J.; Uhr, M.; Ulrich, S.; Waschgler, R.; Zernig, G. AGNP Consensus Guidelines for Therapeutic Drug Monitoring in Psychiatry: Update 2011. *Pharmacopsychiatry* **2011**, *44*, 195-235.
21. Viinamäki, J.; Ojanperä, I. Concurrent Estimation of Metabolite Concentrations Along with Parent Drug Quantification in Post-Mortem Blood. *Forensic Sci. Int.* **2016**, *267*, 110-114.
22. Habicht, S. C.; Vinueza, N. R.; Archibold, E.; Duan, P.; Kenttämaa, H. I. Identification of the Carboxylic Acid Functionality by Using Electrospray Ionization and Ion-Molecule Reactions in a Modified Linear Quadrupole Ion Trap Mass Spectrometer. *Anal. Chem.* **2008**, *80*, 3416-3421.
23. Gao, H.; Petzold, C.J.; Leavell, M.D.; Leary, J.A. Investigation of Ion/Molecule Reactions as a Quantification Method for Phosphorylated Isomers: An FT-ICR Approach. *J. Am. Soc. Mass Spectrom.* **2003**, *14*, 916-924.

24. Su, T.; Chesnavich, W.J. Parametrization of the Ion-Polar Molecule Collision Rate Constant by Trajectory Calculations. *J. Chem. Phys.* **1982**, *76*, 5183-5184.
25. Frisch, M. J.; Trucks, G. W.; Schlegel, H. B.; Scuseria, G. E.; Robb, M. A.; Cheeseman, J. R.; Montgomery, J. A., Jr.; Vreven, T.; Kudin, K. N.; Burant, J. C.; Millam, J. M.; Iyengar, S. S.; Tomasi, J.; Barone, V.; Mennucci, B.; Cossi, M.; Scalmani, G.; Rega, N.; Petersson, G. A.; Nakatsuji, H.; Hada, M.; Ehara, M.; Toyota, K.; Fukuda, R.; Hasegawa, J.; Ishida, M.; Nakajima, T.; Honda, Y.; Kitao, O.; Nakai, H.; Klene, M.; Li, X.; Knox, J. E.; Hratchian, H. P.; Cross, J. B.; Bakken, V.; Adamo, C.; Jaramillo, J.; Gomperts, R.; Stratmann, R. E.; Yazyev, O.; Austin, A. J.; Cammi, R.; Pomelli, C.; Ochterski, J. W.; Ayala, P. Y.; Morokuma, K.; Voth, G. A.; Salvador, P.; Dannenberg, J. J.; Zakrzewski, V. G.; Dapprich, S.; Daniels, A. D.; Strain, M. C.; Farkas, O.; Malick, D. K.; Rabuck, A. D.; Raghavachari, K.; Foresman, J. B.; Ortiz, J. V.; Cui, Q.; Baboul, A. G.; Clifford, S.; Cioslowski, J.; Stefanov, B. B.; Liu, G.; Liashenko, A.; Piskorz, P.; Komaromi, I.; Martin, R. L.; Fox, D. J.; Keith, T.; Al-Laham, M. A.; Peng, C. Y.; Nanayakkara, A.; Challacombe, M.; Gill, P. M. W.; Johnson, B.; Chen, W.; Wong, M. W.; Gonzalez, C.; Pople, J. A. Gaussian 03, revision C.02; Gaussian, Inc.: Wallingford, CT, 2003.
26. Hunter, E. P.; Lias, S. G. Proton Affinity Evaluation. In NIST Chemistry WebBook, NIST Standard Reference Database Number 69; Linstrom, P. J., Mallard, W. G., Eds.; National Institute of Standards and Technology: Gaithersburg, MD, 2013.
27. Duan, P.; Fu, M.; Gillespie, T.A.; Winger, E.; Kenttämä, H.I. Identification of Aliphatic and Aromatic Tertiary N-Oxide Functionalities in Protonated Analytes via Ion/Molecule and Dissociation Reactions in an FT-ICR Mass Spectrometer. *J. Org. Chem.* **2009**, *74*, 1114-1123.
28. Marlton, S.J.P.; McKinnon, B.I.; Ucur, B.; Maccarone, A.T.; Donald, W.A.; Blanksby, S.J.; Trevitt, A.J. Selecting and Identifying Gas-Phase Protonation Isomers of NicotineH<sup>+</sup> Using Combined Laser, Ion Mobility and Mass Spectrometry Techniques. *Faraday Discuss.* **2019**, *217*, 453-475.
29. Matthews, E.; Dessent, C.E.H. Experiment and Theory Confirmed That UV Laser Photodissociation Spectroscopy can Distinguish Protomers Formed *via* Electrospray. *Phys. Chem. Chem. Phys.* **2019**, *19*, 17343-17440.
30. McCullagh, M.; Giles, K.; Richardson, K.; Stead, S.; Palmer, M. Investigations into the Performance of Travelling Wave Enabled Conventional and Cyclic Ion Mobility Systems to Characterise Protomers of Fluoroquinolone Antibiotic Residues. *Rapid Commun. Mass Spectrom.* **2018**, *33*, 11-21.
31. Xia, H.; Attygalle, A.B. Transformation of the Gas-Phase Favored *O*-Protomer of *p*-Aminobenzoic Acid to its Unfavored *N*-Protomer by Ion Activation in the Presence of Water Vapor: An Ion-Mobility Mass Spectrometry Study. *J. Mass Spectrom.* **2018**, *53*, 353-360.
32. Xia, H.; Attygalle, A.B. Untrapping Kinetically Trapped Ions: The Role of Water Vapor and Ion-Source Activation Conditions on the Gas-Phase Protomer Ratio of Benzocaine Revealed by Ion-Mobility Mass Spectrometry. *J. Am. Soc. Mass Spectrom.* **2017**, *28*, 2580-2587.

33. Kong, J.Y.; Yu, Z.; Easton, M.W.; Niyonsaba, E.; Ma, X.; Yerabolu, R.; Sheng, H.; Harrell, T.M.; Zhang, Z.; Ghosh, A.K.; Kenttämäa, H.I. Differentiating Isomeric Deprotonated Glucuronide Drug Metabolites via Ion/Molecule Reactions in Tandem Mass Spectrometry. *Anal. Chem.* **2018**, *90*, 9426-9433.
34. Fu, M.; Duan, P.; Gao, J.; Kenttämäa, H.I. Ion-Molecule Reactions for the Differentiation of Primary, Secondary, and Tertiary Hydroxyl Functionalities in Protonated Analytes in a Tandem Mass Spectrometer. *Analyst* **2012**, *137*, 5720-5722.
35. Gqamana, P.P.; Duan, P.; Fu, M.; Gallardo, V.; Kenttämäa, H.I. A Novel Chemical Ionization Reagent Ion for Organic Analytes: The Aquachloromanganese(II) Cation [ClMn(H<sub>2</sub>O)<sup>+</sup>]. *Rapid Commun. Mass Spectrom.* **2012**, *26*, 940-942.
36. Somuramasami, J.; Duan, P.; Amundson, L.M.; Archibold, E.; Winger, B.E.; Kenttämäa, H.I. Differentiation of Protonated Aromatic Regioisomers Related to Lignin by Reactions with Trimethylborate in a Fourier Transform Ion Cyclotron Resonance Mass Spectrometer. *J. Am. Soc. Mass Spectrom.* **2011**, *22*, 1040-1051.
37. Fu, M.; Eismän, R.J.; Duan, P.; Li, S.; Kenttämäa, H.I. Ion-Molecule Reactions Facilitate the Identification and Differentiation of Primary, Secondary and Tertiary Amino Functionalities in Protonated Monofunctional Analytes in Mass Spectrometry. *Int. J. Mass Spectrom.* **2009**, *282*, 77-84.
38. Watkins, M.A.; Price, J.M. Winger, B.E.; Kenttämäa, H.I. Ion-Molecule Reactions for Mass Spectrometric Identification of Functional Groups in Protonated Oxygen-Containing Monofunctional Compounds. *Anal. Chem.* **2004**, *76*, 964-976.

## CHAPTER 4. A STUDY OF ELECTROSPRAY IONIZATION-INDUCED OXIDATION OF SULFUR-CONTAINING COMPOUNDS

### 4.1 Introduction

Many complex mixtures contain sulfur compounds such as thiols. These mixtures are diverse in composition and include biological systems,<sup>1,2</sup> heavy crude oils,<sup>3,4</sup> organic synthesis mixtures,<sup>5,6</sup> and more. When analyzing these complex mixtures, it is vastly important to choose the correct instrumentation and conditions to produce easily interpreted data. Mass spectrometry has emerged as one of, if not *the*, most powerful tool for analyzing complex mixtures, and electrospray ionization (ESI) has gained traction as the ionization method of choice for many analyses. However, sulfur-containing compounds are difficult to analyze using ESI because they tend to have very low ionization efficiencies.<sup>7,8</sup> Therefore, numerous researchers have developed new ESI-based techniques to circumnavigate this problem. These techniques include chemical derivatization,<sup>8</sup> chromatographic separation,<sup>9</sup> and complexation with Ag<sup>+</sup>.<sup>7,10</sup> These new techniques have had varying degrees of success, resulting in complex and difficult to interpret data. The side reactions that can occur during electrospray ionization are at least partially to blame for the complex data produced during these experiments.

In a typical ESI analysis, the analyte is ionized by the addition or removal of a proton, which produces a pseudomolecular ion:  $[M+H]^+$  in positive mode or  $[M-H]^-$  in negative mode.<sup>11,12</sup> (For a more detailed overview of traditional ESI, see Chapter 2.) These pseudomolecular ions have a mass-to-charge ( $m/z$ ) ratio either one unit greater or smaller compared to the analyte's molar mass (greater in positive mode and smaller in negative mode). This shift of one  $m/z$  unit makes identifying the analyte's molar mass possible, which can ultimately help in identifying the analyte. However, in complex mixture analysis, this identification technique relies on two main assumptions: that the pseudomolecular ion for each analyte is easily identifiable and that every analyte in the mixture produces a pseudomolecular ion and nothing else. However, these two assumptions do not always hold true. Under atypical ESI conditions—including low flow rates, relatively high voltages, or with easily oxidized or reduced analytes—electrochemical and other reactions can take place.<sup>13,14</sup>

Since its invention, ESI has been known to function as a controlled-current electrolytic cell.<sup>13,14</sup> Depending on the mode the ESI source is operated in, radical cations and radical anions

can be formed. In negative mode, reduction in the ESI source leads to radical anion production, a process that usually occurs with analytes with standard reduction potentials less than one (versus the standard calomel electrode).<sup>15</sup> In positive mode, electrochemical oxidation can lead to radical cation formation, although this process is less common and the resulting radical cations are often too unstable or reactive to be detected by the mass spectrometer.<sup>15</sup> It is easy to see how highly reactive radical ions could lead to complicated ESI data by initiating reactions<sup>16</sup> within the ESI source, the products of which can potentially be detected by the mass spectrometer.

However, electrochemical oxidation and reduction is not the only non-standard process that occurs in atypical ESI experiments. Recently, it has been shown that ESI operated at low flow rates and relatively high voltages produces a corona discharge at the tip of the ESI needle.<sup>17-19</sup> A corona discharge is a buildup of electrical charge that produces a relatively low-energy plasma in the surrounding gas<sup>20</sup> and is most often associated in mass spectrometry with atmospheric pressure chemical ionization (APCI).<sup>21</sup> Depending on the solvent used, the gas inside the ion source (usually nitrogen), and the polarity of the discharge, the ions and plasma zone can vary widely.<sup>22</sup> However, some common species found within these plasmas includes hydroxy radicals, ozone, and hydrogen peroxide.<sup>23</sup> In ESI, the plasma formation is linked to analyte oxidation and reduction, most likely through radical and ion-molecule reactions within the plasma.<sup>20</sup> While the plasma forms in both positive and negative polarities, the plasma formed from a negative polarity experiment produces slow-moving electrons that can propagate a portion of the current up to several centimeters from the discharge, ultimately increasing the affected area.<sup>22</sup> Therefore, negative polarity ESI corona discharges have a greater chance of altering the analyte during ionization and changing the resulting mass spectrum.

Recently, researchers have begun utilizing the corona discharge produced during atypical ESI experiments. In particular, research has focused on the ozone which is generated by the plasma. Ozone is a highly reactive gas and is believed to be generated in the plasma through a multi-step process that starts with the splitting of atmospheric oxygen and ends in the formation of ozone along with other radical and reactive species.<sup>25</sup> A detailed and exhaustive review of ozone formation was written by Chen and Davidson.<sup>25</sup>

The technique of utilizing ESI-induced ozone to oxidize analytes is called OzESI-MS.<sup>17</sup> The technique does not involve any changes to the instrument itself and can be performed with unmodified mass spectrometers. A constant flow of oxygen gas and very high ESI voltages are

used to increase ozone formation within the ESI source. This technique has most notably been to locate carbon-carbon double bonds in unsaturated lipids based on the resulting ozonolysis reactions.<sup>18,19</sup> However, this technique is still in its infancy, and the reactions between ESI-produced ozone and other kinds of analytes has not been exhaustively studied. Indeed, it is not even established if the exceptionally high voltages and oxygen gas used in OzESI-MS are necessary to produce sufficient ozone formation for ozonolysis reactions. Since the technique is still being developed, it is possible that for some analytes and mixtures, ESI-produced ozone may generate unexpected ions that introduce additional complexity into the mass spectra and greatly complicate data analysis.

Since sulfur compounds are found in so many complex mixtures and biological systems, understanding the behavior of sulfur compounds in atypical corona discharge ESI experiments is of increasing importance. While oxidation and ozonolysis products have been reported during corona discharge ESI experiments for other compounds, neither the types of oxidation products formed for sulfur-containing analytes during these experiments nor their mechanism of formation is fully known. This knowledge gap may make positively identifying sulfur compounds in complex mixtures difficult when atypical ESI conditions are used. This study was performed to help fill this fundamental gap in knowledge and explores the complex chemistry involved in the analysis of thiols and other sulfur-containing compounds when ionized by corona discharge ESI. In this paper, the factors which both mitigate oxidation and which *enhance* oxidation are presented for researchers who would like to either take advantage of the ozonolysis of sulfur-containing compounds or need to minimize the effect. Finally, a new mechanism by which thiols are oxidized during the corona discharge ESI process is proposed and discussed.

## 4.2 Materials and Methods

All analytes were purchased from Sigma-Aldrich (St Louis, MO, USA) and used without further purification. All analytes were stored at room temperature. All solvents (HPLC grade water and MS grade acetonitrile and methanol) were purchased from Fisher Scientific (Pittsburg, PA, USA). For the mass spectrometry auxiliary and sheath gases, nitrogen gas was acquired from the Purdue University Department of Chemistry's in-house distillation apparatus. Argon gas (> 99.5% pure) was purchased from Indiana Oxygen Company (Lafayette, IN, USA). Oxygen gas (99.993 % purity) was purchased from Praxair Welding Gas and Supply Store (Lafayette, IN, USA).

Three different analyte solutions were prepared. Ethanethiol was dissolved in two different solvents (acetonitrile and methanol) both at a concentration of 10 % by volume. A solution of cysteine (a solid) was prepared in HPLC grade water at a concentration of 5 mg/mL. Every solution was made fresh every day experiments were performed.

The mass spectrometer used for this study was a Thermo Scientific Orbitrap XL. This mass spectrometer is a hybrid linear quadrupole ion trap with a high-resolution Orbitrap detector. It was operated in two different modes for this study: high resolution mode with the Orbitrap as the mass analyzer and low resolution mode with the linear quadrupole ion trap as the mass analyzer. The high resolution was set at 100,000 and was sufficient for calculating the exact elemental composition of many of the ions detected. The ionization mode used was ESI, operated in both positive and negative mode. The ion capillary was kept at 250 °C and the sheath and auxiliary gas (30 and 15 arbitrary units, respectively) was nitrogen except where otherwise noted. The sample was introduced by the built-in syringe pump at a flow rate of 10  $\mu$ L/min except where noted otherwise. The voltage on the ESI source was tuned daily to optimize ionization and produce a stable current. Voltages varied between 2.5-4.5 kV.

For the APCI experiment, the nitrogen sheath and auxiliary gas was kept at 30 and 10 (arbitrary units), respectively. The voltage on the APCI source was at 3-5 kV and tuned daily for optimized ionization and current. The ion transfer capillary voltage was 30 V and the ion transfer capillary temperature was 300 °C.

Collision activated dissociation (CAD) experiments, were used to identify the fragments produced by different ions. This data was then used to identify common fragmentation losses and to aid in identifying the elemental composition of the ions. For CAD experiments, the initial ion isolation was performed with an isolation width of 2 m/z units and a q value of 0.25. Occasionally, the isolation window was narrowed to prevent the isolation of interfering ions of similar m/z value. The isolation width was never less than 0.8 m/z units. CAD energy was optimized on a case-by-case basis and was between 10 and 25 arbitrary units.

For in-source CAD (ISCAD) experiments, an increased voltage gradient was added at the source of the mass spectrometer to accelerate ions into the orifice of the mass spectrometer. The voltage used was 10 V. ISCAD was used to break up adducts prior to entering the mass spectrometer and therefore provided data on the most stable covalently bonded products.

To posit a potential mechanism for the reaction between ethanethiol and ozone, density functional theory (DFT) calculations were performed using the Gaussian 09 program.<sup>29</sup> All calculations were performed by graduate students Wanru Li and Jacob Milton. The DFT calculations were used for energy calculations and geometry optimization. The level of theory chosen was the M06-2X/aug-cc-pVTZ level of theory. This level of theory was chosen because it is known to be one of the best functionals for calculations of reaction barrier heights.<sup>30</sup> Following the DFT calculations, a full Hessian calculation and geometry optimization was performed. This was done to ensure that the transition state had only one negative eigenvalue and that all eigenvalues for minima were positive. For the transition state calculations, the geometry was confirmed by intrinsic reaction coordinate (IRC) calculations. These IRC calculations were used to further optimize the geometry of the resulting products. Partial charges were calculated using the CHELPG algorithm, which fits point charges to the electrostatic potential.<sup>31</sup> Calculated internal energies and enthalpies were thermally corrected using harmonic oscillator statistical mechanics assuming the reaction took place at 1 atm pressure.

## **4.3 Results and Discussion**

### **4.3.1 Reactions of Ethanethiol During Atypical ESI**

I first noted apparent oxygen-incorporation into sulfur-containing compounds when performing ESI/MS experiments with pure ethanethiol. The finding was surprising and unexpected, since the ethanethiol being tested was a pure liquid; the presence of so many additional ions in the mass spectra was concerning and required further study. High resolution mass spectrometry measurements and CAD experiments confirmed not only that oxygen was being added to ethanethiol, but that the energy required to break the resulting ion into fragments was on par with the energy needed to fragment a covalent compound. This meant that not only was oxygen being incorporated into the ethanethiol, but that the products were a result of chemical reactions that formed a covalent bond between the oxygen and the ethanethiol. In-source CAD (ISCAD) further confirmed that several of the unexpected peaks, including many of the oxygen addition peaks, were highly stable, suggesting they were the result of chemical reactions rather than mere adducts. It was at this point that the investigation into the cause of this chemical reaction and the resulting products was born.

I noted that the ESI/MS conditions which seemed to produce the oxygen incorporation and highest number of additional peaks were low analyte flow rates (approximately 10  $\mu\text{L}/\text{min}$ ) and relatively high ESI voltages (2.5-4.5 kV). The spectra collected under these conditions were not easily interpreted and included many peaks, with the pseudomolecular ion barely apparent and numerous reaction products appearing in both positive and negative mode ESI (See Figure 4.1 below).

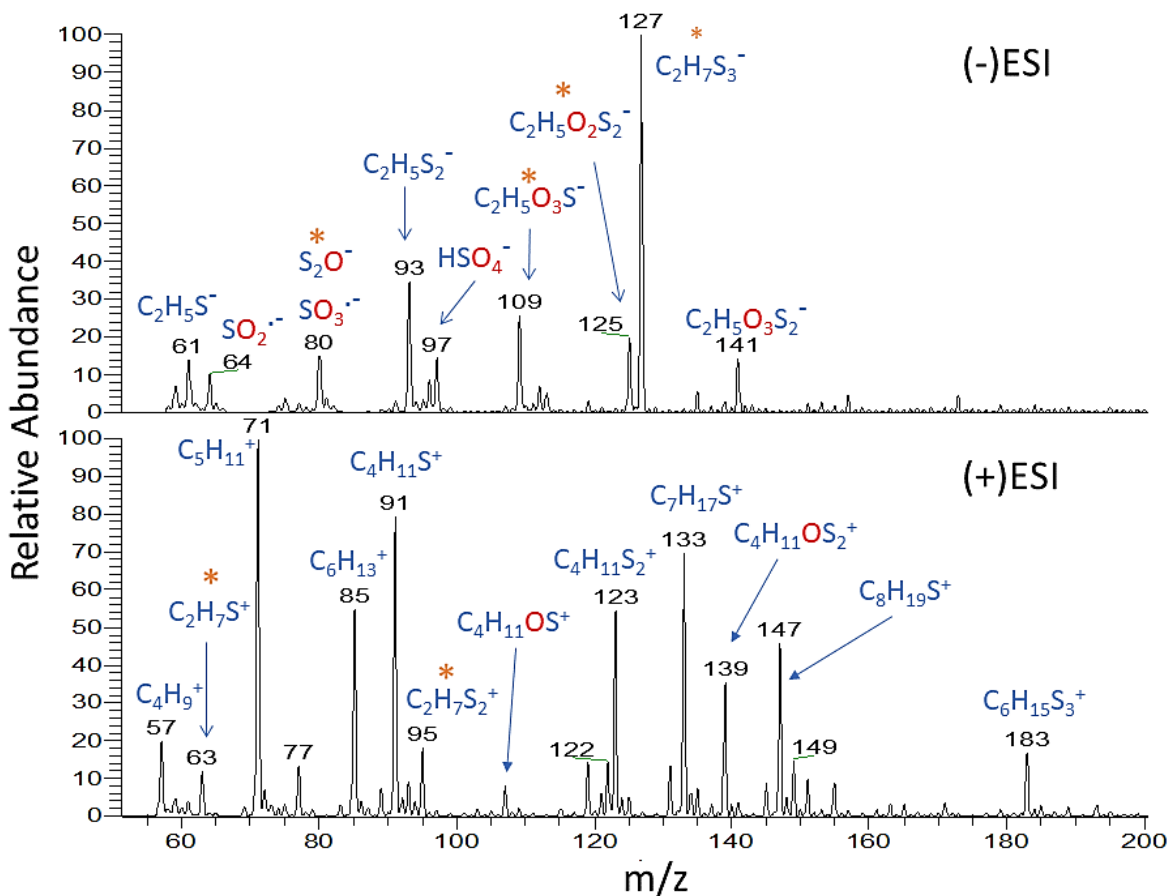


Figure 4.1 Negative mode ESI (top) and positive mode ESI (bottom) mass spectra of pure ethanethiol. The pseudomolecular peaks for deprotonated and protonated ethanethiol are  $m/z$  61 and 63, respectively. An analyte flow rate of 10  $\mu\text{L}/\text{min}$  and similarly high voltages were used for both experiments. The mass spectrum measured using positive mode shows significantly less oxygen incorporation but a larger number of peaks. \* Denotes a highly stable ion as determined by ISCAD experiments.

During the experiments with ethanethiol, a visible electrical discharge and plasma formation was observed at the tip of the ESI needle as the neat thiol was introduced (see Figure 4.2 below). A literature search provided an explanation of both the plasma formation and the greatly-increased

oxygen incorporation seen in the negative mode ESI spectra compared to the positive mode spectra. Based on the literature, the low analyte flow rate and the high voltage combined to create a corona discharge that, according to literature, contained highly-reactive ozone.<sup>17-19</sup> Additionally, the literature revealed that negatively charged plasma formed during negative mode ESI produces significantly more electrons than positively charged plasma.<sup>25</sup> The increased number electrons leads to excited nitrogen and oxygen molecules and is responsible for up to 90 % of ozone formation in ESI.<sup>25</sup> Therefore, the increased number of electrons found in the negatively charged ESI corona discharge plasma would result in an increased amount of ozone compared to positive mode ESI corona discharge plasma. Based on this literature information, it was hypothesized that the source of the oxygen incorporation in our experiments was ozone produced by the ESI conditions.



Figure 4.2 Photograph of the plasma discharge during an ethanethiol experiment with a negative mode ESI voltage of 3 kV and an ethanethiol flow rate of 10  $\mu\text{L}/\text{min}$ . The plasma discharge is located at the tip of the ESI needle and is in the middle of the red circle (added for emphasis).

To confirm that the sulfur oxidation was a function of the ESI corona discharge and not a result of a general corona discharge, the spectrum of ethanethiol was taken using atypical ESI as well as atmospheric pressure chemical ionization (APCI). APCI also involves a corona discharge, but the setup is very different from an ESI corona discharge. In APCI, the analyte solution is fully

vaporized and then the gas-phase molecules drift past a corona discharge needle on their way into the mass spectrometer (see Chapter 2 for additional details). It is at this point that ion-molecule reactions ionize the analyte. The analyte solution and the corona discharge are therefore separated in space. Additionally, the plasma formation at the APCI corona discharge needle is not extensive enough to form a visible plasma like the one we observed during the ESI experiments. ESI corona discharge, however, occurs at the very tip of the ESI needle. The analyte solution therefore flows through this corona discharge and plasma. There are, therefore, two competing trends that might affect the relative extent of ozone reactions. The corona discharge and ozone formation in ESI is likely greater than in APCI, leading to more ozone reactions. However, the ozone reactions in APCI take place in the gas phase while the ESI reactions likely take place, at least in part, in solution. Therefore, the APCI reactions that take place may take place more quickly compared to the ESI reactions.

The ESI and APCI spectra were collected using ethanethiol at an infusion rate of only 10  $\mu\text{L}/\text{min}$ , a flow rate we knew would induce the plasma formation during the ESI experiments. Negative mode was used for both experiments since negative mode is known to produce the more energetic corona discharge. All lens voltages and other tuning parameters for the mass spectrometer were held constant at normal operating conditions. Both spectra were collected on the same instrument within the same half hour. As anticipated, the reaction products and oxygen incorporation were both greatly increased in the ESI spectrum (see figure below). For the ESI spectrum, the oxygen-incorporation products ( $m/z$  141, 109) and other oxidation products ( $m/z$  97, 80, 64) are very abundant. The pseudomolecular ion of ethanethiol ( $m/z$  61) on the other hand, is less than 20 % relative abundance. The APCI spectrum, however, is much cleaner and shows very little evidence of oxygen incorporation or oxidation products. Indeed, the ethanethiol pseudomolecular ion is the base peak in the spectrum. As expected, it was concluded from the data that atypical ESI corona discharge experiments produced greater ozone reactions and oxidation products than APCI. Ultimately, APCI produced the more easily-interpreted spectrum. The ESI-induced provided additional information and reaction products, but ultimately interpretation of the resultant mass spectrum was greatly complicated, which could be a significant problem when analyzing complex mixtures with sulfur-containing analytes.

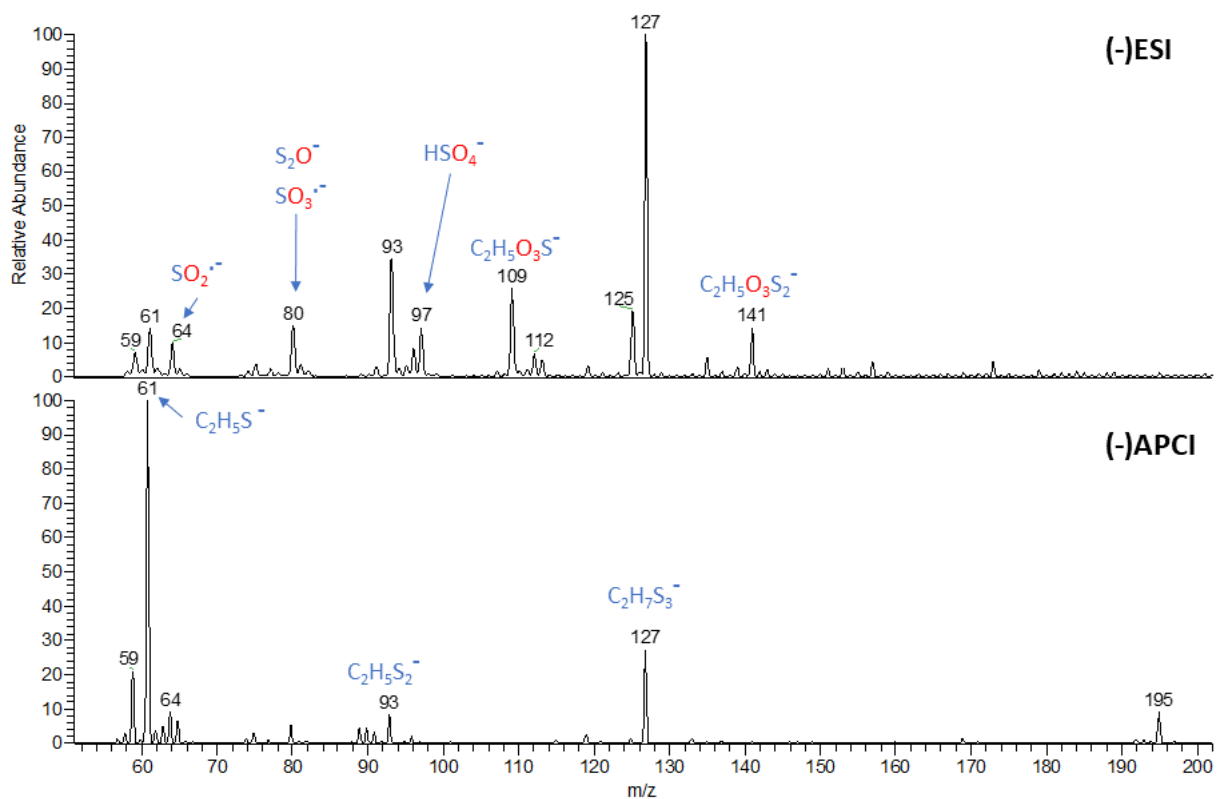


Figure 4.3 Comparison of negative ESI (top) and APCI (bottom) mass spectra of pure ethanethiol (deprotonated ethanethiol has  $m/z$  of 61). The low flow rate of  $10 \mu\text{L}/\text{min}$  and similarly high voltages were used for both experiments. The mass spectrum measured using APCI shows dramatically fewer ions, has a dominant deprotonated thiol ion ( $m/z$  61), and is therefore more easily interpreted.

### 4.3.2 Mechanism of Thiol Ion Ozonolysis

Based on experimental observations, an accepted mechanism for the reaction between a deprotonated thiol and ozone has been previously published.<sup>3,28</sup> A version of this scheme redrawn to include deprotonated ethanethiol as the reactant is shown in Figure 4.4 below. In the literature mechanism, the ESI source first produces a deprotonated thiol ion by the traditional ESI mechanism (see Chapter 2). The negative charge is located on the sulfur, which then performs a nucleophilic attack on one of the outer oxygens in ozone. The result is the direct addition of ozone to the sulfur, with the negative charge now located on the outer most oxygen. Next, a neutral oxygen molecule is lost, resulting in the overall addition of one oxygen to the deprotonated thiol. In this mechanism, to add additional oxygens, additional reactions with ozone are required (i.e. to

add three total oxygens, three consecutive reactions with ozone must take place). The rate-limiting step is believed to be the sulfoxide formation.

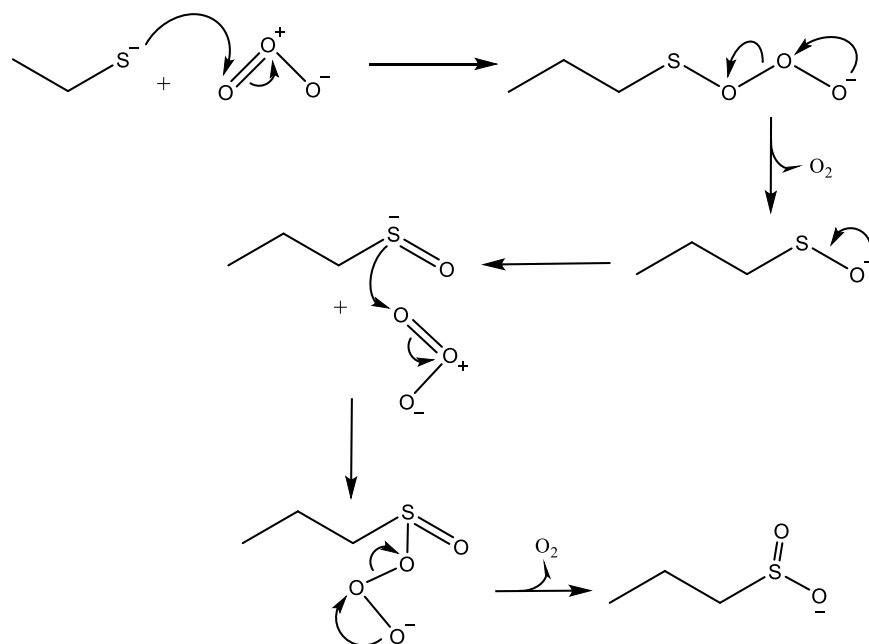


Figure 4.4 Previously proposed mechanism for the reaction between ozone and a negatively charged sulfur, based on Wang et al. and Williams et al.<sup>3,28</sup> In this proposed mechanism, the sulfur anion (formed during electrospray ionization) attacks one of the end oxygens on ozone. The sulfoxide formation is believed to be the rate-limiting step in the mechanism.

However, the literature mechanism did not explain our data. With each additional oxygen addition, a new reaction with ozone must take place. Statistically, this should ensure that the addition of one oxygen is more probable than the addition of two oxygens, which is still more probable than the addition of three oxygens. Surprisingly, in our negative mode ESI, the addition of one and two oxygens was not observed at all. The addition of three oxygens, however, was observed in our negative mode spectra (peak  $m/z$  109 in Figure 4.1). Considering this discrepancy between the literature-predicted outcome and our data, we decided to investigate other potential mechanisms for the reaction of deprotonated ethanethiol and ozone. Since quantum chemical calculations had not been cited as a source for the previous literature mechanism,<sup>3,28</sup> we performed quantum chemical calculations to establish the feasibility of the proposed mechanism.

The calculations we performed (completed by graduate students Wanru Li and Jacob Milton) did not support the literature mechanism. Instead, the calculations suggested that the most

energetically favorable mechanism involved direct insertion of the negatively charged sulfur into one of the oxygen-oxygen bonds within the ozone molecule (Figure 4.5). While the transition state for this reaction is positive by 7.8 kcal/mol, the energy within the plasma at the tip of the ESI needle, which has been shown to cleave carbon-carbon double bonds (a process requiring over 100 kcal/mol<sup>26</sup>), is more than sufficient for the reaction to overcome this barrier. The resulting ion ( $\text{C}_2\text{H}_5\text{SO}_3^-$ ) was observed in the mass spectrum of ethanethiol, and analogous ions were identified in the mass spectra of all other compounds studied (see following section). The reason why this ion is preserved and does not spontaneously fragment is the topic of current study by Wanru Li. This newly proposed mechanism for the addition of three oxygens in one step is more statistically likely than the previously proposed mechanism, which proposed that the addition of three oxygens was the result of three separate reactions with ozone.

Next, the fragmentation of the ozone addition product was investigated through additional quantum chemical calculations. The most energetically favorable fragmentation was the homolytic cleavage of the sulfur-carbon bond to produce an ethane radical and  $\text{SO}_3^-$ , a common ion found in all spectra in this study. It is therefore hypothesized that the presence of  $\text{SO}_2^-$  and  $\text{SO}_3^-$  in the mass spectra of different thiols is due to fragmentation of the  $\text{RSO}_2^-$  and  $\text{RSO}_3^-$  anions during their transfer to the ion trap. The mechanism is further supported by the  $\text{MS}^2$  mass spectra of each of the monothiols, which showed that the  $\text{RSO}_2^-$  and  $\text{RSO}_3^-$  product ions of all monothiols fragmented via the loss of an  $\text{R}^\bullet$  group, further suggesting homolytic cleavage of the C-S bond.

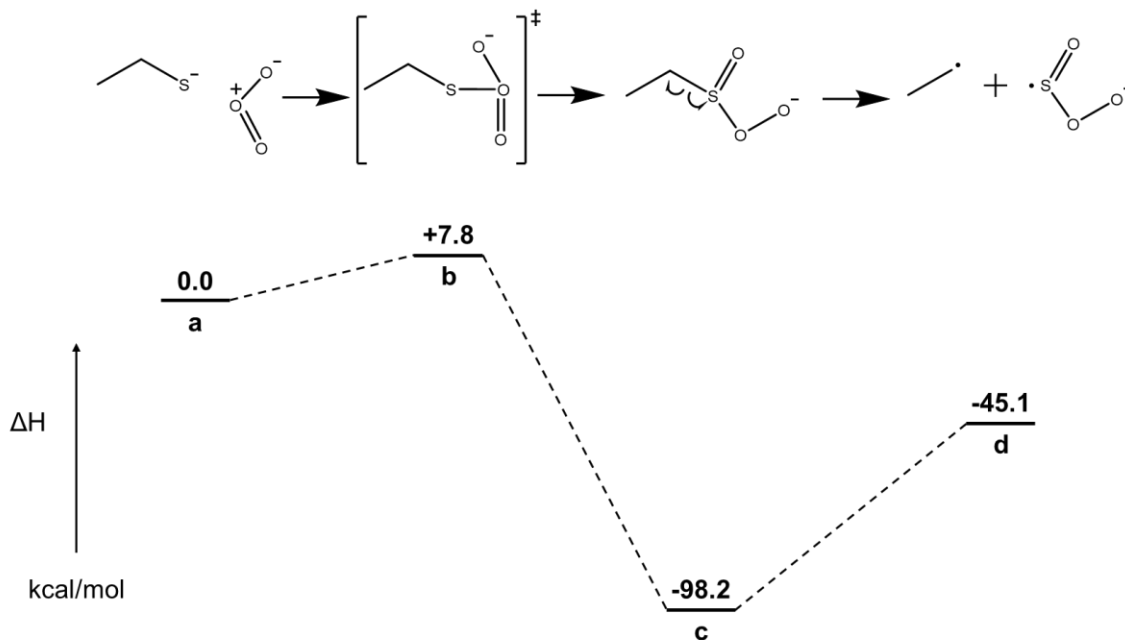


Figure 4.5: Potential energy surfaces (enthalpies in kcal/mol) for the formation of a) ethanethiol and ozone; b) transition state; c) product before CAD; d) final products after CAD. Calculations were performed at the M06-2X/aug-cc-pVTZ// M06-2X/aug-cc-pVTZ level of theory.

### 4.3.3 Trends in Sulfur-Compound Oxidation

Most experiments in this study used pure ethanethiol as the analyte since it is arguably one of the simplest sulfur-containing compounds. However, it was necessary that we confirm that ethanethiol was not the only sulfur-containing compound to be oxidized during ESI corona discharge experiments. Therefore, we chose four other compounds to test: propanethiol, ethanedithiol, tetrahydrothiophene, and the amino acid cysteine. Each compound was analyzed as a pure liquid except for cysteine, which is naturally a solid. The solvent chosen for cysteine was water and was chosen because of its solubility. The cysteine solution was prepared at 5 mg/mL. The (-) ESI mass spectra taken under corona discharge conditions for each compound are shown below.

The first interesting finding was that the relative abundance of the oxygen incorporation products were not consistent across multiple days. For example, Figure 4.6(a) below is a spectrum of ethanethiol. When compared to the spectrum in Figure 4.1, the oxygen-containing products  $m/z$  80, 109, and 125 have significantly different relative abundances. This finding suggested to us that the amount of ozone generated on different days is not consistent and therefore the extent of the

ozone reactions changes accordingly. However, the reaction products and spectral peaks themselves do not change between days. That is, the same reactions occur every time and the same products are produced; only the relative amount of each product changes.

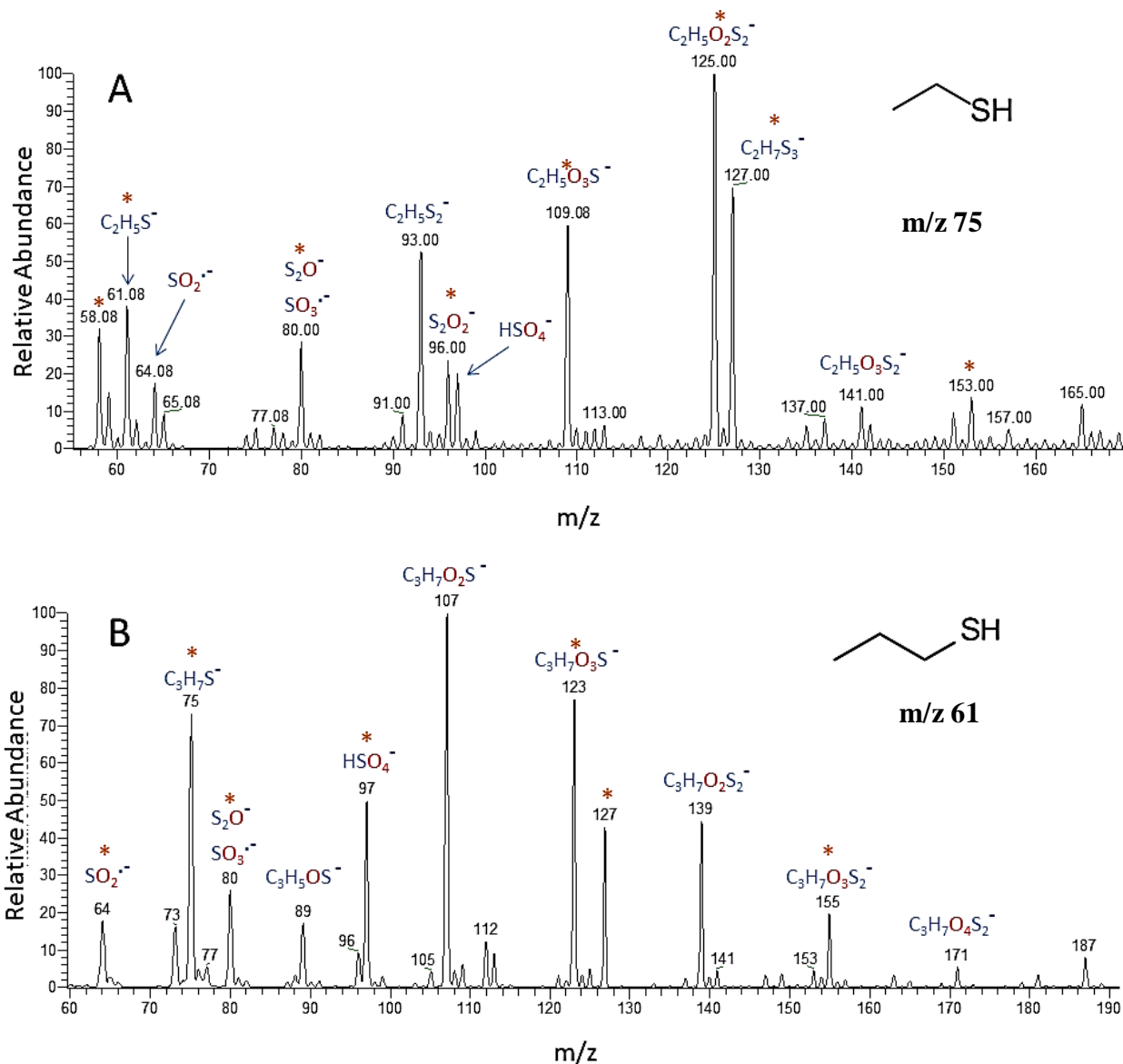


Figure 4.6 Low resolution (-)ESI MS spectra measured for neat (A) ethanethiol, (B) propanethiol, (C) ethanedithiol, (D) tetrahydrothiophene, and (E) cysteine in water. The chemical formulas of the major ions are shown; they were determined by high-resolution measurements (resolution 100,000). The m/z below each analyte structure is the m/z of the corresponding pseudomolecular ion. \* Indicates that the ion survived In-Source Collision Activated Dissociation (ISCAD) (data not shown), suggesting that this ion is very stable.

Figure 4.6 continued

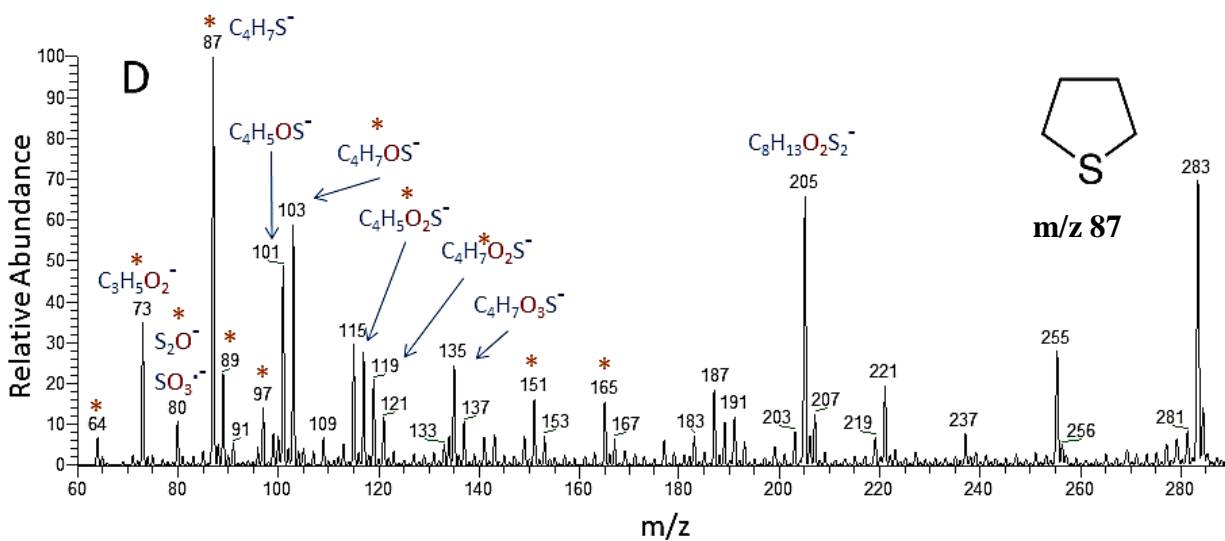
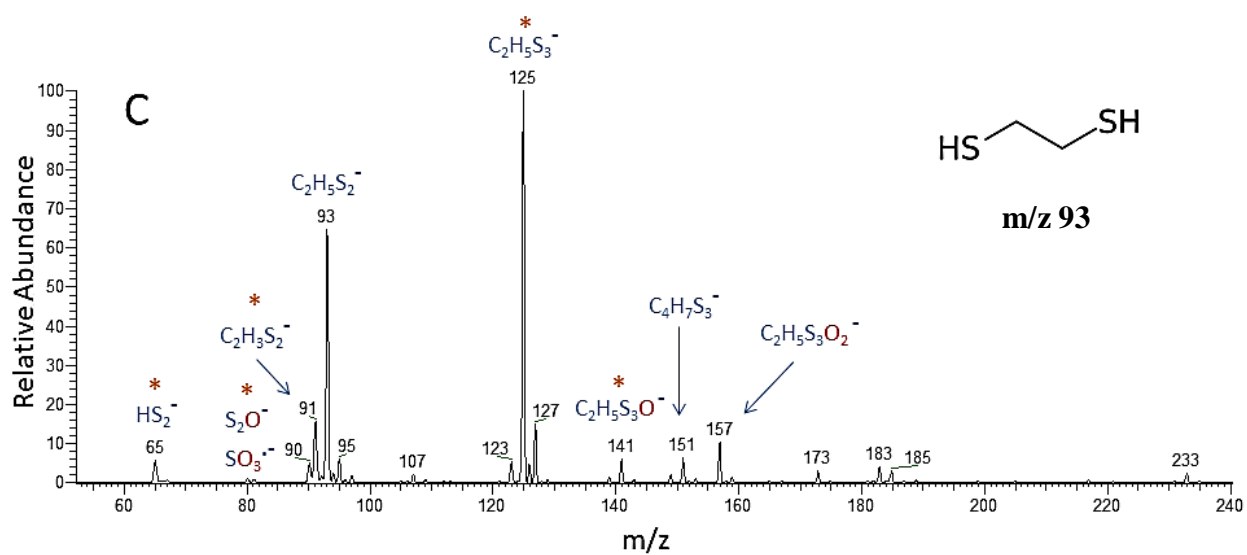
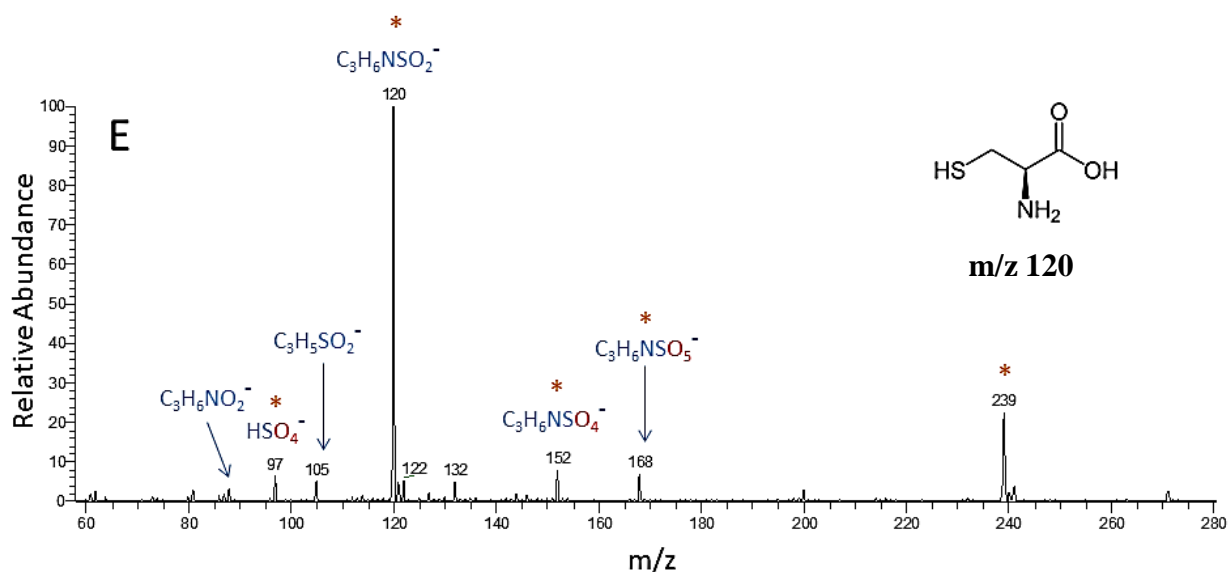


Figure 4.6 continued



Three types of reaction product ions were seen in the mass spectra of the five model compounds. The first type of ion included the addition of O, O<sub>2</sub>, or O<sub>3</sub> to the analyte. These product ions were seen to some extent for every analyte tested except ethanedithiol. The addition of O<sub>3</sub> was the most common, which makes sense considering our newly-proposed mechanism. According to this mechanism, ozone is directly added to the sulfur anion, and the product can then further fragment. The overall addition of just one or two oxygens is therefore likely a result of fragmentation of the ozone addition product. Both thiols showed significant O<sub>3</sub> and O<sub>2</sub> addition. The cyclic tetrahydrothiophene showed substantial O, O<sub>2</sub>, and O<sub>3</sub> addition. As previously reported for similar ozonolysis studies, cysteine exhibited both O<sub>3</sub> and O<sub>2</sub> addition, although the experiments did not produce the cysteine sulfonate reported previously.<sup>27</sup> In every case except cysteine, the oxygen addition products had a relative abundance of at least 20%, suggesting that reactions within the ESI plasma are abundant. The high frequency that these sulfur compounds reacted within the ESI source to form oxidation products suggests that sulfur-containing compounds in complex mixtures may be falsely identified as oxidized sulfur compounds when analyzed under these conditions.

The second type of commonly observed product ions resulted from the overall addition of S, SO, SO<sub>2</sub>, and/or SO<sub>3</sub>. Ionized cysteine was the only analyte tested that did not produce at least one of these products. Ethanethiol exhibited all four types of addition, while propanethiol only

exhibited SO<sub>2</sub> and SO<sub>3</sub> adduct formation. Ethanedithiol underwent SO and SO<sub>2</sub> adduct formation and tetrahydrothiophene formed an SO<sub>2</sub> adduct. The addition of SO<sub>x</sub> compounds likely arises from secondary reactions. Fragments of ethanethiol and ethanethiol oxidation products could further recombine with ionized or neutral ethanethiol within the ESI source, producing the SO<sub>x</sub> addition products.

The final types of commonly observed ions were the highly oxidized sulfur compounds SO<sub>2</sub><sup>-</sup>, SO<sub>3</sub><sup>-</sup>, and HSO<sub>4</sub><sup>-</sup>. At least one these highly oxidized species was observed for each compound tested. Ethanethiol and propanethiol had all three species; ethanedithiol and tetrahydrothiophene had SO<sub>3</sub><sup>-</sup>; cysteine only had HSO<sub>4</sub><sup>-</sup>. Two general trends in these ions were observed: first, large amounts of any of these three ions were correlated with higher degrees of O, O<sub>2</sub>, and/or O<sub>3</sub> adduct formation. For example, for propanethiol, the relative abundance of SO<sub>2</sub><sup>-</sup>, SO<sub>3</sub><sup>-</sup>, and HSO<sub>4</sub><sup>-</sup> in the mass spectrum were 20, 30, and 50 %, respectively while the O<sub>2</sub> and O<sub>3</sub> adducts were the two most abundant ions in the mass spectrum. Cysteine, meanwhile, had only 10 % relative abundance of HSO<sub>4</sub><sup>-</sup> and the relative abundances of O<sub>2</sub> and O<sub>3</sub> adducts were each only 10 %. Working on the assumption that SO<sub>2</sub><sup>-</sup> and SO<sub>3</sub><sup>-</sup> are fragmentation products of ozone addition, this correlation between SO<sub>2</sub><sup>-</sup>, SO<sub>3</sub><sup>-</sup> and O, O<sub>2</sub>, and/or O<sub>3</sub> product formation is easily explained. The presence of sulfonic acid may be the result of secondary reactions between fragment ions and other species found within the plasma: namely hydroxy radicals and hydrogen peroxide. The second observation was that SO<sub>2</sub><sup>-</sup> and SO<sub>3</sub><sup>-</sup> correlated with the amount of SO<sub>x</sub> product ions in the mass spectra. All compounds except cysteine formed at least one of these radical anions, and *also* showed extensive addition of S, SO, SO<sub>2</sub>, and/or SO<sub>3</sub>. Cysteine, meanwhile, showed nearly no radical anion formation or SO<sub>x</sub> adduct formation.

Ethanedithiol had significantly fewer reaction products compared to the other sulfur-containing analytes. No significant incorporation of ozone was noted, and the fragments associated with ozone reactions (namely SO<sub>3</sub><sup>-</sup>) were also nearly nonexistent. Instead, numerous additions of sulfur were observed, leading to ions such as C<sub>2</sub>H<sub>5</sub>S<sub>3</sub><sup>-</sup>. The source of the incorporated sulfur is not known, but this behavior was observed for other species as well, suggesting that sulfur-carbon bond breakage occurs within the plasma. Ultimately, we do not yet know why dithiols react with ozone so differently. One possibility is that the deprotonated thiol reacts with the still protonated thiol, resulting in the formation of a disulfide bond that would be unlikely to oxidize through ozone addition. However, there is currently no support for this theory beyond the appearance of HS<sub>2</sub><sup>-</sup> ions

in this spectrum, which are not seen in any abundance for the analytes. This finding suggests that there is the formation of disulfide bonds for this analyte.

#### **4.3.4 Controlling the extent of oxidation**

Understanding the conditions that lead to the greatest amount of ESI ozonolysis may help researchers choose appropriate conditions when analyzing sulfur-containing compounds. Therefore, we performed several tests with pure ethanethiol to determine the parameters that influence the amount of ESI-induced oxygen addition.

##### ***Oxygen Gas***

Most OzESI/MS experiments artificially increase the ozone formation in the ESI source through the use of ozone generators or pure oxygen sheath and auxiliary gases. However, our experiments were conducted without the aid of an ozone generator and with nitrogen sheath and auxiliary gases. Therefore, we were uncertain if our OzESI/MS products would be altered if performed with pure oxygen gas. To see whether using oxygen gas created a fundamentally different mass spectrum, we switched the sheath and auxiliary gas from nitrogen to pure oxygen. Ethanethiol was used as the analyte and was introduced at a flow rate of 10  $\mu\text{L}/\text{min}$ . The voltage was kept constant at -4 kV. A collection of spectra with nitrogen gas were taken first as a control and then the same number of spectra were collected with oxygen gas. The averaged spectra can be seen below.

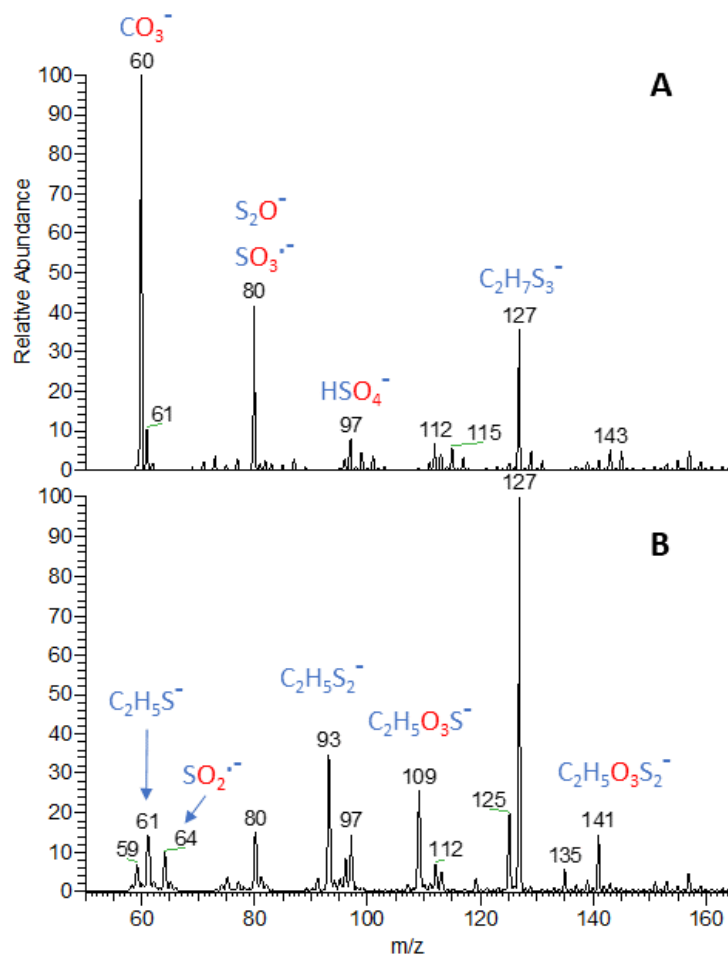


Figure 4.7 Low-resolution atypical condition (-)ESI mass spectrum of ethanethiol taken with (a) oxygen and (b) nitrogen as the sheath and auxiliary gas.

It is clear that drastic changes are observed between the oxygen and nitrogen spectra. In the nitrogen spectrum, the direct ozone addition product is easily observed ( $m/z$  109). The pseudomolecular ion of ethanethiol ( $m/z$  61) is also observed, as are numerous other products. However, the mass spectrum acquired with oxygen gas is dramatically different. The ozone addition product is nearly absent. Instead, the fragment ions associated with ozone addition ( $m/z$  80) are dramatically more abundant. This suggests that the ozone reaction still takes place, but that the plasma formed with pure oxygen is so energetic that the ozone product fragments before making it into the mass spectrometer for analysis. Additionally, the oxygen spectrum had an ion present that was not observed with nitrogen:  $\text{CO}_3^-$ . The carbon trioxide ion is known to occur within negative corona discharges.<sup>32</sup> Its occurrence during the oxygen experiments further suggests that the plasma formed during the oxygen corona discharge was more energetic.

To quantify the change in abundance, the total absolute signal intensity was determined for each averaged spectrum. The total absolute signal intensity is a direct measure of the total current produced during the collection time and is recorded by the mass spectrometer. In short, it is the summed signal intensities of every ion that hits the detector within the collection window. Next, the absolute signal intensity (measured current) for each individual ion was divided by the total absolute signal intensity. This was performed to normalize the signals, since changing from nitrogen to oxygen gas lowered the overall ionization efficiency and the resulting intensity of the mass spectrum. By normalizing to the overall signal, the intensities of individual ions in the nitrogen and oxygen experiments could be compared. The comparison confirmed that the relative abundance of oxygen-containing ions doubled when oxygen gas was used (see Figure 4.8).

These findings led us to the conclusion that, while oxygen gas is not necessary to form ozonolysis products during ESI experiments, oxygen gas greatly increases the abundance of the oxygen-containing products. However, using nitrogen as the sheath and auxiliary gases produces conditions that are more conducive to preserving and observing the ozone reaction products. OzESI/MS can therefore be performed with sulfur-containing analytes without the use of ozone generators or oxygen gas.

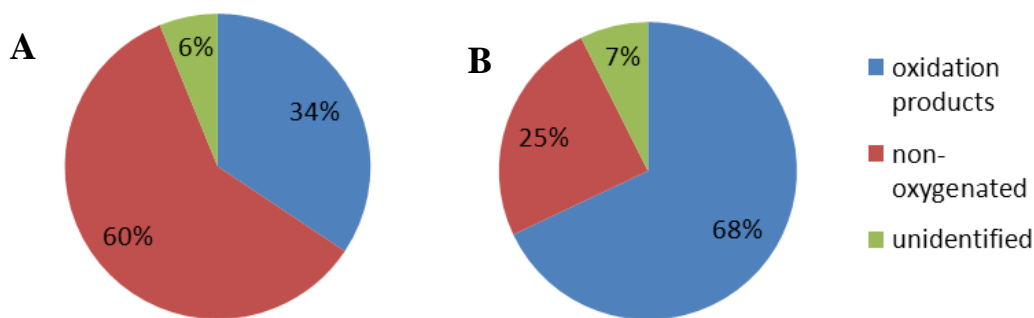


Figure 4.8 Relative abundances of oxygen-containing ions when analyzed by ESI using (a) nitrogen and (b) oxygen gas. Ethanethiol was the analyte. Comparisons were made by normalizing each ion signal to the total absolute signal intensity. The relative abundance of oxygen-containing ions doubled when oxygen was used instead of nitrogen.

### ***Analyte Flow Rate***

It is known that ESI corona discharge is mostly prevalent at low analyte solution flow rates.<sup>17-</sup>

<sup>19</sup> To test the effect of analyte solution flow rate on the oxygen inclusion in our data, spectra of

ethanethiol at eight different flow rates were acquired. The ethanethiol injection rate was increased from 10  $\mu\text{L}/\text{min}$  up to 80  $\mu\text{L}/\text{min}$ , with the flow rate increasing 10  $\mu\text{L}/\text{min}$  every 30 seconds. The total abundances of oxygen-containing and non-oxygen containing ions were determined for each flow rate and normalized to the total absolute ion abundance for that flow rate as described in Section 4.3.3.1. The results are shown in the graph below. It is clear that there is a direct correlation between the flow rate and the abundance of oxygen-containing ions: as the flow rate increases, the oxygen-containing ions decrease. It has not been established whether this trend extends past 80  $\mu\text{L}/\text{min}$  flow rates; higher flow rates could not be tested due to the foul smell of ethanethiol. Beyond 80  $\mu\text{L}/\text{min}$ , the smell could not be contained by our exhaust apparatus. The oxidation and ozone reactions were most abundant at the lowest flow rates, which agrees well with previous OzESI/MS experiments.<sup>17,26</sup> Additionally, the pseudomolecular ion of ethanethiol increased with increasing injection volume, leading to more easily-interpreted mass spectra. There are two main reasons why the oxidation likely decreases as the analyte injection rate increased. Firstly, as the analyte injection rate increased, the frequency with which visible plasma was formed decreased. Therefore, the plasma generation at higher flow rates is most likely lower, since the charge is being carried by a larger volume of liquid. Additionally, higher flow rates result in an increased linear velocity for the analyte molecules. This means that at higher flow rates, the ethanethiol molecules and ions spend less time in the corona discharge, which might inhibit the frequency of ion/molecule reactions within the corona discharge.

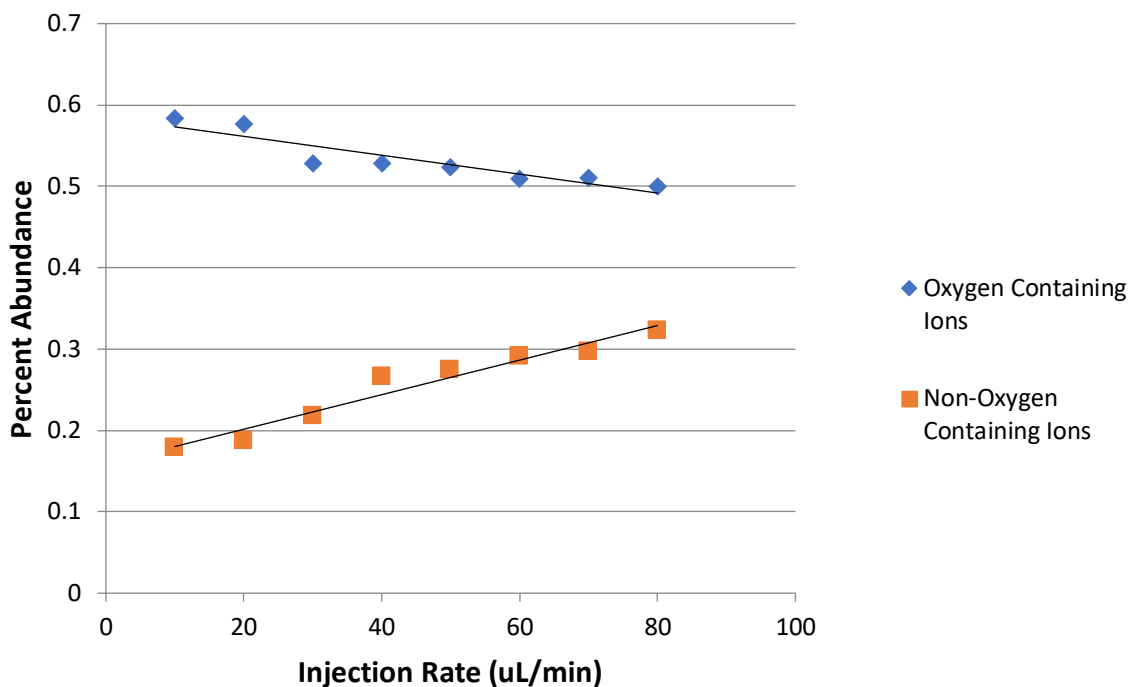


Figure 4.9 Relative abundances of oxygen containing and non-oxygen containing ions as a function of the syringe injection flow rate of pure ethanethiol in (-) ESI.

### ***Removing Oxygen from the ESI Source***

Since OzESI/MS requires the formation of ozone from atmospheric oxygen, it was hypothesized that increasing the nitrogen gas during the ESI experiments could displace the majority of atmospheric oxygen in the ESI source and therefore decrease the ozone production and resulting oxidation products. To test this hypothesis, five different spectra of ethanethiol in (-) ESI mode were taken. Ethanethiol was injected at a constant flow rate of 10 µL/min. The sheath/auxiliary gas flow rates were increased for each spectrum at total flow rates of 20/10, 30/15, 40/20, 60/30, and 70/35 arbitrary units. The spectra for 20/10, 40/20, and 70/35 are shown in the figure below. Overall, the changes were not as dramatic as anticipated. As the nitrogen flow rates increased, the relative abundance of the  $\text{HSO}_4^-$  and  $\text{C}_2\text{H}_5\text{S}_2\text{O}_3^-$  ions decreased, while the relative abundance of  $\text{SO}_3^-$  increased. The relative amount of the direct ozone addition ( $m/z$  109) was fairly constant, suggesting that ozone addition still occurred, even when the ESI source was purposefully purged with nitrogen gas. The simultaneous decrease in  $\text{C}_2\text{H}_5\text{S}_2\text{O}_3^-$  and increase in  $\text{SO}_3^-$  might suggest that the high nitrogen flow rates led to increased fragmentation of some higher-order ozone products such as  $\text{C}_2\text{H}_5\text{S}_2\text{O}_3^-$  into the  $\text{SO}_3^-$  fragment ions. Ultimately, it was concluded

that flooding the ESI source with increasing amounts of nitrogen gas is unlikely to stop the formation of ozone and plasma discharge at low analyte flow rates.

Ultrapure argon gas was also tested as a sheath and auxiliary gas at different flow rates and similar results were obtained: the nitrogen and oxygen-containing ions were still present.

The only other source of oxygen that could potentially be removed is within the ethanethiol itself. If the ozone reactions are occurring primarily in the ESI droplets, dissolved oxygen and water within the analyte may be of significant importance for this reaction. However, the ethanethiol purchased was tested at 99.5 % purity on the certificate of analysis, and our lab was not equipped to further remove additional water from the test material.

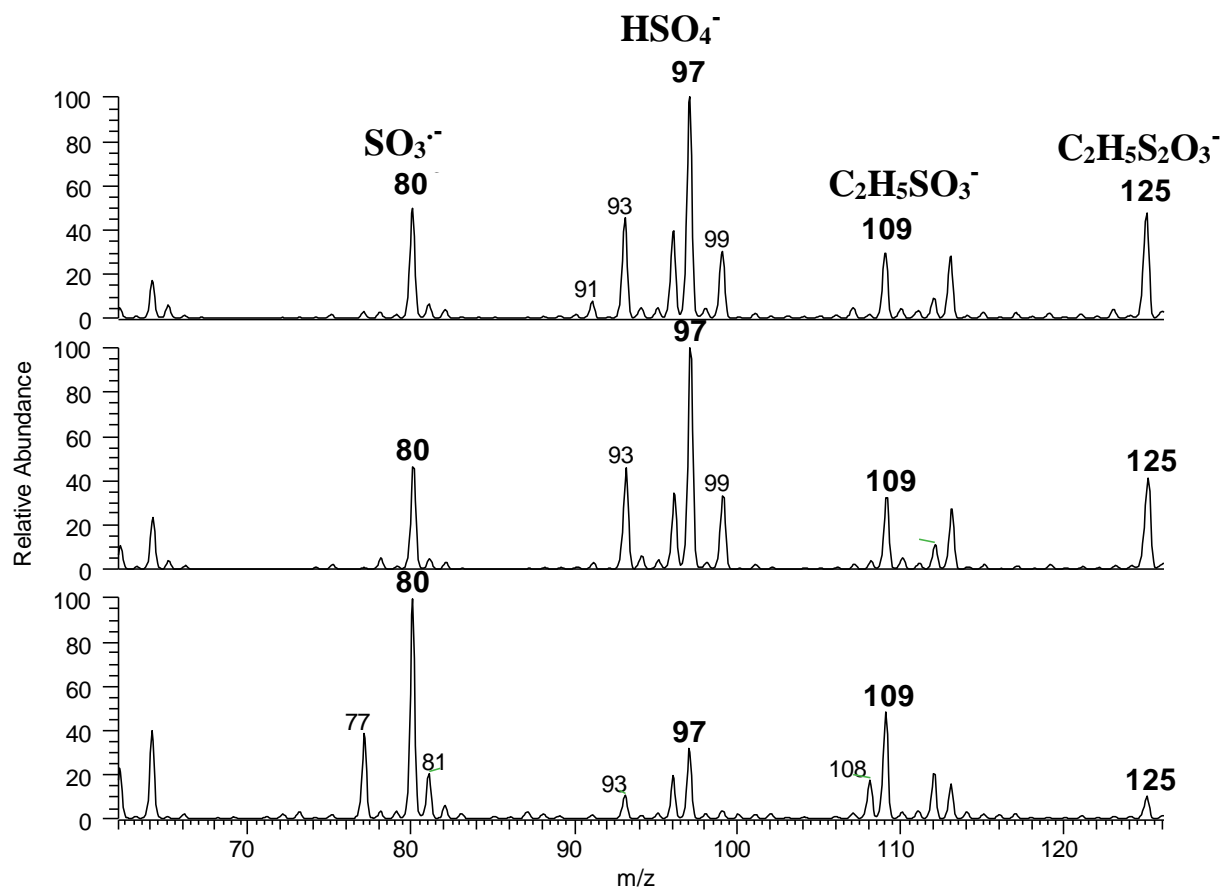


Figure 4.10 (-)ESI mass spectra of pure ethanethiol at sheath/auxiliary flow rates of (top) 20/ 10, (middle) 40/20, and (bottom) 70/35. The four most common oxygen-containing ions are labeled. The voltage was kept constant at 3 kV for each experiment. Deprotonated ethanethiol was not observed.

## Addition of Solvent

We hypothesized that adding a solvent to ethanethiol may reduce the amount of oxygen-incorporation seen in the pure ethanethiol mass spectra. We thought that the solvent may act in a sacrificial capacity. As the main constituent of the solution, the solvent would be more statistically likely to react with any ozone produced, decreasing the amount of oxygen incorporation for the ethanethiol. To test this hypothesis, two separate solvents were chosen: a protic solvent and an aprotic solvent. Based on ethanethiol's solubility, the protic solvent we chose was methanol and the aprotic solvent was acetonitrile. Each solution contained ethanethiol in the solvent at 10 % by volume. Background (-) and (+) ESI mass spectra of the pure solvents (methanol or acetonitrile) were taken for comparison.

(-)ESI N<sub>2</sub>

Analyte: Ethanethiol

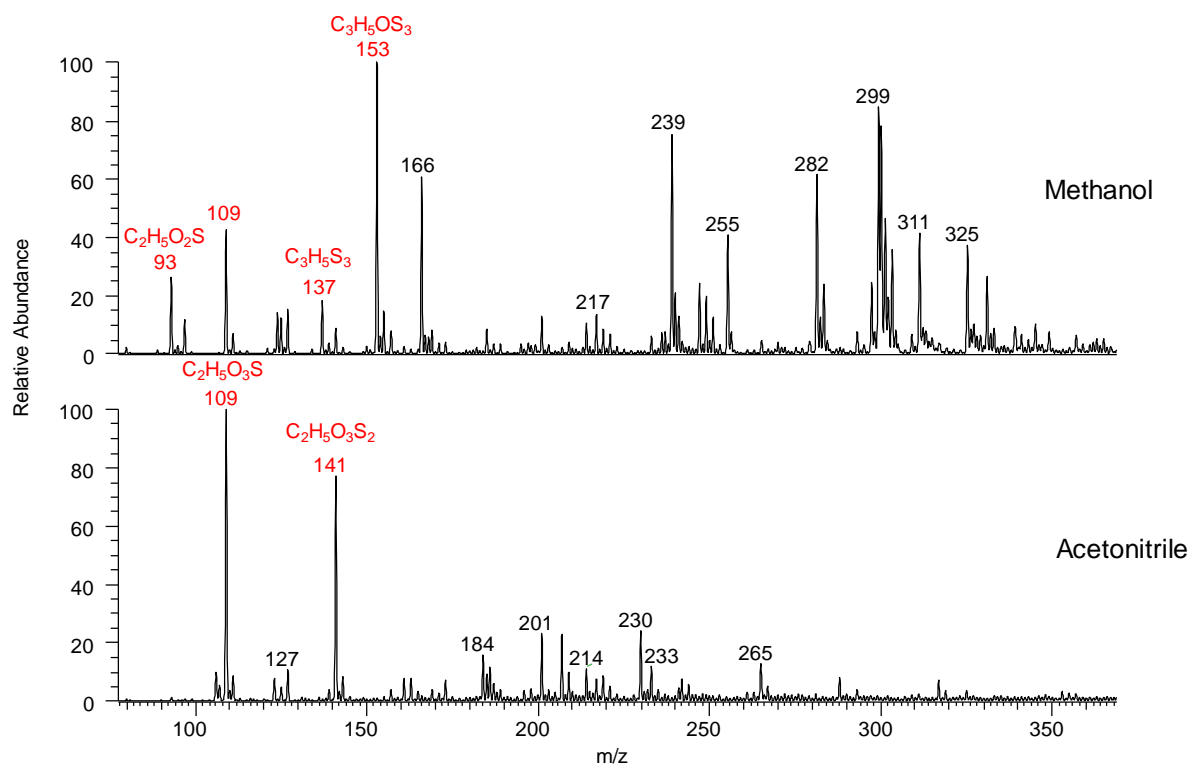


Figure 4.11 Low-resolution atypical condition (-)ESI mass spectrum of ethanethiol dissolved in methanol (top) and acetonitrile (bottom). Elemental compositions in **red** were determined using accurate mass measurements (high-resolution mass spectra; data not shown). The lack of an elemental composition (all ions in **black**) indicates that for this ion, high resolution data did not identify the elemental composition. Deprotonated ethanethiol (m/z 61) was not observed.

Ultimately, adding a solvent to the ethanethiol did not result in a more easily interpreted spectrum. The ozone addition product ( $m/z$  109) is apparent in the (-) ESI spectra of both the methanol and acetonitrile solutions. Other oxygen containing ions were also observed. Therefore, the reaction products did not disappear or even decrease with the addition of either methanol or acetonitrile. Additionally, the pseudomolecular ion for ethanethiol ( $m/z$  61) was not observed for either mixture. These observations, when combined with the extensive number of additional peaks, suggests that mixing ethanethiol with methanol or acetonitrile is not a successful strategy for producing easily-interpreted data. The (+) ESI spectra of both solutions were also taken and were similarly difficult to interpret.

The positive-mode spectra for the mixtures of ethanethiol were also difficult to interpret. We had hoped that, since positive-mode ESI corona discharge plasmas are less energetic, that the addition of solvent would be more helpful in positive mode, preserving the pseudomolecular ion and reducing spectral complexity. As seen in the figure below, this was not the case for either solvent mixture, suggesting that the plasma reactions, even in lower-energy positive mode plasma, are inherent and pervasive.

(+)ESI N<sub>2</sub>  
Analyte: Ethanethiol

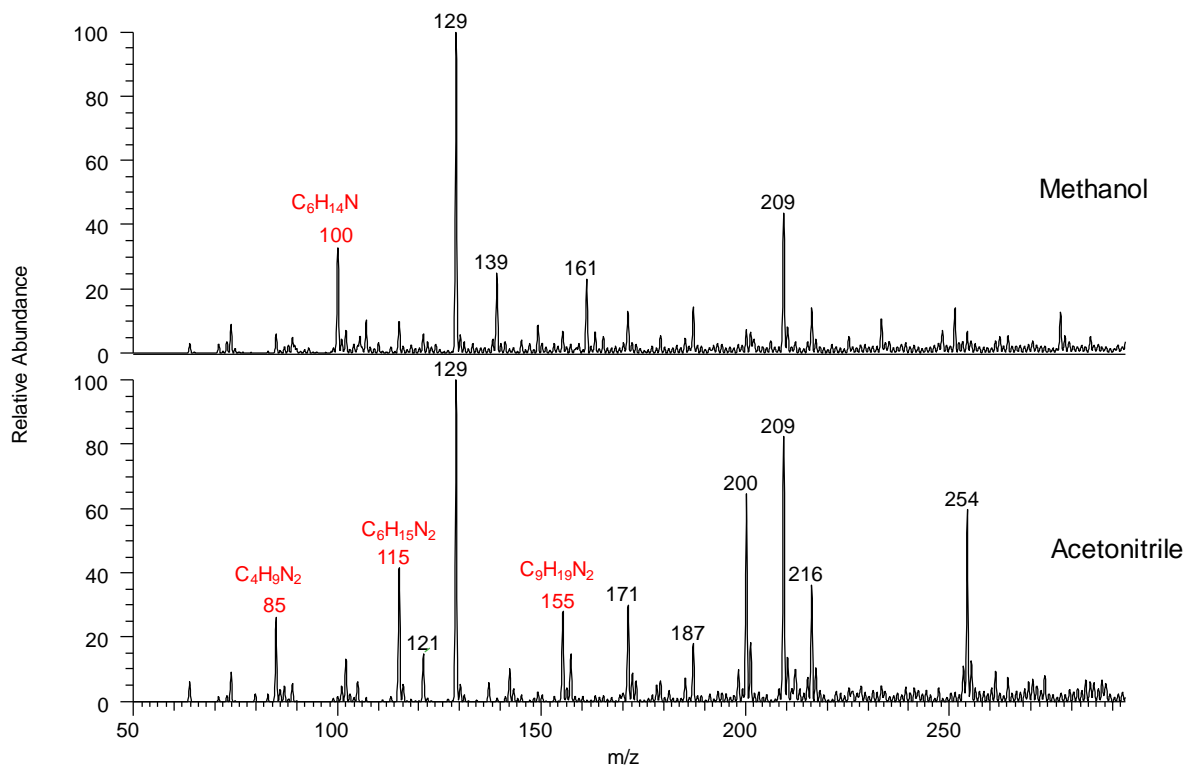


Figure 4.12 Low-resolution atypical condition (+)ESI mass spectrum of ethanethiol dissolved in methanol (top) and acetonitrile (bottom). Elemental compositions in **red** were determined using accurate mass measurements (high-resolution mass spectra; data not shown). The lack of an elemental composition (all ions in **black**) indicates that for this ion, either several reasonable predictions were obtained or none. Protonated ethanethiol was not observed.

#### 4.4 Conclusions

In this study, electrospray ionization experiments performed at atypical conditions—high voltages and low flow rates—produced a corona discharge plasma capable of reacting with a range of sulfur-containing analytes, including ethanethiol, propanethiol, ethanedithiol, tetrahydrothiophene, and cysteine. The result was a variety of oxygen-containing ions. Ozone produced in the corona discharge plasma was identified as the most likely cause of the oxygen incorporation products. The literature mechanism for the reaction between deprotonated thiol ions and ozone was deemed potentially incomplete. Subsequent quantum chemical calculations were performed to investigate the mechanism of formation for the oxygen-containing ions. Based on the calculations, a new mechanism was proposed. In this mechanism, the charged sulfur directly

inserts into one of the ozone's oxygen-oxygen bonds. The ozone addition product can then fragment by homolytic cleavage to produce  $\text{SO}_3^{\cdot-}$  fragment ions. This fragmentation pattern was confirmed using CAD experiments and other experimental data.

All sulfur-containing compounds tested exhibited substantial oxidation. The most common oxidation reactions included the addition of O,  $\text{O}_2$ ,  $\text{O}_3$ , S, SO,  $\text{SO}_2$ , or  $\text{SO}_3$ . Additionally, the identification of  $\text{SO}_2^{\cdot-}$ ,  $\text{SO}_3^{\cdot-}$ , and  $\text{HSO}_4^-$  in the mass spectra was closely associated with the extent of oxidation.

The conditions which lead to the most extensive reaction product formation and oxygen incorporation were tested. Ultimately, the use of low analyte flow rates ( $< 50 \mu\text{L}/\text{min}$ ) produced the largest amount of ozone reaction products. Changing the ESI gas to oxygen increased total oxygen-containing ion abundance, but tended to decrease the abundance of the direct ozone addition products. Oxygen incorporation mitigation strategies such as solvent addition and flooding the ESI source with nitrogen gas were unsuccessful. Indeed, the addition of solvent dramatically increased the complexity of the resulting spectra. Therefore, mixing thiols with methanol or acetonitrile is not suggested when low flow rates and high ESI voltages are required. While lowering the voltage used for ionization would likely result in lower oxygen incorporation, the lower voltage did not produce a stable current or analyte ionization to allow comparison. Ultimately, the only strategies successful at reducing the oxygen incorporation were the use of higher analyte flow rates and switching from ESI to APCI.

## 4.5 References

1. Block, E. Organic sulfur compounds in organic synthesis. *J. Chem. Ed.* **1971**, *48*, 814-824.
2. Nguyen, T.B. Recent advances in organic reactions involving elemental sulfur. *Adv. Synth. Catal.* **2017**, *359*, 1066-1130.
3. Gruhlke, M.C.H.; Slusarenko, A.J. The biology of reactive sulfur species (RSS). *Plant Physiol. and Biochem.* **2012**, *59*, 98-107.
4. Boyd, E.S.; Druschel, G.K. Involvement of intermediate sulfur species in biological reduction of elemental sulfur under acidic, hydrothermal conditions. *Appl. Environ. Microbiol.* **2013**, *79*, 2061-2068.
5. Wang, X.; Schrader, W. Selective analysis of sulfur-containing species in a heavy crude oil by deuterium labeling reactions and ultrahigh resolution mass spectrometry. *Int. J. Mol. Sci.* **2015**, *16*, 30133-30143.

6. Panda, S.K.; Andersson, J.T. Schrader, W. Characterization of supercomplex crude oil mixtures: What is really in there? *Angew. Chem. Int. Ed.* **2009**, *48*, 1788–1791.
7. Lobodin, V.V.; Juyal, P.; McKenna, A.M.; Rodgers, R.P.; Marshall, A.G. Silver cationization for rapid speciation of sulfur-containing species in crude oils by positive electrospray ionization Fourier transform ion cyclotron resonance mass spectrometry. *Energy Fuels* **2014**, *28*, 447-452.
8. Purcell, J.M.; Juyal, P.; Kim, D.G.; Rodgers, R.P.; Hendrickson, C.L.; Marshall, A.G. Sulfur speciation in petroleum: atmospheric pressure photoionization or chemical derivatization and electrospray ionization Fourier transform ion cyclotron resonance mass spectrometry. *Energy Fuels* **2007**, *21*, 2869-2874.
9. Godat, E.; Madalinski, G.; Muller, L.; Heilier, J-F.; Labarre, J.; Junot, C. Mass spectrometry-based methods for the determination of sulfur and related metabolite concentrations in cell extracts. *Meth. Enzymol.* **2010**, *473*, 41-76.
10. Roussis, S.G.; Proulx, R. Molecular weight distributions of heavy aromatic petroleum fractions by Ag<sup>+</sup> electrospray ionization mass spectrometry. *Anal. Chem.* **2002**, *74*, 1408-1414.
11. Wilm, M. Principles of electrospray ionization. *Mol. Cell. Proteomics* **2011**, *10*. M111.009407-1 – M111.009407-8.
12. Konermann, L.; Ahadi, E.; Rodriguez, A.D.; Vahidi, S. Unraveling the mechanism of electrospray ionization. *Anal. Chem.* **2013**, *85*, 2-9.
13. Van Berkel, G.J.; Kertesz, V. Using the electrochemistry of the electrospray ion source. *Anal. Chem.* **2007**, *79*, 5510-5520.
14. Van Berkel, G.J.; Giles, G.E.; Bullock, J.S.; Gray, L.J. Computational simulation of redox reactions within a metal electrospray emitter. *Anal. Chem.* **1999**, *71*, 5288-5296.
15. Van Berkel, G.J.; Zhou, F. Electrospray as a controlled-current electrolytic cell: Electrochemical ionization of neutral analytes for detection by electrospray mass spectrometry. *Anal. Chem.* **1995**, *67*, 3958-3964.
16. Wijeratne, A.B.; Yang, S.H.; Armstrong, D.W.; Schug, K.A. Solvent molecules undergo homolytic cleavage and radical recombination processes during negative-mode electrospray ionization: Adduct formation with antimony(III)-tartrate dianion. *Anal. Chem.* **2010**, *82*, 5141-5146.
17. Thomas, M.C.; Mitchell, T.W.; Blanksby, S.J. Ozonolysis of phospholipid double bonds using electrospray ionization: A new tool for structure determination. *J. Am. Chem. Soc.* **2006**, *128*, 58-59.
18. Thomas, M.C.; Mitchell, T.W.; Harman, D.G.; Deeley, J.M.; Murphy, R.C.; Blanksby, S.J. Elucidation of double bond position in unsaturated lipids by ozone electrospray ionization mass spectrometry. *Anal. Chem.* **2007**, *79*, 5013-5022.

19. Thomas, M.C.; Mitchell, T.W.; Blanksby, S.J. Online ozonolysis methods for the determination of double bond position in unsaturated lipids. In *Lipidomics, Methods in Molecular Biology*, vol. 579, Armstrong, D. (ed.), 2009. Humana Press, a part of Springer Science+Business Media, LLC.
20. Lloyd, J.R.; Hess, S. A corona discharge initiated electrochemical electrospray ionization technique. *J. Am. Soc. Mass Spectrom.* **2009**, *20*, 1988-1996.
21. Carroll D.I.; Dzidic I.; Stillwell, R.N.; Haegle, K.D.; Horning, E.C. Atmospheric pressure ionization mass spectrometry: Corona discharge ion sources for use in liquid chromatograph-mass spectrometer-computer-analytical system. *Anal. Chem.* **1975**, *47*, 2369–2373.
22. Chang, J.S.; Lawless, P.A.; Yamamoto, T. Corona discharge processes. *IEEE Transactions on Plasma Science*, **1991**, *19*, 1152-1166.
23. Maleknia, S.D.; Downard, K.M. Advances in radical probe mass spectrometry for protein footprinting in chemical biology applications. *Chem. Soc. Rev.* **2014**, *43*, 3244–3258.
24. Van Berkel GJ. The Electrolytic Nature of Electrospray. In: Cole RB, Ed. *Electrospray Ionization Mass Spectrometry*. Wiley; New York: 1997. pp. 65–105.
25. Chen, J.; Davidson, J.H. Ozone production in the negative DC corona: the dependence of discharge polarity. *Plasma Chem. Plasma P.* **2003**, *23*, 501-518.
26. Harris, R. A., May, J. C., Stinson, C. A., Xia, Y., & McLean, J. A. Determining double bond position in lipids using online ozonolysis coupled to liquid chromatography and ion mobility-mass spectrometry. *Anal. Chem.* **2018**, *90*, 1915-1924.
27. Khairallah, G.N.; Maccarone, A.T.; Pham, H.T.; Benton, T.M.; Ly, T.; da Silva, G.; Blanksby, S.J.; O’Hair, R.A.J. Radical formation in the gas-phase ozonolysis of deprotonated cysteine. *Angew. Chem. Int. Ed.* **2015**, *54*, 12947-12951.
28. Williams, S.; Campos, M.F.; Midey, A.J.; Arnold, S.T.; Morris, R.A.; Viggiano, A.A. Negative ion chemistry of ozone in the gas phase. *J. Phys. Chem. A* **2002**, *106*, 997-1003.
29. Gaussian 09, Revision A.02, Frisch, M.J.; Trucks, G.W.; Schlegel, H.B.; Scuseria, G.E.; Robb, M.A.; Cheeseman, J.R.; Scalmani, G.; Barone, V.; Mennucci, B.; Petersson, G.A.; Nakatsuji, H.; Caricato, M.; Li, X.; Hratchian, H.P.; Izmaylov, A.F.; Bloino, J.; Zheng, G.; Sonnenberg, J.L.; Hada, M.; Ehara, M.; Toyota, K.; Fukuda, R.; Hasegawa, J.; Ishida, M.; Nakajima, T.; Honda, Y.; Kitao, O.; Nakai, H.; Vreven, T.; Montgomery, J.A.; Peralta, J.E.; Ogliaro, R.; Bearpark, M.; Heyd, J.J.; Brothers, E.; Kudin, K.N.; Staroverov, V.N.; Kobayashi, R.; Normand, J.; Raghavachari, K.; Rendell, A.; Burant, J.C.; Iyengar, S.S.; Tomasi, J.; Cossi, M.; Rega, N.; Millam, J.M.; Klene, M.; Knox, J.E.; Cross, J.B.; Bakken, V.; Adamo, C.; Jaramillo, J.; Gomperts, R.; Stratmann, R.E.; Yazyev, O.; Austin, A.J.; Cammi, R.; Pomelli, C.; Ochterski, J.W.; Martin, R.L.; Morokuma, K.; Zakrzewski, V.G.; Voth, G.A.; Salvador, P.; Dannenberg, J.J.; Dapprich, S.; Daniels, A.D.; Farkas, O.; Foresman, J.B.; Ortiz, J.V.; Cioslowski, J.; Fox, D.J. Gaussian, Inc., Wallingford CT, 2009.

30. Easton, M.W.; Nash, J.J.; Kenttämä, H.I. Dehydration pathways for glucose and cellobiose during fast pyrolysis. *J. Phys. Chem. A* **2018**, *122*, 8071–8085.
31. Breneman, C.M.; Wiberg, K.B. Determining atom-centered monopoles from molecular electrostatic potentials: The need for high sampling density in formamide conformational analysis. *J. Comput. Chem.* **1990**, *11*, 361–373.
32. Sabin, J. R; Kim, H. A theoretical study of the structure and properties of carbon trioxide. *Chemical Physics Letters*. **1971**, *11*, 593–597.

## **CHAPTER 5. ANALYTICAL CHARACTERIZATION OF SELENIUM AND TELLURIUM DISSOLVED IN AMINE-THIOL SOLVENT SYSTEMS**

### **5.1 Introduction**

Originally designed for producing the energy required for satellites and other extraterrestrial space applications, photovoltaic cells are now responsible for a significant portion of electricity generation across the globe. In 2015, the global energy production from photovoltaics was more than 220 gigawatts, the same energy output as 280 coal-powered electric plants.<sup>1</sup> As global warming and greenhouse gas emissions have become an increasing problem, photovoltaic cells have emerged as a potential, greener alternative to more traditional electricity generation.<sup>2</sup> As countries invest more heavily in alternative energies,<sup>3</sup> the expected global electrical contribution from photovoltaics, especially from solar cells, is expected to increase to 20 % by 2050.<sup>4</sup> Thin film photovoltaics made from metal chalcogenides (chalcogens being the group on the periodic table including oxygen, sulfur, selenium, and tellurium) have emerged as the newest generation of photovoltaic cell technology. These new photovoltaics have several advantages over first-generation photovoltaics, including higher efficiencies,<sup>5</sup> lower production costs (both in energy and materials)<sup>6</sup> and the flexibility of the thin film structure, which can be bent into many shapes for a wide variety of applications.<sup>6</sup>

Traditionally, metal chalcogenides have been made using processes like co-sputtering and co-evaporation. Unfortunately, these processing techniques are relatively energy intensive and require preparation of the material under high vacuum.<sup>7</sup> A newer, alternative preparation method is solution processing. So far, two general types of solution processing have been developed. The first type begins with synthesizing the metal chalcogenide in the form of nanoparticles and then suspending those particles in a solvent to produce a metal chalcogenide “ink” that can then be sprayed or otherwise deposited onto a surface. The second type of solution processing begins with a molecular precursor to the material, which is directly deposited on a surface and then thermally annealed to produce the desired material. These processing techniques are attractive alternatives to co-sputtering and co-evaporation because of their lower energy and material consumption, decreased cost, and less intensive processing conditions.<sup>8-10</sup>

However, metal chalcogenide solution processing, especially nanoparticle ink synthesis, has its own challenges to overcome before wide-spread implementation is feasible. Finding a solvent

or combination of solvents (referred to here as a solvent system) that can dissolve the necessary precursors has been a significant challenge. When the chalcogen is sulfur, a wide variety of organic solvents, including DMSO, various alcohols, and DMF have all been successful for thin film fabrication.<sup>11,12</sup> For selenium and tellurium, however, these solvents do not work. Selenium and tellurium, which are heavier, bigger, and have more metallic character than sulfur (tellurium is classified as a metalloid), are more difficult to dissolve. While some solvent systems have been found to dissolve selenium and tellurium, these solvent systems tend to introduce impurities in the final material or require explosive or deadly chemicals like hydrazine.<sup>13-16</sup> The search for alternative solvent systems for selenium and tellurium has led to the recent utilization of amine-thiol mixtures. These solvent systems are made from a mixture of an amine and a thiol, and they have been successful in dissolving a wide range of metal chalcogenide precursors, including pure metals, metal salts, and pure sulfur, selenium, and tellurium. Not only have the amine-thiol solvent systems successfully dissolved metal chalcogenide precursors, but they are capable of dissolving high concentrations of the precursors under ambient temperature and pressure.<sup>17-20</sup>

So far, a range of materials have been successfully produced using the amine-thiol solvent system, including CdTe, CuBaSnS<sub>4</sub>, SnTe, (Cu,Ag)(In,Ga)(S,Se)<sub>2</sub>, (Cu,Ag)<sub>2</sub>ZnSn(S,Se)<sub>4</sub>, Sb<sub>2</sub>Se<sub>3</sub>, and PbS/Se/Te for use in both photovoltaic cells and thermoelectric devices.<sup>17,20-27</sup> A mixture of oleylamine and dodecanethiol has successfully been used to prepare CdTe, Cu(In,Ga)Se<sub>2</sub>, and Cu<sub>2</sub>ZnSnSe<sub>4</sub> nanoparticles<sup>28</sup> while ethylenediamine-ethanethiol has been used to synthesize Sb<sub>2</sub>Se<sub>3</sub> and SnTe nanoparticles.<sup>20</sup> In the case of ethylenediamine-ethanethiol, the solvent system could be evaporated off from the thin film after spray coating, recovering pure, impurity-free Se and Te crystals.<sup>20</sup> Similarly, butylamine-ethanethiol has been used to produce sulfur impurity-free nanoparticles of CuInSe<sub>2</sub>, Cu<sub>2</sub>NzSnSe<sub>4</sub>, PbSe and pure Se.<sup>29</sup>

However, photovoltaic applications require very precise control over the structure and resulting conductivity of the material. For example, in Cu(In,Ga)Se<sub>2</sub> co-deposition, a starting Cu:Se ratio with more Cu produces an n-type conductivity<sup>30</sup> while more Se produces a p-type conductivity with superior performance results.<sup>31,32</sup> Tightly controlling parameters and understanding the chemistry of the deposition process is therefore very important for producing photovoltaics and other thin film devices with superior performance. Recent studies using amine-thiol solvent system ink formulation of CuCl<sub>2</sub>/CuCl and Cu precursors found that the number of different products formed in solution was significant and some precursors even led to impurities

in the final thin films.<sup>33,34</sup> Despite this need, the behavior of Se, and Te in amine-thiol solvent systems is not yet well understood. To date, few studies have actively looked at the chemistry behind the amine-thiol solvent system or how changes to that system or the precursors may alter the final material. Much of what we do know is anecdotal at best. For example, we know that Se dissolves in many amine-thiol systems that include monothiols in conjunction with either mono or diamines. However, Te only dissolves in mixtures of monothiols and diamines and remains insoluble if a monoamine is used. The reasons behind these differences are not understood and have not been extensively studied.

In this chapter, we analyzed selenium and tellurium when dissolved in butylamine-ethanethiol and in ethylenediamine-ethanethiol solvent systems. The solutions were studied using negative mode electrospray ionization tandem mass spectrometry and a variety of other analysis techniques, including proton NMR, Raman spectroscopy, and X-ray absorption spectroscopy. We found that the change from the monoamine butylamine to the diamine ethylenediamine resulted in significant changes in the species formed in solution. The reason why Te only dissolves in diamine-thiol solvent systems was also explored. The knowledge gained from these experiments led to the proof-of-concept co-dissolution of Se and Te in a monoamine-monothiol solvent system, which showed that soluble SeTe nanoparticle complexes can form in monoamine-monothiol solvent systems, introducing a new potential pathway for Se and Te solution processing. Additionally, the chemical role of the solvent itself was explored by varying the molar ratio of thiol:chalcogen, leading to a better understanding of the role the thiol plays in dissolving Se and Te. Finally, our improved understanding of this solvent system was used to control the chalcogen incorporation in a  $\text{PbSe}_n\text{Te}_{n-1}$  alloy nanoparticle synthesis.

## 5.2 Experimental

### 5.2.1 Materials

Ethanethiol (99 %) was purchased from Acros Organics. Se (100 mesh, 99.99 %), Te (30 mesh, 99.997 %), S (XX), lead acetate trihydrate (99.999 %), butylamine (99.5 %), and ethylenediamine (99.5 %) were purchased from Sigma-Aldrich. All chemicals were used as received. The following abbreviations will be used throughout this paper: Se (selenium), Te (tellurium), BA (butylamine), EN (ethylenediamine), ET (ethanethiol).

### 5.2.2 Ink Generation

A glovebox was used for the preparation of all materials and inks except where explicitly stated otherwise. The glovebox was held under inert nitrogen (moisture and oxygen concentrations were less than 1 ppm). All vials were kept sealed with parafilm to prevent evaporation of ethanethiol, which is somewhat volatile at room temperature. All sample preparation was performed by Swapnil Deshmukh, a doctoral candidate at Purdue University's Davidson School of Chemical Engineering.

The inks were prepared by adding the pure Se and/or Te to either butylamine (BA) or ethylenediamine (EN) and then adding the ethanethiol (ET). For most experiments, the ratio of amine: thiol was kept at 1:1 (by volume). Te solutions and Se solutions with lower ratios of ethanethiol had to be stirred for several hours to dissolve the Te or Se. All other solutions only required several minutes of stirring for dissolution. For mass spectrometry experiments, the following inks were generated and used for analysis: 10 mM Se in 1:1 (v/v) BA:ET; 10 mM Te in 1:1 (v/v) EN:ET; 0.2 M Te in 1:1 (v/v) EN:ET; 0.2 M Se:Te (mol ratio 7:3) in 1:1 (v/v) BA:ET; 0.2 M Se:Te (mol ratio 7:3) in 1:1 (v/v) EN:ET. Additionally, several inks using varying concentrations of thiol were prepared and are described further in the relevant following sections.

To generate the  $\text{PbSe}_n\text{Te}_{n-1}$  thin film, a solution of 0.2 M lead acetate trihydrate was first prepared in ethylenediamine. Next, two separate Se and Te solutions were made: one in 1:1 (by volume) butylamine: ethanethiol and the other in 1:1 (by volume) ethylenediamine: ethanethiol. The Se and Te mol ratio used was 7:3 and the total Se and Te combined concentration was kept at 0.2 M. Next, 1 mL of the lead acetate solution and 1 mL of the desired Se Te solution were mixed at room temperature for approximately 1 min. The nanoparticle formation could be visually distinguished within the stirring time. The precipitated nanoparticles were washed once with ethylenediamine and then three times with isopropyl alcohol. The isopropyl alcohol washes were performed outside of the glovebox. The washed nanoparticles were suspended in isopropyl alcohol, drop cast onto soda lime glass, and heated at 80 °C until dry to produce the thin films. All remaining materials, used inks, and nanoparticle washes were disposed of through Purdue University's Radiological and Environmental Management team.

### 5.2.3 Electrospray Ionization Mass Spectrometry Experiments

The experimental parameters chosen for these experiments were informed by previous studies on copper dissolution in similar amine-thiol solvent systems.<sup>33</sup> Since contact with air can alter the chemistry of the solution or, in the case of Te, cause the solution to spontaneously precipitate, the solutions were transferred into a homebuilt syringe setup inside a glovebox. The syringe setup contained three major components: a 5 mL Hamilton syringe for bulk sample storage and transfer, a 500  $\mu$ L Hamilton syringe for direct infusion into the mass spectrometer's electrospray ionization source, and a three-way Hamilton valve. All three components were connected using high purity perfluoroalkoxy tubing, which also connected the valve to the ESI source (see figure below). Using the three-way valve, the large syringe could be used to refill the small mass spectrometer injection syringe whenever needed. The gastight syringes insured that the solutions were not exposed to air prior to reaching the ESI source. The perfluoroalkoxy tubing was chosen due to previous experience<sup>33</sup> with the solvent system, which tended to dissolve traditional mass spectrometer tubing.

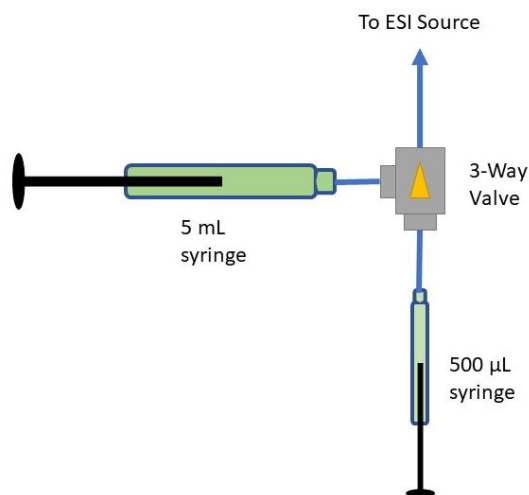


Figure 5.1 Schematic of the syringe setup used for the introduction of the solutions into the mass spectrometer. All tubing shown is perfluoroalkoxy tubing.

A Thermo Scientific LTQ Orbitrap XL hybrid mass spectrometer with integrated syringe pump was used to analyze all solutions. The resolution ( $m/\Delta m$ ) at  $m/z$  200 was set to 100,000 for all high-resolution experiments. All CAD experiments (see Chapter 2, section 2.4 for details on CAD) were performed at unit resolution in low resolution mode. Negative mode electrospray

ionization (ESI, see Chapter 2, section 2.2 for additional details) was used to ionize the species in solution. The ESI voltage used was between 3 and 4 kV and was adjusted on a day-to-day basis to ensure that the produced ion current remained stable. The ESI capillary was kept at 250 °C. Nitrogen was used as the sheath and auxiliary gases and was set to 30 and 15 arbitrary units, respectively. Samples were injected using the integrated syringe pump at a rate of 10  $\mu\text{L}/\text{min}$ . To ensure safety while working with the solutions and to prevent inhaling any fumes, an external three port exhaust system was designed and set up to remove any fumes from the mass spectrometry experiments. One port removed air around the ESI exhaust, a second port removed air from the area surrounding the syringes, and the third port directed the removed air and expelled it into a nearby fume hood. As an additional precaution, 3M series 6000 half-face respirators with multi-gas vapor cartridges (filter 60926) were worn while conducting all experiments.

To determine the elemental composition of each peak in the spectrum, high-resolution mass spectrometry measurements were first used. Using Thermo Scientific *Xcalibur 2.1* software, the recorded high resolution mass for a given peak was compared to the masses of theoretical projections of the possible elemental compositions for the given  $m/z$  ratio. Only matches with deviations less than 15 ppm from the theoretical mass were considered possible elemental compositions. The deviation limit was set at 15 ppm due to the large  $m/z$  range used in the data collection ( $m/z$  50-1000). Next, the theoretical isotopic distribution patterns of the potential elemental compositions were compared to the observed isotopic distribution. The peak was only considered positively identified if the distribution of the measured ion did not deviate by more than 5% from the theoretical isotopic distribution, except where spectral overlap was noted or there was excessive background noise. The theoretical distributions were found using the free webtool from the Scientific Instrument Services (SIS) Isotope Distribution Calculator and Mass Spec Plotter.

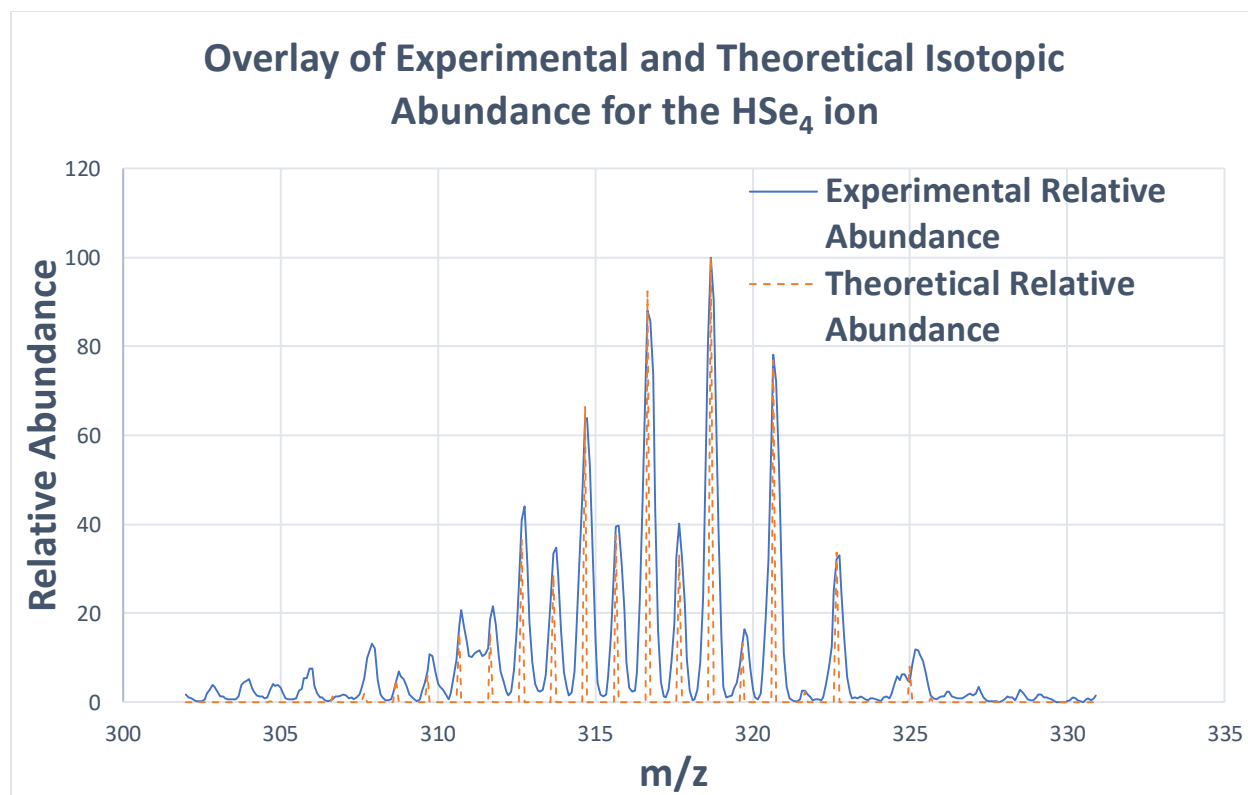


Figure 5.2 Overlay of the experimental (solid blue line) and theoretical (dashed orange line) isotopic abundance for the HSe<sub>4</sub> ion. The data was collected from a sample of 10 mM Se in 1:1 (v/v) BA-ET. The theoretical isotopic relative abundance was calculated using the Scientific Instrument Services Isotope Distribution Calculator and Mass Spec Plotter. The differences in isotopic distribution evident below m/z 309 and at m/z 325 were attributed to overlap from low-intensity ions and background noise, respectively.

When possible, the ions of interest were isolated and fragmented using collision activated dissociation (CAD). The fragments and neutral losses observed were then compared to the most likely elemental composition of the ion to see if the losses were feasible and made sense. For example, an ion predicted to be entirely comprised of Se and Te atoms but which showed a loss of ethanethiol in CAD experiments would not feasibly be possible. Therefore, the elemental composition assignment would restart from the beginning of the described process until a positive match could be made that fit all available data. When performing the CAD experiments, low resolution mode was used. The ions were trapped with a  $q$  value of 0.25 and an isolation window ranging from  $\pm 0.4$ -1 m/z units. The isolation window was adjusted on a case-by-case basis to ensure that only one m/z was being isolated at a time. The CAD energy used ranged from 10-40

arbitrary units and was adjusted during each experiment to provide the best fragment ion intensity without lowering the precursor ion intensity below 10 % relative abundance.

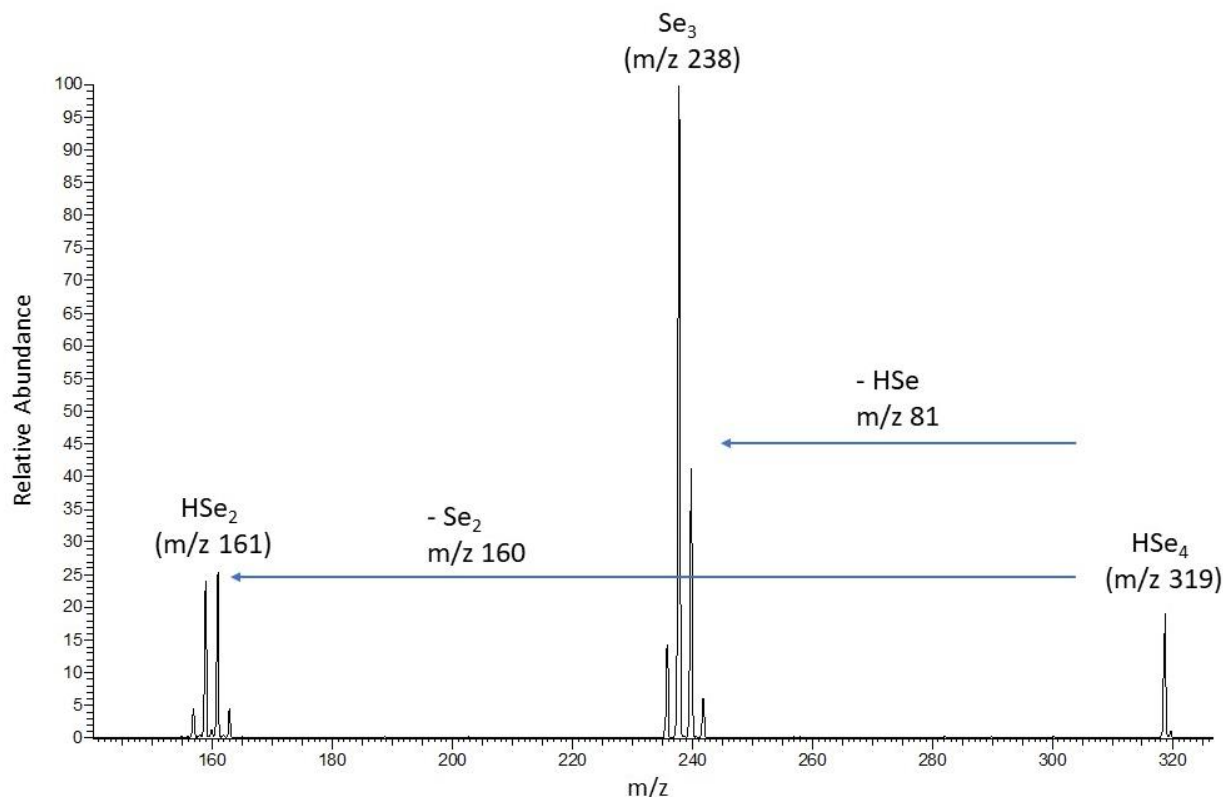


Figure 5.3 Fragmentation pattern of the HSe<sub>4</sub> ion collected from a sample of 10 mM Se in 1:1 (v/v) BA:ET. During experimentation, the monoisotopic ion was not correctly identified for fragmentation experiments and the ion of m/z 319 was instead fragmented. The corresponding losses therefore show isotopic distributions and are not single peaks. The losses align with the assignment of the ion as HSe<sub>4</sub>.

#### 5.2.4 Other Spectroscopic Characterization

Raman, X-ray diffraction, and <sup>1</sup>H NMR spectra were collected by Swapnil Deshmukh, Nicole LiBretto, Kyle Weideman and Jeffrey Miller at Purdue University's Davidson School of Chemical Engineering. X-ray absorption (XAS) spectra were collected at Argonne National Laboratory.

Raman spectroscopy was performed using a Horiba/Jobin-Yvon HR800 at an excitation wavelength of 632.8 nm and laser power of 4.25 mW. The samples were prepared in a glovebox

as described and then sealed inside a quartz cuvette (Hellma Analytics fluorescence cuvette) prior to removal from the glovebox.

$^1\text{H}$  NMR spectra were collected using a Bruker AV-III-HD NMR with deuterated acetonitrile solvent. For quantitative experiments, the standard used for normalization was ethylene carbonate.

X-ray absorption spectroscopy was performed in situ using Argonne National Laboratory's Advanced Photon Source at a 10-BM beamline. Scans took approximately 10 minutes each and were performed along the Se K edge at 12.6580 keV. The fast scan mode was used to scan from 250 eV below the edge to 550 eV above the edge. The samples tested were 0.1 M solutions prepared and sealed in a collection tube inside a glovebox. To fit the XAS data, standard EXAFS fitting procedures were conducted. For calibration, the foil's intrinsic loss factor ( $S_0^2$ ) was calculated to be 0.75. To fit the magnitude and imaginary components, a least squared fit for the first shell of  $r$ -space and isolated  $q$ -space were performed on the  $k^2$  weighted Fourier transform data between 2.7 to 10  $\text{\AA}^{-1}$ . The scattering pairs used for the FEFF6 calculations were Se-S (CN=1,  $R=2.24 \text{ \AA}$ ), Se-Se (CN=1,  $R=2.35 \text{ \AA}$ ), and Se-Te (CN=1,  $R=2.52 \text{ \AA}$ ).

X-ray diffractograms (XRD) were collected using a Rigaku Smart Lab diffractometer. A Cu  $K\alpha$  ( $\lambda = 1.5406 \text{ \AA}$ ) source was used in Bragg-Brentano mode at a power of 40 kV/44mA. To prepare the samples, the pure metallic powders were dispersed in isopropyl alcohol and then drop cast on a piece of soda lime glass.

### **5.3 Analysis of Se and Te Solutions in Monoamine- and Diamine-Thiol Solvent Systems**

#### **5.3.1 Selenium Dissolution in Monoamine vs Diamine Solutions**

At ambient temperature and pressure, selenium dissolves in high concentrations in both monoamine-thiol and diamine-thiol solutions.<sup>20,29</sup> However, the species that Se forms in these solutions are not well characterized. Previous studies have shown that dialkyl disulfide species form when Se is added to monoamine-monothiol solvents but not in diamine-monothiol solvents.<sup>20,29</sup> It is therefore clear that Se behaves differently depending on the solvent system and may have a different dissolution mechanism in monoamine-thiol solvents compared to diamine-thiol solvents. To study these differences, we prepared two different solutions of 0.1 M Se, one solution using a 1:1 (v/v) butylamine-ethanethiol (BA-ET) solvent and one solution using a 1:1

(v/v) ethylenediamine-ethanethiol (EN-ET) solvent. A variety of characterization techniques were used to analyze these solutions.

The characterization of the two Se solutions began with Raman analysis. The first step was to take background spectra of the pure solvents: BA-ET and EN-ET. The Se solutions were then compared to the corresponding background spectrum to identify bonds that formed during the Se dissolution. In the BA-ET solution, the Se addition produced three new peaks in the Raman spectrum. There were two broad, low intensity peaks at 260 and 274  $\text{cm}^{-1}$  while the third peak was sharper and at 242  $\text{cm}^{-1}$ . After consulting the literature, each new peak was assigned to a type of Se-Se bond. According to the literature, trigonal crystal structure Se has a Se-Se peak at 234  $\text{cm}^{-1}$  while orthorhombic, monoclinic, and amorphous Se structures occur above 250  $\text{cm}^{-1}$ .<sup>35,36</sup> Therefore, the new peak we observed at 242  $\text{cm}^{-1}$  was assigned to the trigonal crystal structure of Se while the other two peaks at 260 and 274  $\text{cm}^{-1}$  were assigned to Se in either the orthorhombic, monoclinic, or amorphous structure. It was not possible to determine which of these three possibilities was in the solution based on the Raman spectra alone. However, previous studies on similar solutions have suggested that Se exists in amine-thiol solvent systems as monoclinic  $\text{Se}_8$  rings.<sup>29</sup> It is possible that at least one of the two broad peaks in our spectrum corresponds to these previously proposed monoclinic  $\text{Se}_8$  rings. However, unlike the previous study, our Raman spectra suggests that Se clusters with several different types of Se bonding are present in these solutions, rather than just monoclinic  $\text{Se}_8$  rings.

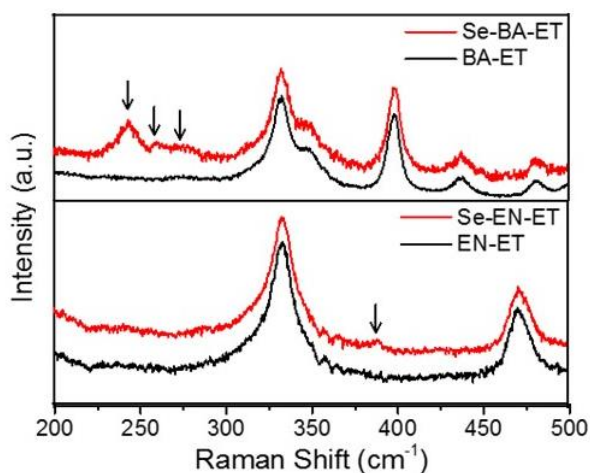


Figure 5.4 Raman spectrum of Se in BA-ET (top) and EN-ET (bottom). The Se solutions are shown in red and the corresponding background spectra are shown in black. The arrows indicate the features present only in the Se solutions.

When the Se in EN-ET solution was compared to its background, only one very small new feature was observed at  $388\text{ cm}^{-1}$ . This peak was obviously not a result of Se-Se bonds. Based on the literature, this new peak was assigned to S-Se bonds.<sup>37</sup> The Raman data therefore clearly showed a significant difference between the Se species formed in BA-ET compared to EN-ET, with BA-ET resulting in various types of Se-Se bonding and EN-ET resulting exclusively in S-Se bonding. However, the EN-ET results did not agree with previous studies, which also saw Raman evidence of Se-Se bonding.<sup>20</sup> Therefore, the reliability of the EN-ET results were somewhat questionable and required further investigation.

The next technique used to characterize the two solutions was  $^1\text{H}$  NMR. Again, the solutions containing Se were compared to background spectra of pure BA-ET and EN-ET. Despite the significant differences observed between the two Se solutions, the NMR data was surprisingly similar for Se in BA-ET and EN-ET. Both samples had two new peaks compared to the background: a quartet at 2.72 ppm and a triplet at 1.28 ppm. Both of these peaks correspond to diethyl disulfide, confirming previous reports that Se dissolution in amine-thiol solvent systems results in the formation of dialkyl disulfides.<sup>20,29</sup> However, these were the only new peaks observed in either Se-containing solution. Despite the Raman data showing clear evidence of Se-Se bonds in BA-ET and S-Se bonds in EN-ET, neither were observed in the  $^1\text{H}$  NMR spectra. Se clusters would not be observed in a  $^1\text{H}$  NMR since there are no hydrogens in Se clusters. However, the ethanethiol-Se bonds should be theoretically discernable by  $^1\text{H}$  NMR. One possible explanation for the missing ethanethiol-Se bonds in the EN-ET NMR is that the ethanethiol ions and ethanethiol-Se ions have similar chemical shifts, meaning that they may have been present but mistakenly identified as ethanethiol ions. Another explanation, put forth by Webber et al<sup>20</sup> for similar solutions, is that the exchange between Se-Se clusters and ethanethiol-Se species is too fast to be observed by NMR. Since Raman operates on a faster timescale, the ethanethiol-Se species could be observed by Raman spectroscopy, even though they could not be detected by NMR.

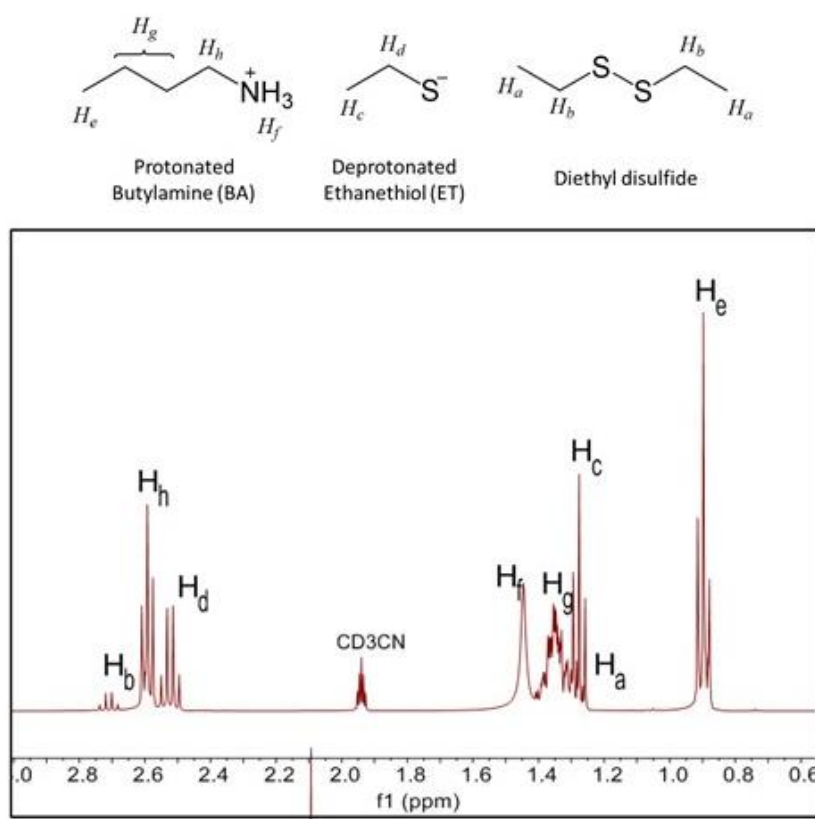


Figure 5.5 NMR Spectrum of Se in BA-ET. Only the area of interest (from 0.6-3 ppm) is shown. The corresponding protons are labeled according to their chemical assignments. The corresponding chemical assignments are labeled on the chemical structures above the spectrum.

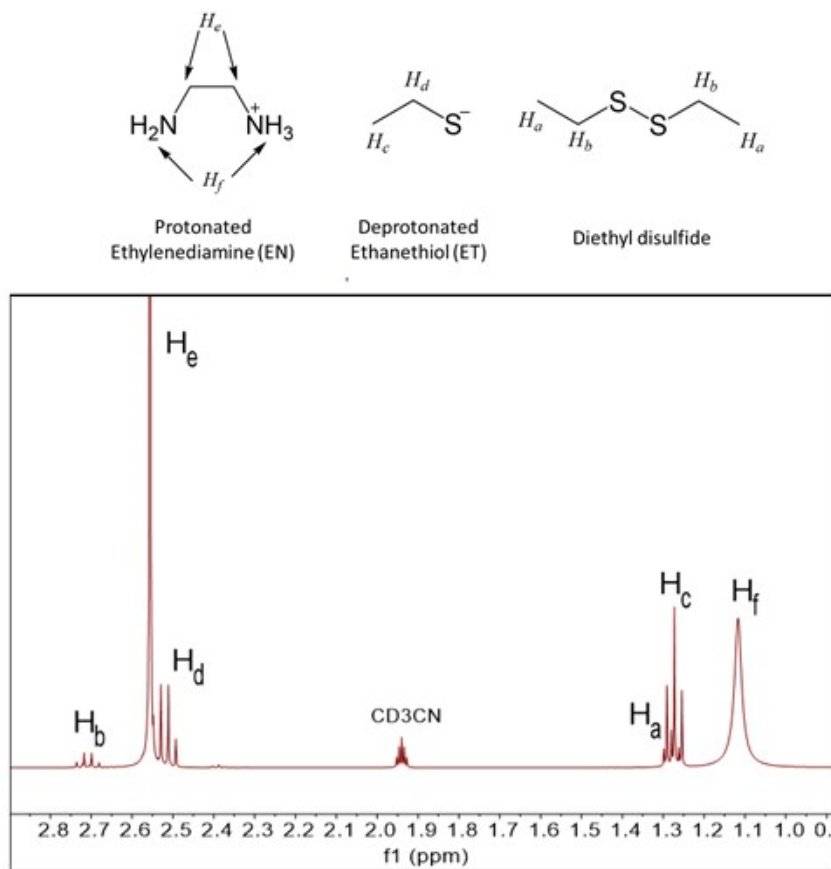


Figure 5.6 NMR Spectrum of Se in EN-ET. Only the area of interest (from 1-3 ppm) is shown. The corresponding protons are labeled according to their chemical assignments. The corresponding chemical assignments are labeled on the chemical structures above the spectrum.

The next analytical technique used to study these two solutions was X-ray absorption spectroscopy. This technique usually utilizes two modes: X-ray absorption near edge spectroscopy (XANES) and extended X-ray absorption fine structure (EXAFS). XANES is used to identify the chemical state of the solution while EXAFS is used to identify the coordination environment in the solution and is especially useful for metals. The background spectra for the X-ray absorption analyses was pure Se foil. Therefore, the XANES and EXAFS can only detect changes in the Se in the solution and cannot detect any changes that do not involve Se.

The XANES edge energy was lower for both solutions than it was for the pure Se foil. This lowering of edge energy suggests that the Se in the solutions was reduced. Unfortunately, the edge energy of the -2 oxidation state and metallic Se are too close in energy and could not be deconvolved. However, the white line intensities of the Se in BA-ET and EN-ET could be

compared to produce some comparative information. Since the white line intensity of the Se in BA-ET solution was higher, it was concluded that there is likely some differences in the bonding modes between the two solutions. However, no conclusive information was obtained.

While the XANES spectra were inconclusive, EXASF data did suggest that the Se coordination in the two solutions was very different. In the BA-ET solution, the EXASF fitting resulted in a predicted average bond distance of 2.34 Å, which is the bond distance of an Se-Se bond.<sup>38</sup> The coordination number for the BA-ET solution was 1.6, suggesting that Se clusters of two and three are most prevalent. Meanwhile, the EN-ET average bond distance was calculated at 2.20 Å, which corresponds to S-Se bonds.<sup>38</sup> This shorter bond distance suggests that S-Se bonds are either the only species in the EN-ET solutions or are much more common than Se-Se bonds. The coordination number for Se in the EN-ET solution was 0.8, further lending support to the conclusion that Se mainly exists as a lone Se atom with a single thiolate ligand.

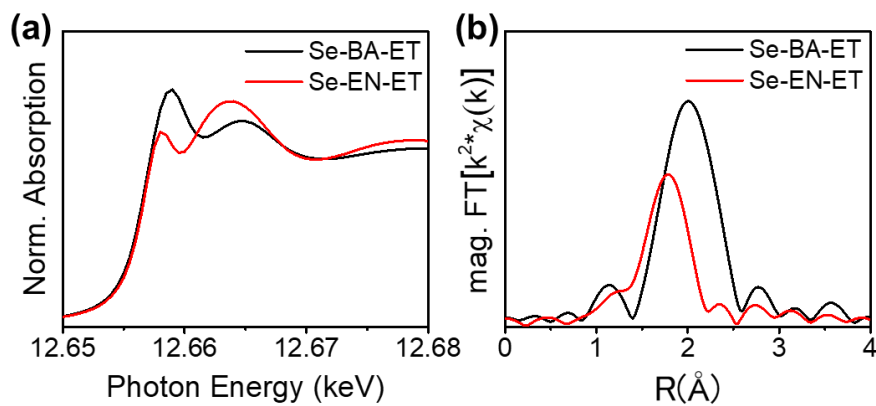


Figure 5.7 XAS spectra for Se in BA-ET (black trace) and EN-ET (red trace). Figure 5.7 (a) is the XANES K-edge for Se while (b) is the corresponding Fourier transform magnitude component of the EXASF spectra.

Since mass spectrometry has the advantage of identifying individual components of a complex mixture, (-)ESI-MS/MS was the final analytical technique used to compare the two Se solutions. The Se concentration for this technique was necessarily decreased from 0.1 M to 0.01 M. While both positive and negative mode ESI spectra were collected, only the negative mode showed any peaks containing Se, so only this mode will be discussed here. It was immediately clear from the mass spectra of the Se in BA-ET and EN-ET solutions that the two solutions were incredibly different. For the BA-ET solution, numerous  $\text{HSe}_x^-$  clusters were observed, with cluster

sizes varying between two and six Se atoms. The  $\text{HSe}_2^-$  ion was the most abundant, which matches the coordination number observed in the EXASf analysis. The mass spectrum for Se in EN-ET, meanwhile, was dominated by the  $m/z$  141 peak, which was identified as the  $\text{C}_2\text{H}_5\text{SSe}^-$  ion. The only positively-identified ion with Se-Se bonds was  $\text{HSe}_2^-$ , although there were some very low-intensity ions present that appeared to be Se clusters but could not be positively identified. This result agrees very well with the other analytical data, suggesting that Se with a single thiol ligand is the primary species formed during dissolution and Se-Se bonds are less prevalent.

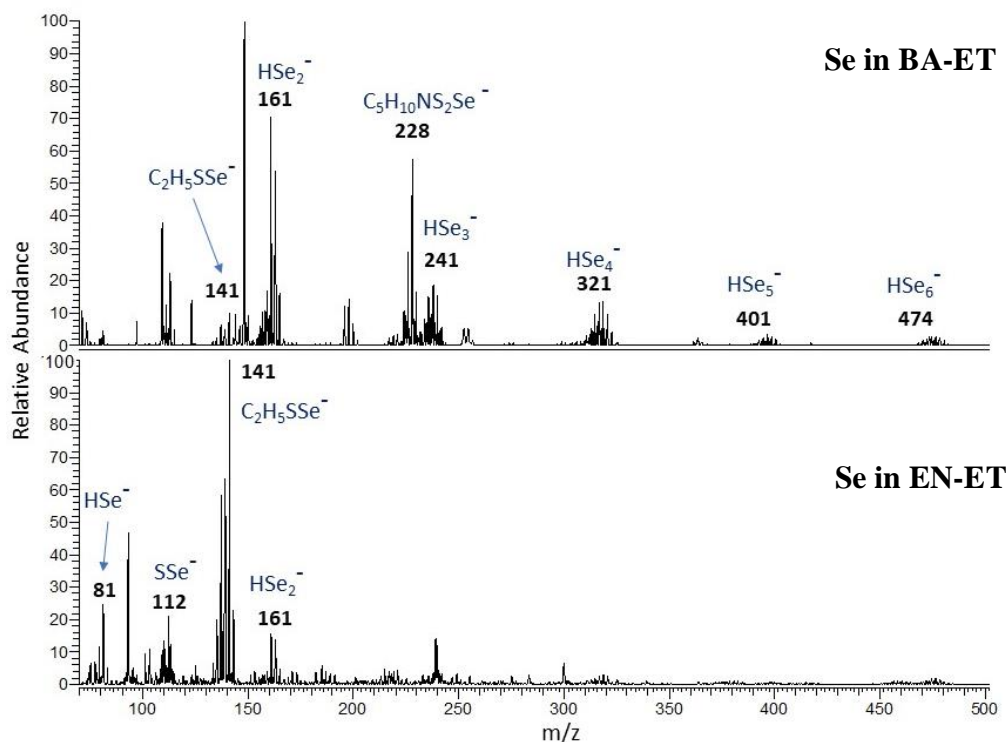


Figure 5.8 (-)ESI-MS spectra of Se in BA-ET (top) and EN-ET (bottom). Labeled masses are for the monoisotopic mass of the corresponding assignment. Unlabeled peaks either contain no selenium or were not successfully identified.

Table 5.1 Elemental composition of ions detected using (-) ESI-MS for Se in BA-ET and Se in EN-ET. For some ions, the high resolution MS signal was too low for accurate calculation of the error or calculation of the  $m/z$  with high accuracy (more than two decimal points). Assignments for these ions were based on low-resolution mass and isotopic distributions. These ions are marked in the table with \*. All  $m/z$  reported are for the monoisotopic mass.

<b>Se in BA-ET</b>		
<i>m/z</i>	<b>Elemental Composition</b>	<b>Error from expected mass (+/- ppm)</b>
112.89743	HSSe	13.83
148.02660	C <sub>5</sub> H <sub>10</sub> NS <sub>2</sub>	11.03
160.84253	HSe <sub>2</sub>	13.71
227.94314	C <sub>5</sub> H <sub>10</sub> NS <sub>2</sub> Se	10.41
240.75861	HSe <sub>3</sub>	7.34
320.67581	HSe <sub>4</sub>	7.63
400.59277	HSe <sub>5</sub>	5.68
474.00*	HSe <sub>6</sub>	Assigned based on isotopic patterns
550.50*	HSe <sub>7</sub>	Assigned based on isotopic patterns

<b>Se in EN-ET</b>		
<i>m/z</i>	<b>Elemental Composition</b>	<b>Error from expected mass (+/- ppm)</b>
80.92523	HSe	17.69
92.98412	C <sub>2</sub> H <sub>5</sub> S <sub>2</sub>	15.08
111.88941	SSe	12.21
140.92852	C <sub>2</sub> H <sub>5</sub> SSe	9.58
160.84194	HSe <sub>2</sub>	10.07

Ultimately, the data collected here suggests that in monoamine-monothiol solutions, Se addition results in the formation of dialkyl disulfide and relatively small clusters of Se atoms. On the other hand, Se added to diamine-monothiol solutions results in the formation of dialkyl disulfide and RSSe species in solution. It is clear that the addition of Se is directly responsible for the formation of the dialkyl disulfide, but the exact mechanism is not yet known. In the amine-thiol solvent system, the thiol exists as a thiol ion (RS<sup>-</sup>). To form a disulfide, two of these negatively-charged sulfurs would have to interact and form the disulfide bond. This is highly unlikely due to the repulsion of like charges. Therefore, it is possible that the addition of Se, which can easily form negatively-charged Se ions, provides the means of forming the disulfide bond; the extra electrons from one of the RS<sup>-</sup> ions are transferred to one or more Se, and the resulting RS

species is no longer repelled by the  $RS^-$  ions still in solution. These two species can then react to form the disulfide bond.

The reason why diamines primarily lead to  $RSSe$  species while monoamines primarily lead to  $Se_x$  species is unclear. Any negative ion in solution must be coordinated with a corresponding positive ion to remain stable. These positive ions would likely dissociate during the ESI-MS/MS process, leading to the observation of the negative ion only. The positive counter ion in amine-thiol solvent systems is the amine. Diamines are more basic than monoamines, so it is possible that  $RSSe$  species require a stronger counterion than  $Se_x$  ions, leading monoamine solutions to form only  $Se_x$  ions while diamines are capable of forming  $RSSe$  ions. However, more studies need to be performed to further probe this reaction.

### 5.3.2 Tellurium Dissolution in Diamine Solutions

As members of the same periodic group, Se and Te share some key similarities in their reactivity. Despite their similarities, these two elements also differ significantly. Te is larger, less electronegative, is classified as a metalloid, and is notoriously difficult to dissolve.<sup>39</sup> The characteristics of the Te crystal structure also have key differences compared to the crystal structure of Se. While they share a naturally occurring trigonal crystal structure, the bonds inside the crystal structure are quite different. The trigonal crystal structure consists of long chains of atoms that are crosslinked. For Se, the individual chains have strong bonding interactions, but the crosslinks are relatively weak. Therefore, separating the chains is relatively easy while breaking apart an individual chain is more difficult. Meanwhile, the Te crystal structure does not have this large difference in bond strength: the crosslinks are approximately as strong as the chain bonds.<sup>39</sup>

Considering these significant differences, it is expected that Se and Te behave very differently in amine-thiol solvent systems. While Se is fairly easy to dissolve in a range of monoamine-monothiol and diamine-monothiol solvent systems, Te is only soluble in diamine-monothiol and not in monoamine-monothiol solvent systems. Additionally, in our preliminary testing, we found that Te is much less soluble in diamine-monothiol solvents than Se. In EN-ET, we could only dissolve Te up to 0.6 M, but Se dissolved at concentrations over 6 M. When the solvent was evaporated from the two solutions (Te in EN-ET and Se in EN-ET), a process necessary for solution processing of thin films, the two solutions behaved very differently. For the

Te solution, metallic Te precipitated as the solvent evaporates while Se dried down to produce a stable Se complex. We concluded that the species in solution must be very different for Se and Te.

Since we had already extensively characterized Se dissolved in EN-ET, the next step was to characterize Te in EN-ET. First, Raman analysis was performed on a 0.5 M Te in EN-ET solution and compared to a background Raman spectrum of pure metallic Te powder. The background spectrum had two sharp peaks between 100-150  $\text{cm}^{-1}$ . These two peaks are the types of bonds present in crystalline Te.<sup>40,41</sup> The Te in EN-ET was very different compared to this background. The crystalline peaks observed in the background were entirely absent and three clearly visible (if unresolved) peaks between 150-200  $\text{cm}^{-1}$  were observed. Previous literature reports have identified peaks between 150-175  $\text{cm}^{-1}$  as amorphous Te with little Te-Te interactions.<sup>40,41</sup> The peak at approximately 160  $\text{cm}^{-1}$  in our spectrum was therefore assigned to amorphous Te. Based on similar solutions, the two peaks from 175-200  $\text{cm}^{-1}$  were assigned to S-Te bonds.<sup>42,43</sup>

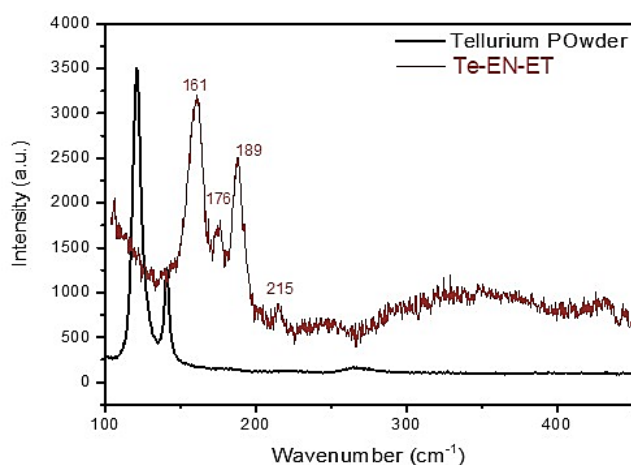


Figure 5.9 Raman spectra of Tellurium powder (black trace) and Tellurium in EN-ET (red trace). The new peaks present only in the Te-EN-ET solution are labeled with the corresponding wavenumber.

While the next step in the analysis of the Se in EN-ET solution was NMR and XAS analysis, these two techniques could not be performed for the analogous Te solution. NMR was not possible because the addition of a third solvent (necessary for NMR analysis) immediately precipitated the Te, no matter which solvent was tried. The XAS was not possible because Argonne National Lab,

where the other XAS analyses for this study were conducted, does not have equipment capable of performing XAS on Te due to its very high edge energy.

Since NMR and XAS analysis were not possible, the analysis of the Te in EN-ET solution primarily relied on ESI-MS/MS analysis. Like the Se solutions, Te ions were only observed in negative mode ESI, so the positive mode ESI data will not be discussed here. The ESI-MS/MS data had numerous ions present, although the spectrum was not as complex as the analogous Se solution. Two main types of ions were observed:  $\text{HTe}_x^-$  and  $\text{C}_2\text{H}_5\text{STe}_x^-$  ions. For the  $\text{HTe}_x^-$  ions, only Te clusters of two, three, and four were observed. None of these ions were above 50 % relative abundance, and the only ion observed above 10 % abundance was  $\text{HTe}_2^-$ . As a group, the  $\text{C}_2\text{H}_5\text{STe}_x^-$  ions were much more abundant. Te clusters of one, two, and three observed, with  $\text{C}_2\text{H}_5\text{STe}_2^-$  ions being the most abundant in the entire spectrum. Gas phase Te has previously been studied by mass spectrometer, and the results suggested that  $\text{Te}_2$  clusters are the most stable gas phase structure for Te.<sup>39</sup> Our data fits well with this previous observation, with ions containing  $\text{Te}_2$  being highly abundant and the most abundant for each ion type.

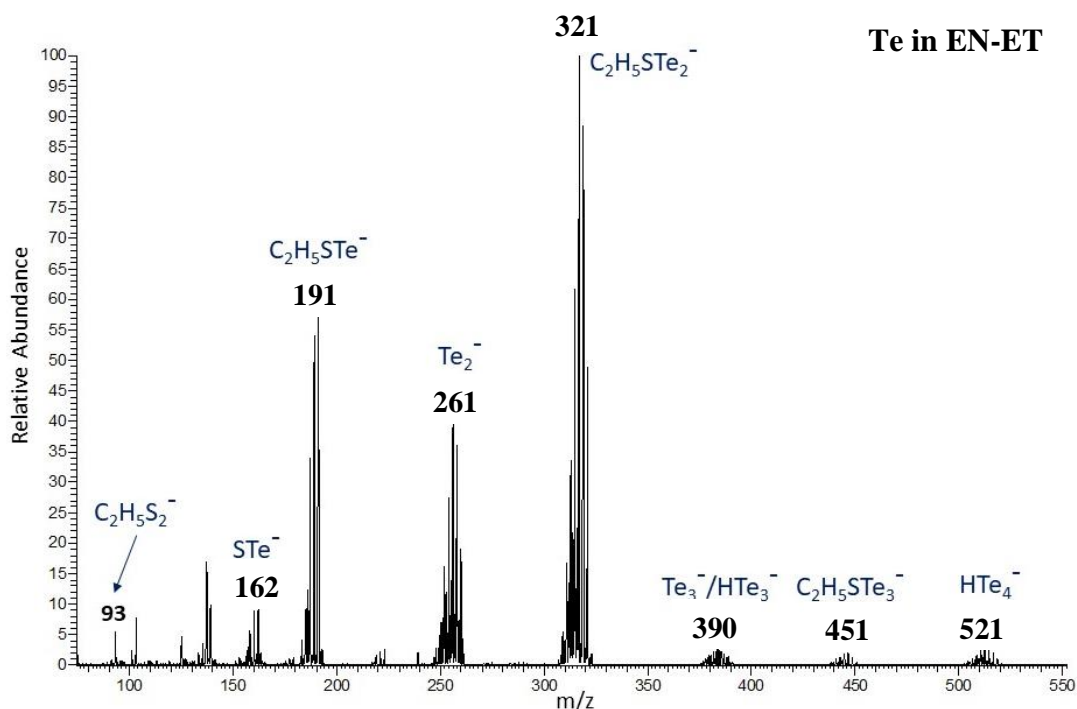


Figure 5.10 (-)ESI-MS spectrum of tellurium in EN-ET. Labeled masses are for the monoisotopic mass of the corresponding assignment. Unlabeled peaks either contain no tellurium or were not successfully identified.

Table 5.2 Elemental composition of ions detected using (-) ESI-MS for Te solutions in EN-ET. For some ions, the high resolution MS signal was too low for accurate calculation of the error or calculation of the  $m/z$  with high accuracy (more than two decimal points). Assignments for these ions were based on low-resolution mass and isotopic distributions. These ions are marked in the table with \*. All  $m/z$  reported are for the monoisotopic mass.

<b>Te in EN-ET</b>		
<i>m/z</i>	<b>Elemental Composition</b>	<b>Error from expected mass (+/- ppm)</b>
136.95613	C <sub>3</sub> H <sub>5</sub> S <sub>3</sub>	9.79
161.87906	STe	8.12
190.91805	C <sub>2</sub> H <sub>5</sub> STe	6.19
260.82089	HTe <sub>2</sub>	4.48
320.82420	C <sub>2</sub> H <sub>5</sub> STe <sub>2</sub>	3.45
389.71815	Te <sub>3</sub> /HTe <sub>3</sub>	0.08
450.75*	C <sub>2</sub> H <sub>5</sub> STe <sub>3</sub>	Assigned based on isotopic pattern
520.67*	HTe <sub>4</sub>	Assigned based on isotopic pattern

While Se in EN-ET also exhibited HSe<sub>x</sub><sup>-</sup> ions, we hypothesized that the HTe<sub>x</sub><sup>-</sup> ions are not found in solution but instead are artifacts of the ESI process. We know that as solvent evaporates from this solution, Te precipitates spontaneously. Since ESI involves solvent evaporation, we hypothesized that the Te begins to precipitate and the metallic clusters are ionized and observed in the mass spectrum as the HTe<sub>x</sub><sup>-</sup> ions. Therefore, we suggest here that there is a possibility that some of the observed HTe<sub>x</sub><sup>-</sup> ions may not exist in solution. However, To determine whether this is the case, further studies would need to be performed on diluted Te solutions to see whether the relative abundance of the HTe<sub>x</sub><sup>-</sup> ions changed as a function of concentration.

### 5.3.3 Co-dissolution of Selenium and Tellurium

Since Se and Te are capable of forming bonds and alloys, we decided to next test the behavior of Se and Te in an EN-ET solvent system to see whether Se-Te bond formation occurred. In preliminary testing, the presence of Se in the solution had a considerable impact on the solubility and behavior of Te. Firstly, in ethylenediamine-ethanethiol, Te was soluble up to 0.6 M; adding Se to the solution allowed Te to dissolve at much higher concentrations, up to 2 M. Secondly, when Te was dissolved in ethylenediamine-ethanethiol and the solvent was evaporated off, metallic Te crystals precipitated from the solution. When Se was added to the solution, evaporation of the solvent resulted in the precipitation of an organometallic complex, not pure Te. Therefore,

we concluded that Te must form different species in solution when Se is present compared to when Te is dissolved on its own.

A range of tests were used to study the Te species in EN-ET when Se was also present and the results were then compared to Te in EN-ET without Se. First, (-)ESI-MS was used to identify the major compounds in the solution using the technique previously described. This analysis resulted in the identification of several different species, including ions of the form:  $\text{RSSe}_x$ ,  $\text{RSTe}_y$ ,  $\text{RSSe}_x\text{Te}_y$ , and  $\text{Se}_x\text{Te}_y$ . When Te was dissolved on its own in EN-ET, the major ions were Te ions with thiolate ligands. Based on evaporation experiments, these thiolate ligands do not remain in the finished thin film, but instead dissociate to regenerate metallic Te. In the EN-ET solution with Se and Te, these same Te ions with thiolate ligands were observed, but additional  $\text{Se}_x\text{Te}_y$  complexes both with and without thiolate ligands were observed. Since the evaporation of these solutions resulted in an organometallic complex rather than metallic Te, we hypothesized that these thiolate ligands on the  $\text{Se}_x\text{Te}_y$  complexes were preserved during solvent evaporation and that the Se-sulfur bond must be the key to the organometallic preservation.

To confirm the species found in solution, additional tests were conducted. First, the SeTe-EN-ET solution was analyzed using Raman spectroscopy. In the Raman spectrum, numerous peaks were observed, including: clear peaks for Se-Se bonds, a small feature identified as Te-Te bonds, and an additional broad peak at  $175\text{-}225\text{ cm}^{-1}$  that could, according to the literature,<sup>44,45</sup> correspond to either S-Se or Se-Te bonds. Since both S-Se and Se-Te bonds were observed in the ESI-MS spectra, it was unclear whether the broad peak observed in the Raman spectra was due to S-Se bonds, Se-Te bonds, or a combination of both.

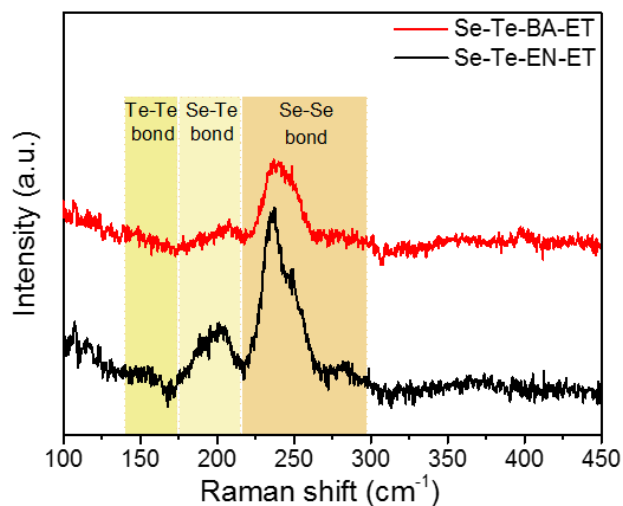


Figure 5.11 Raman spectra for the co-dissolved Se and Te in both BA-ET (top red trace) and EN-ET (bottom black trace). The three major types of peaks were Te-Te bonds, Se-Te bonds, and Se-Se bonds. These regions are labeled with graduated boxes on the spectra. The Se-Te bond region could also potentially correspond to S-Se bonds.

Next, XAS analysis was conducted on the solution. The spectra were collected along the Se edge. Fitting of the data showed three different types of bonds present: S-Se, Se-Se, and Se-Te bonds. The total coordination number was two. This data suggests that in the  $\text{RSSe}_x\text{Te}_y$  ions observed in the mass spectra, the thiolate ligand is primarily attached to a Se atom rather than to a Te atom.

Since the spectral data from the SeTe-EN-ET suggested that both  $\text{RSSe}_x\text{Te}_y$  and  $\text{Se}_x\text{Te}_y$  species exist in solution and at higher concentrations of Te than when no Se was present, we thought it likely that the formation of Se-Te bonds was a significant and different dissolution route for Te. We hypothesized that, in solution,  $\text{Se}_x$  ions may be acting as nucleophiles and forming Se-Te complexes, much like the thiolate ions are believed to perform nucleophilic attacks on both Se and Te to form RS-Se and RS-Te complexes. We hypothesized that if Se ions were a major contributing factor to the dissolution of Te, then adding both Se and Te to a BA-ET solvent system (in which Te is not soluble on its own) would result in Te dissolution. To test this hypothesis, we first dissolved Se in BA-ET, as previously described, to generate  $\text{Se}_x$  ions in solution. Once the potential Se nucleophiles were generated, we added Te to the solution. Some dissolution was immediately noted.

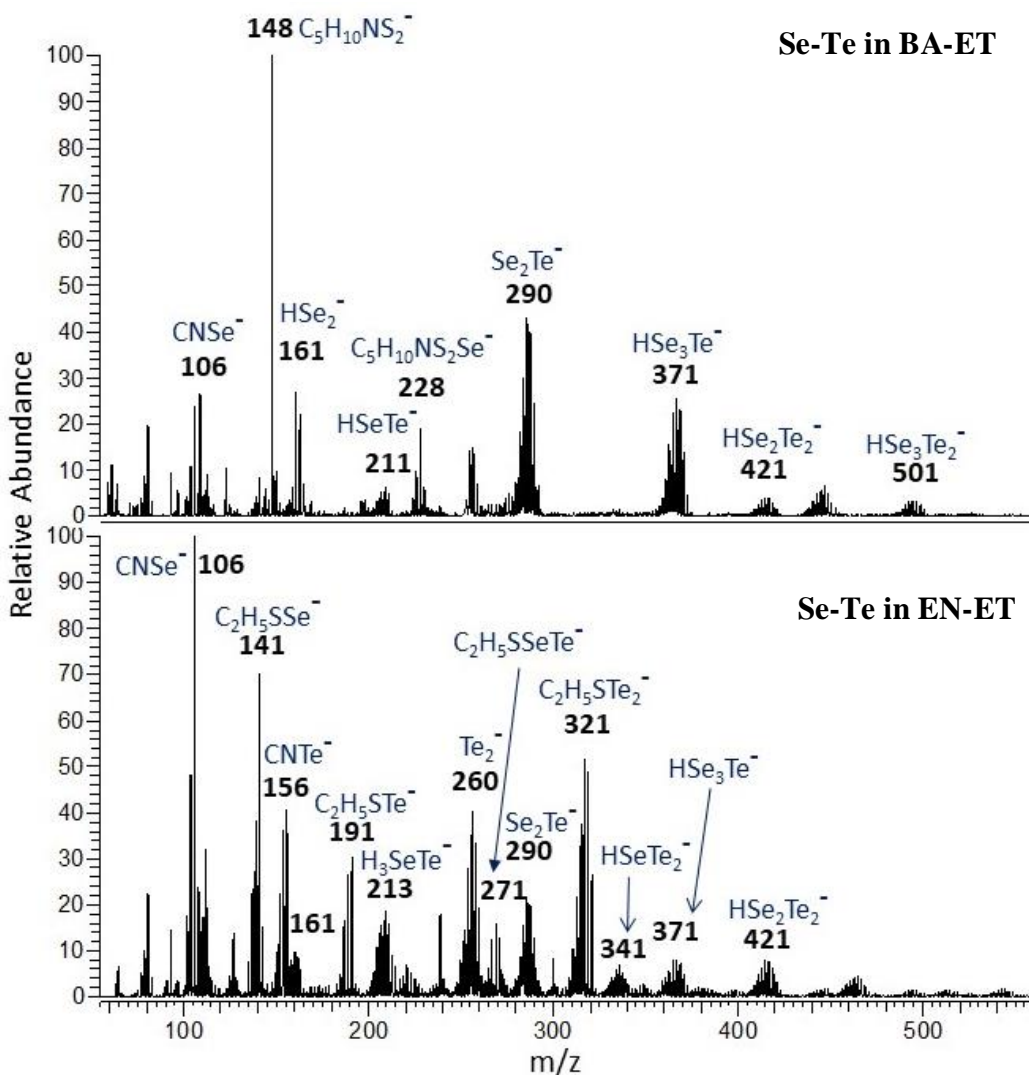


Figure 5.12 (-)ESI-MS spectra of SeTe dissolved in BA-ET (top) and in EN-ET (bottom). Labeled masses are for the monoisotopic mass of the corresponding assignment. Unlabeled peaks either contain no selenium or tellurium or were not successfully identified.

To confirm whether Te was successfully dissolved in the Se-BA-ET solution, we performed several analytical tests. First, mass spectrometry experiments confirmed the presence of  $Se_xTe_y$  compounds in solution. Interestingly, no significant peaks with thiolate ligands were noted in the mass spectra, suggesting that the  $Se_x$  nucleophiles were mostly responsible for the Te dissolution. Additionally, it was noted that in the  $Se_xTe_y$  ions, the number of Te atoms in the cluster was always less than or equal to the number of Se atoms ( $x \geq y$ ). This suggested that there was a limit to the Te solubility that was dependent on the amount of Se in solution. Experiments were then performed to test the solubility limit, varying the relative mol ratio of Se:Te that could dissolve in solution.

We found that the maximum ratio was 3:2 Se:Te, suggesting that, while many different clusters could form, a cluster of three Se atoms could likely dissolve at most two Te atoms. The mass spectrometry experiments further confirmed this finding: the largest cluster observed in the mass spectrum was HSe<sub>3</sub>Te<sub>2</sub>.

For Te on its own in EN-ET, we argued that the Te<sub>x</sub> clusters observed may be a result of evaporation during the ESI process. In drying experiments, we found that metallic Te crashes out readily as soon as the solvent begins to evaporate. However, this same precipitation was not observed when Se and Te were co-dissolved. This suggests that the Se<sub>x</sub>Te<sub>y</sub> clusters are stable, even as the solvent begins to evaporate. Therefore, we concluded that these Se<sub>x</sub>Te<sub>y</sub> clusters are likely not the result of precipitation within the ESI source but instead are found within the solution itself.

Table 5.3 Elemental composition of ions detected using (-) ESI-MS for Se-Te solutions in BA-ET and in EN-ET. For some ions, the high resolution MS signal was too low for accurate calculation of the error or calculation of the m/z with high accuracy (more than two decimal points). Assignments for these ions were based on low-resolution mass and isotopic distributions. These ions are marked in the table with \*. All m/z reported are for the monoisotopic mass.

<b>Se-Te in BA-ET</b>		
<i>m/z</i>	<b>Elemental Composition</b>	<b>Error from expected mass (+/- ppm)</b>
105.92036	CNSe	12.39
148.02625	C <sub>5</sub> H <sub>10</sub> NS <sub>2</sub>	9.00
160.84213	HSe <sub>2</sub>	11.25
210.83132	HSeTe	6.16
227.94271	C <sub>5</sub> H <sub>10</sub> NS <sub>2</sub> Se	5.58
289.73993	Se <sub>2</sub> Te	4.18
370.66490	HSe <sub>3</sub> Te	4.95
420.83*	HSe <sub>2</sub> Te <sub>2</sub>	Signal too low
500.67*	HSe <sub>3</sub> Te <sub>2</sub>	Signal too low

Table 5.3 continued

<b>Se-Te in EN-ET</b>		
<i>m/z</i>	<b>Elemental Composition</b>	<b>Error from expected mass (+/- ppm)</b>
105.91988	CNSe	7.86
140.92789	C <sub>2</sub> H <sub>5</sub> SSe	5.11
155.90941	CNTe	4.24
160.84100	HSe <sub>2</sub>	4.23
190.91736	C <sub>2</sub> H <sub>5</sub> STe	2.56
212.84688	H <sub>3</sub> SeTe	5.68
259.81210	Te <sub>2</sub>	0.78
270.83359	C <sub>2</sub> H <sub>5</sub> SSeTe	0.73
289.73917	Se <sub>2</sub> Te	1.56
320.82318	C <sub>2</sub> H <sub>5</sub> STe <sub>2</sub>	0.27
340.83*	HSeTe <sub>2</sub>	Signal too low
370.75*	HSe <sub>3</sub> Te	Signal too low
420.83*	HSe <sub>2</sub> Te <sub>2</sub>	Signal too low

Next, both Raman and XAS analysis of the solution were conducted. In the Raman analysis, Se-Se bonds were seen clearly, while a small feature similar to the Se-Te and S-Se bonds seen in the SeTe-EN-ET solution was also observed. Additionally, no discernable Te-Te bonding was seen, lending further evidence that the number of Se-Te bonds in the solution far outweighed the number of Te-Te bonds. The XAS analysis showed no evidence of S-Se bonds but did show evidence for Se-Se and Se-Te bonds, with an overall lower coordination number than that seen in the EN-ET solvent system. These findings further support the conclusion that Se nucleophilic ions are the main actors in the dissolution of Te in BA-ET.

#### **5.4 Effect of Thiol Concentration on Chalcogen Dissolution**

Unlike common single-component solvents like water or acetonitrile, the amine-thiol solvent system is not just a solvent: it is also a reactant. In this solvent system, a proton is transferred from the thiol to the amine, resulting in an ionic liquid.<sup>34,29</sup> The formation of S-Se and S-Te bonds (as demonstrated in sections 5.3.1 and 5.3.2) in these solvent systems illustrates that the solvent itself is an important reactant and is therefore directly responsible for the Se and Te dissolution. Therefore, we hypothesized that if the solvent itself is a reactant, varying the concentration of one of the solvent components may directly affect the dissolution of the chalcogens we studied.

### 5.4.1 Effect of Thiol Concentration on Selenium Dissolution

In section 5.3.1, we showed that Se in BA-ET tends to form small Se clusters while Se in EN-ET tends to form RSSe compounds. While all of the data from our Raman, NMR, XAS, and ESI-MS/MS agreed well with each other, our data did not agree well with previous reports for Se in diamine-monothiol solutions, even though several of the analytical techniques were nearly identical.<sup>20</sup> We hypothesized that the difference resulted from the relative amount of Se and thiol used in the previous report compared to our experiments. To further investigate how the ratio of thiol to Se affects Se dissolution, we prepared a series of several solutions with varying thiol to Se ratios in both BA-ET and EN-ET and analyzed them as previously described.

While previous Se samples were made at a concentration of 0.1 or 0.01 M, we increased this concentration to 1.25 M for the following experiments. This was done to increase the signal intensity of the Se and increase reproducibility of the measurements. A total of eight samples were prepared: four samples in BA-ET and four samples in EN-ET. The ET:Se ratios prepared were 0.3, 0.6, 1.5, and 4.0. For these samples, the amine was always in excess of the thiol. Therefore, theoretically, all of the thiols in solution should have been in a deprotonated form and an equal mol ratio of amine (amine:thiol of 1:1 for BA-ET and 2:1 for EN-ET) would be protonated. When comparing the results for these samples to the previous results, the previous results in 1:1 (v/v) amine:thiol are described as “excess thiol” samples. The samples created here with an ET:Se ratio of 0.3 are described as “least thiol.” The set of BA-ET samples will be described first.

The first test on the BA-ET samples was Raman spectroscopy. In the previously analyzed excess thiol sample, three relatively low-intensity peaks between 225-300  $\text{cm}^{-1}$  were observed and were all identified as Se-Se bonds, with the peak at 240  $\text{cm}^{-1}$  corresponding to trigonal crystalline Se and the other two peaks to either monoclinic, orthorhombic, or amorphous Se. Three major trends were observed when analyzing the new samples. First, as the ratio of ET:Se decreased, the intensity of the Se-Se bond peaks dramatically increased. Since the amount of Se in the samples was held constant, this increase in Se-Se bond intensity suggests that at low thiol concentrations, more Se-Se bonds exist and that these Se-Se bonds are broken as more thiol is added. Second, the previously observed peak at 242  $\text{cm}^{-1}$  split into two different peaks at low thiol concentrations: 236 and 248  $\text{cm}^{-1}$ , with the 236  $\text{cm}^{-1}$  peak more intense at lower thiol concentrations. This suggests that at low thiol concentrations, Se remains in its trigonal crystal structure in solution. As more thiol is added, the Se begins to transition to orthorhombic, monoclinic, or amorphous structure.

The final trend observed was that at low thiol concentrations, S-Se bonds were observed in the sample. This suggests that at low thiol concentrations, S-Se bonds form, but that these bonds are broken as additional thiol is added. The reason for this is still unclear and requires further study.

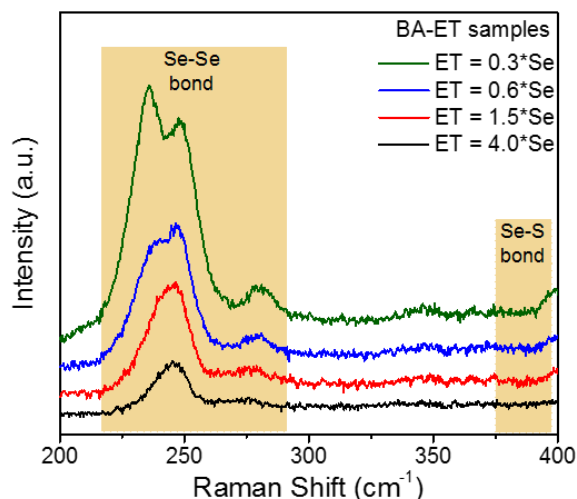


Figure 5.13 Raman spectra of Se in BA-ET at four different ET:Se mol ratios. The regions for Se-Se bonds and for S-Se bonds are darkened and labeled.

The next technique to characterize the Se in BA-ET solution series was XAS. To simplify the data collection, only the least thiol sample was analyzed. Ultimately, not observable difference in the types of bonds was noted between the excess and least thiol samples: only Se-Se bonds were observed. However, the EXAFS data did show some slight variations in average Se coordination number. In excess thiol, the average coordination number was 1.6; in the least thiol sample, the average coordination number was 1.8. This suggests that Se coordination decreases as the thiol concentration increases. Since Se exists mostly as long chains, a larger average coordination number means a longer chain. This is because, in a chain of Se atoms, each terminal Se has a coordination number of one while the inner Se atoms have a coordination number of two. The longer the chain, the average coordination number will approach two. A chain of only three Se atoms would have a coordination number of 1.5. Therefore, the long Se chains observed in the least thiol sample break into smaller chains as more thiol is added.

The next analysis technique used was  $^1\text{H}$  NMR. The most significant difference noted in the four sample was the amount of diethyl disulfide formed. As the thiol concentration increased, the

relative amount of diethyl disulfide increased too. However, the increase stopped once the ET:Se mol ratio reached 1.5, and neither the sample with ET:Se ratio of 4 nor the excess thiol sample had additional diethyl disulfide.

The final analysis technique used was (-)ESI-MS/MS. For the mass spectrometry experiments, only the least thiol sample (ET:Se mol ratio of 0.3) was analyzed and then compared to the excess thiol sample. Two major differences were noted between the two samples. First, both samples had abundant  $\text{HSe}_x^-$  ions; however, the relative abundance of each of the ions was vastly different. In the excess thiol sample, the  $\text{HSe}_x^-$  ions with the greatest signal intensity (and therefore relative abundance) had two to four Se atoms, with two being the most abundant overall. In the least thiol sample, the greatest intensity  $\text{HSe}_x^-$  ions had two to six Se atoms, with three being the most abundant. This observation clearly corroborates the XAS data, which showed that as the thiol concentration increases, the Se chains decrease in size. The second observation was the appearance of  $\text{C}_2\text{H}_5\text{SSe}_x^-$  ions in the least thiol samples. These ions were not present in the excess thiol sample. This finding lends further support to the appearance of S-Se bonds observed in the Raman data at the lower thiol concentration samples. For these ions, one to four Se atoms were observed.

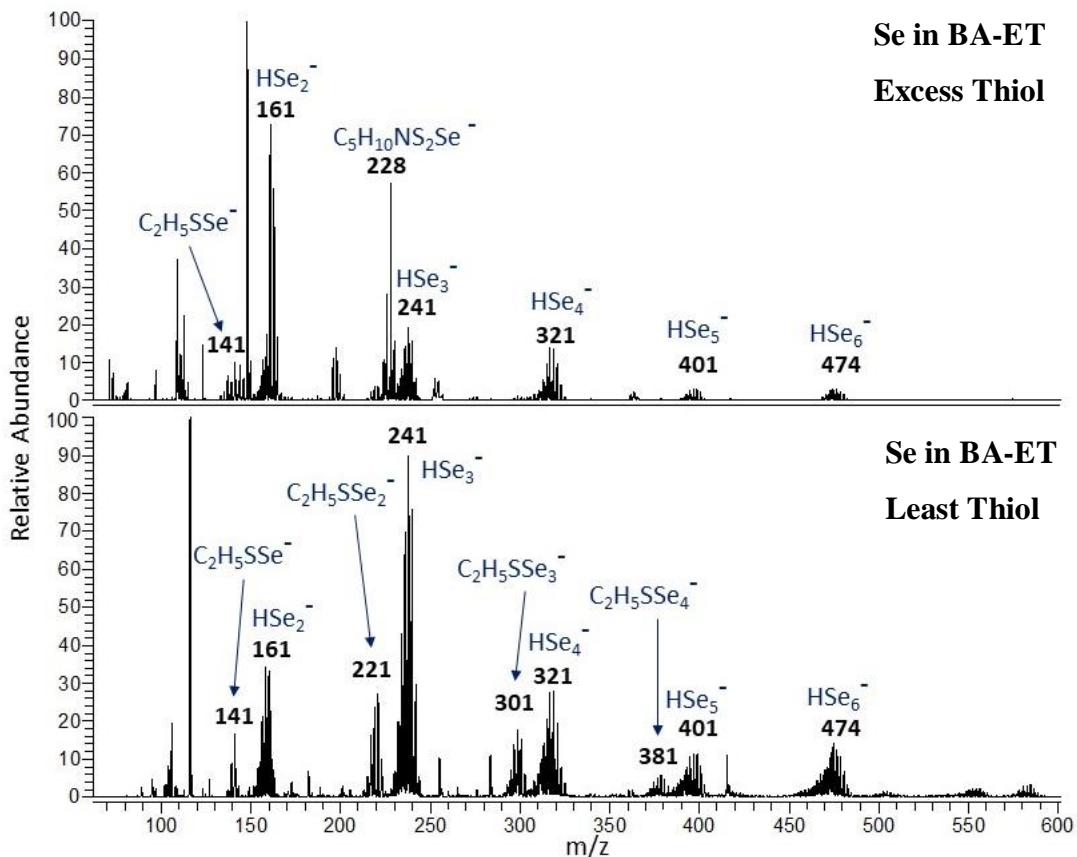


Figure 5.14 (-)ESI-MS spectra of Se in BA-ET. The top spectrum is the excess thiol sample while the bottom spectrum is the least thiol sample. Labeled masses are for the monoisotopic mass of the corresponding assignment. Unlabeled peaks either contain no selenium or were not successfully identified.

Finally, a scheme for the dissolution was produced from the various data collected. This scheme is presented below. Previously, I hypothesized that the addition of Se acts as an electron acceptor in the ionic solvent, accepting electrons from deprotonated thiols to form a neutral species which can then react with an  $RS^-$  ion to form a disulfide. Theoretically, at the lowest thiol concentrations, all thiols are deprotonated and exist as negatively charged ions unable to react with each other and produce diethyl disulfide. As the  $RS^-$  ions react with Se to break up the chains, electrons are transferred to the Se and the disulfide can form. The Raman data showed evidence of this S-Se bond formation at low thiol concentrations. As thiol concentration increases, the Se chains continue to get smaller, as shown in the XAS data. As the Se chains continue to break into smaller chains and clusters, the potential for disulfide formation increases, as shown in the NMR data. However, the mass spectrometry data clearly showed that Se chains of only two to four Se

atoms are favored at high thiol concentrations, suggesting that at a certain point, the Se chains will no longer be broken into smaller pieces. At this point, addition of additional thiol won't break the Se chains anymore and additional disulfide formation won't be possible. This phenomenon was observed in the NMR data, with additional disulfide formation stopping at a ET:Se mol ratio of 1.5.

Next, we performed the same testing procedure on the four thiol concentration samples in EN-ET. The first analysis technique used was Raman spectroscopy. In the previously analyzed excess thiol sample, there was no evidence for Se-Se bonds and only one small feature in the spectrum that was assigned to S-Se bonds. In the new samples, major differences were observed. In the new samples with lower thiol concentrations, Se-Se bonds were observed. As seen in the BA-ET samples, the Se-Se bonds were much higher intensity at lower thiol concentrations. Also in line with the BA-ET samples, the EN-ET Raman spectra showed a transition from more trigonal structures at low thiol concentrations to more orthorhombic, monoclinic, or amorphous structures at higher thiol concentrations. However, the opposite trend was observed in the S-Se bonds in the samples: as the thiol concentration increased, so too did the S-Se bond intensity. This was the opposite trend observed in the BA-ET samples, which only had S-Se bonds at low thiol concentrations. Ultimately, the Raman data suggest that at low thiol concentrations, Se exists primarily in its trigonal chain-like structure. As the thiol concentration increases, the Se-Se bonds are replaced with S-Se bonds. The remaining Se-Se bonds are no longer primarily in the trigonal structure.

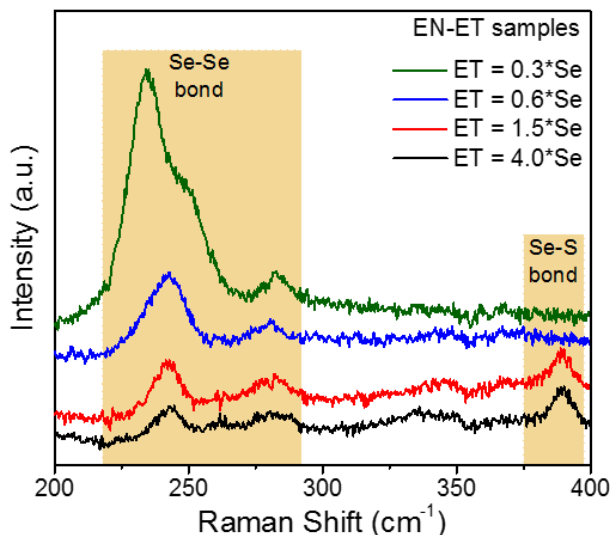


Figure 5.15 Raman spectra of Se in BA-ET at four different ET:Se mol ratios. The regions for Se-Se bonds and for S-Se bonds are darkened and labeled.

The next techniques used on the EN-ET samples were  $^1\text{H}$  NMR and XAS. For the NMR, few differences were noted in the four samples when compared to the excess thiol sample. All samples showed dimethyl disulfide formation, but the clear increase in diethyl disulfide concentration seen in the BA-ET samples was not observed. For the XAS analysis, only the least thiol sample was analyzed and then compared to the excess thiol sample. In the excess thiol, we had only observed S-Se bonds with an average Se coordination number of 0.8. In the least thiol sample, there was no evidence of S-Se bonding, but clear evidence of Se-Se bonds with an average Se coordination number of 1.1. This finding corroborates the Raman data for these samples: as thiol concentration increases, Se clusters and chains are replaced by S-Se bonds with an average of one to two Se atoms (coordination number of approximately 1 in the excess thiol sample).

Finally, mass spectrometry was used to identify the types of ions in the solution. As with the BA-ET mass spectrometry experiments, only the least thiol sample was analyzed and then compared to the excess thiol sample. The two spectra were vastly different. In the excess thiol sample, the most predominant peak was  $\text{C}_2\text{H}_5\text{SSe}^-$ . Very few other Se-containing ions were observed. In the least thiol sample, however, at least eight different Se-containing ions were observed. Of these ions,  $\text{HSe}_x^-$  ions were the most abundant, with two to four Se atoms the most common cluster size. Ion containing up to six Se atoms were observed. Additionally, both  $\text{C}_2\text{H}_5\text{SSe}^-$  and  $\text{C}_2\text{H}_5\text{SSe}_2^-$  were observed, with  $\text{C}_2\text{H}_5\text{SSe}_2^-$  the more abundant of the two. This data

clearly supports the Raman and XAS data, showing that at low thiol concentrations, relatively large Se chains are still in solution as are S-Se species. As the thiol concentration increases, the Se chains are broken and replaced almost entirely with  $C_2H_5SSe^-$ .

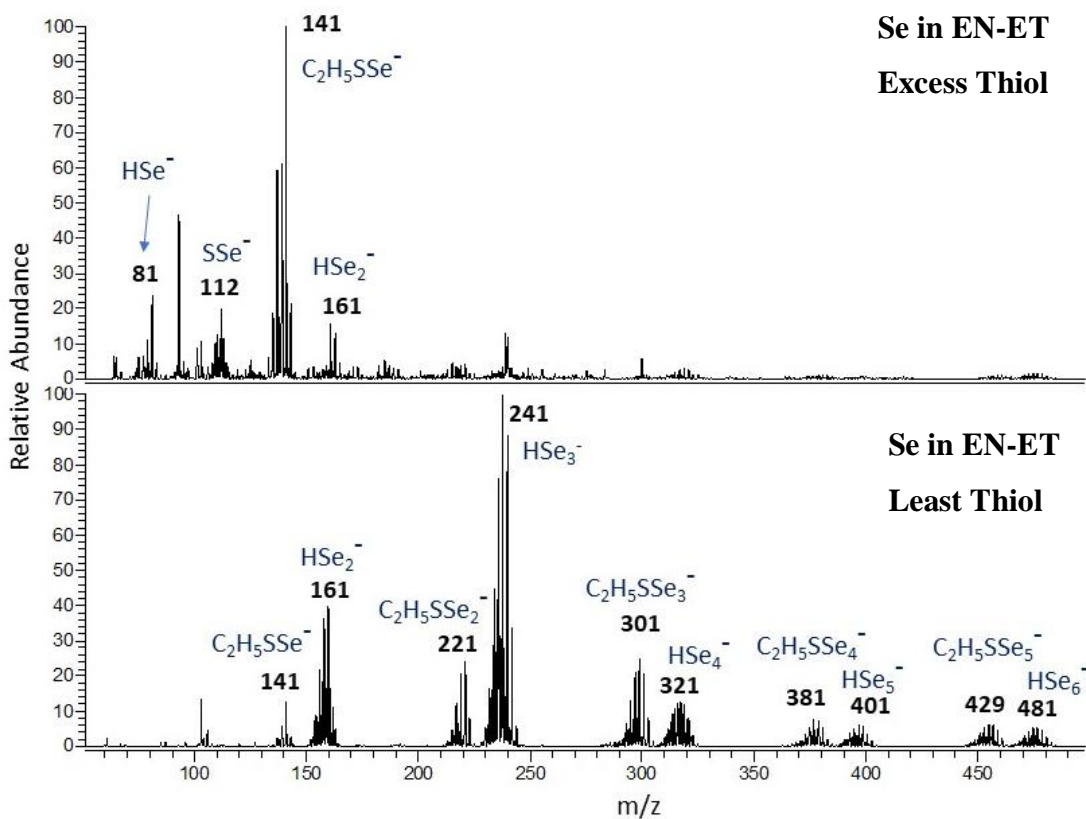


Figure 5.16 (-)ESI-MS spectra of Se in EN-ET. The top spectrum is the excess thiol sample while the bottom spectrum is the least thiol sample. Labeled masses are for the monoisotopic mass of the corresponding assignment. Unlabeled peaks either contain no selenium or were not successfully identified.

Finally, we developed a scheme for Se dissolution in the EN-ET solvent system. In this scheme, the initial deprotonated thiolate ions act as nucleophiles, reacting with Se clusters and forming both  $C_2H_5SSe_x$  species and  $Se_x^-$  ions. At first, the  $Se_x^-$  ions exist as fairly large chains of up to at least six Se atoms. During this process, some diethyl disulfide is formed. As additional thiol is added to the solution, the additional thiolate ions primarily react to form  $C_2H_5SSe_x$  species, breaking up the Se chains until practically no Se chains remain in solution. The difference between this dissolution scheme and the BA-ET scheme may be a result of the differing amine basicity and nucleophilic interactions with the diammonium cation compared to the monoammonium cation.

Table 5.4 Elemental composition of ions detected using (-) ESI-MS for Se solutions in BA-ET and EN-ET with minimum thiol used for dissolution. For some ions, the high resolution MS signal was too low for accurate calculation of the error or calculation of the m/z with high accuracy (more than two decimal points). Assignments for these ions were based on low-resolution mass and isotopic distributions. These ions are marked in the table with \*. All m/z reported are for the monoisotopic mass.

<b>Se in BA-ET with minimum ET</b>		
<i>m/z</i>	<b>Elemental Composition</b>	<b>Error from expected mass (+/- ppm)</b>
105.92037	CNSe	11.73
116.07191	C <sub>3</sub> H <sub>10</sub> NO <sub>2</sub>	11.24
140.92850	C <sub>2</sub> H <sub>5</sub> SSe	9.59
159.83391	Se <sub>2</sub>	8.98
220.84506	C <sub>2</sub> H <sub>5</sub> SSe <sub>2</sub>	6.20
240.75812	HSe <sub>3</sub>	6.69
300.76171	C <sub>2</sub> H <sub>5</sub> SSe <sub>3</sub>	5.14
320.67536	HSe <sub>4</sub>	5.66
400.59350	HSe <sub>5</sub>	8.35
480.58*	HSe <sub>6</sub>	Assigned based on isotopic patterns

<b>Se in EN-ET with minimum ET</b>		
<i>m/z</i>	<b>Elemental Composition</b>	<b>Error from expected mass (+/- ppm)</b>
85.047079	C <sub>3</sub> H <sub>5</sub> ON <sub>2</sub>	13.53
108.99644	C <sub>2</sub> H <sub>5</sub> O <sub>3</sub> S	9.62
140.92818	C <sub>2</sub> H <sub>5</sub> SSe	7.17
160.84161	HSe <sub>2</sub>	8.02
220.84452	C <sub>2</sub> H <sub>5</sub> SSe <sub>2</sub>	3.75
240.75800	HSe <sub>3</sub>	4.81
300.76146	C <sub>2</sub> H <sub>5</sub> SSe <sub>3</sub>	4.15
319.66712	Se <sub>4</sub> /HSe <sub>4</sub>	4.95
400.59241	HSe <sub>5</sub>	6.30
480.58*	HSe <sub>6</sub>	Assigned based on isotopic patterns

#### 5.4.2 Effect of Thiol Concentration on Te Dissolution

For this study, we attempted to reproduce the selenium thiol concentration studies. However, our attempts were thwarted by the low solubility of Te. A 0.5 M Te in EN-ET solution has an ET:Te mol ratio of four. This was the lowest amount of thiol that we could add while still dissolving the Te. When we added additional thiol to this solution and analyzed the resulting

solutions, we saw no observable differences. The solution was simply diluted and had no evidence for a change in Te bonding.

### 5.4.3 Effect of Thiol Concentration on Se Te Codissolution

Finally, we studied the effect of thiol concentration on the codissolution of Se and Te. To produce these samples, a Se:Te ratio of 3:2 at a total chalcogen concentration of 10 mM was used. This data is preliminary and was intended for further exploration, so only (-) ESI MS/MS was used to characterize the samples. The Se and Te in 1:1 (v/v) amine: thiol samples are referred to as the “excess thiol” samples. The “least thiol” samples were made at a thiol: chalcogen ratio of 0.3: no other ratios were prepared.

As previously discussed, Se and Te dissolved together in BA-ET with excess thiol exhibited a large number of species in solution, but that nearly all of these ions were of the form  $\text{Se}_x\text{Te}_y$ , with  $x \geq y$ . Almost no other kinds of Se or Te-containing ions were observed. The mass spectrum of the least thiol sample was quite different. While the least thiol sample still contained  $\text{Se}_x\text{Te}_y$  ions, there were only two of them:  $\text{Se}_2\text{Te}$  and  $\text{HSe}_3\text{Te}$ . Additionally, a substantial abundance of  $\text{CNSe}$  and  $\text{CNTe}$  ions were observed, as was  $\text{HO}_3\text{Te}$ . Since ozone addition and other reactions are known to occur in ethanethiol solutions (see Chapter 4), it is possible that the formation of these three ions are due to ESI-induced reactions and ozone addition. For this solution, an unusually large amount of visual plasma was observed during data collection, which would suggest that the data collected for this sample is not wholly representative of the species found in solution.

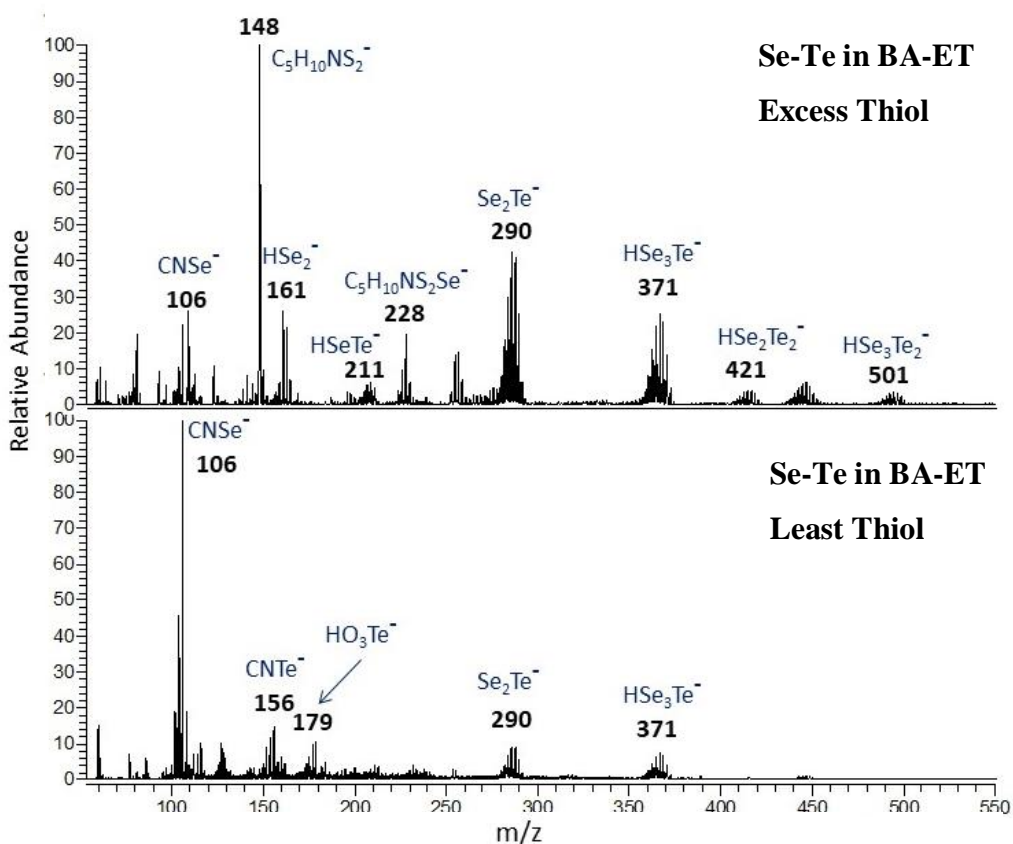


Figure 5.17 (-)ESI-MS spectra of SeTe in BA-ET. The top spectrum is the excess thiol sample while the bottom spectrum is the least thiol sample. Labeled masses are for the monoisotopic mass of the corresponding assignment. Unlabeled peaks either contain no selenium or were not successfully identified.

Table 5.5 Elemental composition of ions detected using (-) ESI-MS for Se-Te solutions in BA-ET with a thiol:Se molar ratio of 0.3. All  $m/z$  reported are for the monoisotopic mass.

<b>Se-Te in BA-ET (Least thiol)</b>		
<i>m/z</i>	<b>Elemental Composition</b>	<b>Error from expected mass (+/- ppm)</b>
105.92037	CNSe	12.49
155.91014	CNTe	8.92
178.89963	HO <sub>3</sub> Te	7.75
289.74043	Se <sub>2</sub> Te	5.91
370.66482	HSe <sub>3</sub> Te	4.74

For Se and Te dissolved in EN-ET, however, much more consistent and reproducible mass spectrometry data was obtained. As previously discussed, with excess thiol, this sample exhibited many different ions, including  $\text{RSSe}_x$ ,  $\text{RSTe}_y$ ,  $\text{RSSe}_x\text{Te}_y$ , and  $\text{Se}_x\text{Te}_y$ . For the  $\text{RSSe}_x\text{Te}_y$ , and  $\text{Se}_x\text{Te}_y$  ions, the number of Se atoms was always greater than or equal to the number of Te atoms. In this solution, both the RS-containing ions and the lone metal clusters were almost equal in total abundance. Additionally,  $\text{Te}_2^-$  was observed: the only instance in the spectrum where Te was observed without any additional Se or a sulfur or CN ligand. Unlike the Se and Te in BA-ET, the least thiol sample in EN-ET had strikingly similar ions present; the main difference was in the relative abundance of many of the ions. In the least thiol sample, larger SeTe clusters, both with and without thiol ligands, were observed in the spectrum and at higher relative abundances. This suggests that dissolution begins by breaking down the Se and Te chains into clusters, and that this process continues as additional thiol is added until cluster sizes are relatively small. Additionally,  $\text{Se}_x$  clusters are in much higher abundance in the least thiol sample, most notably  $\text{HSe}_2$  and  $\text{Se}_3$ . This suggests that when Se and Te first begin to dissolve, the Se dissolves in higher abundance first. Since we hypothesized in section 5.3.3 that the formation of  $\text{Se}_x$  nucleophiles in solution is primarily responsible for the dissolution of Te, the large abundance of  $\text{Se}_2$  and  $\text{Se}_3$  ions at low thiol concentrations makes sense. Finally, the last major observation was the disappearance of the  $\text{Te}_2$  and  $\text{C}_2\text{H}_5\text{STe}_x$  ions. Again, this finding fits well into our broader understanding of Se and Te codissolution. The Se is preferentially dissolved, and only when there is enough thiol in solution can  $\text{Te}_x$  and  $\text{C}_2\text{H}_5\text{STe}_x$  species be formed in solution.

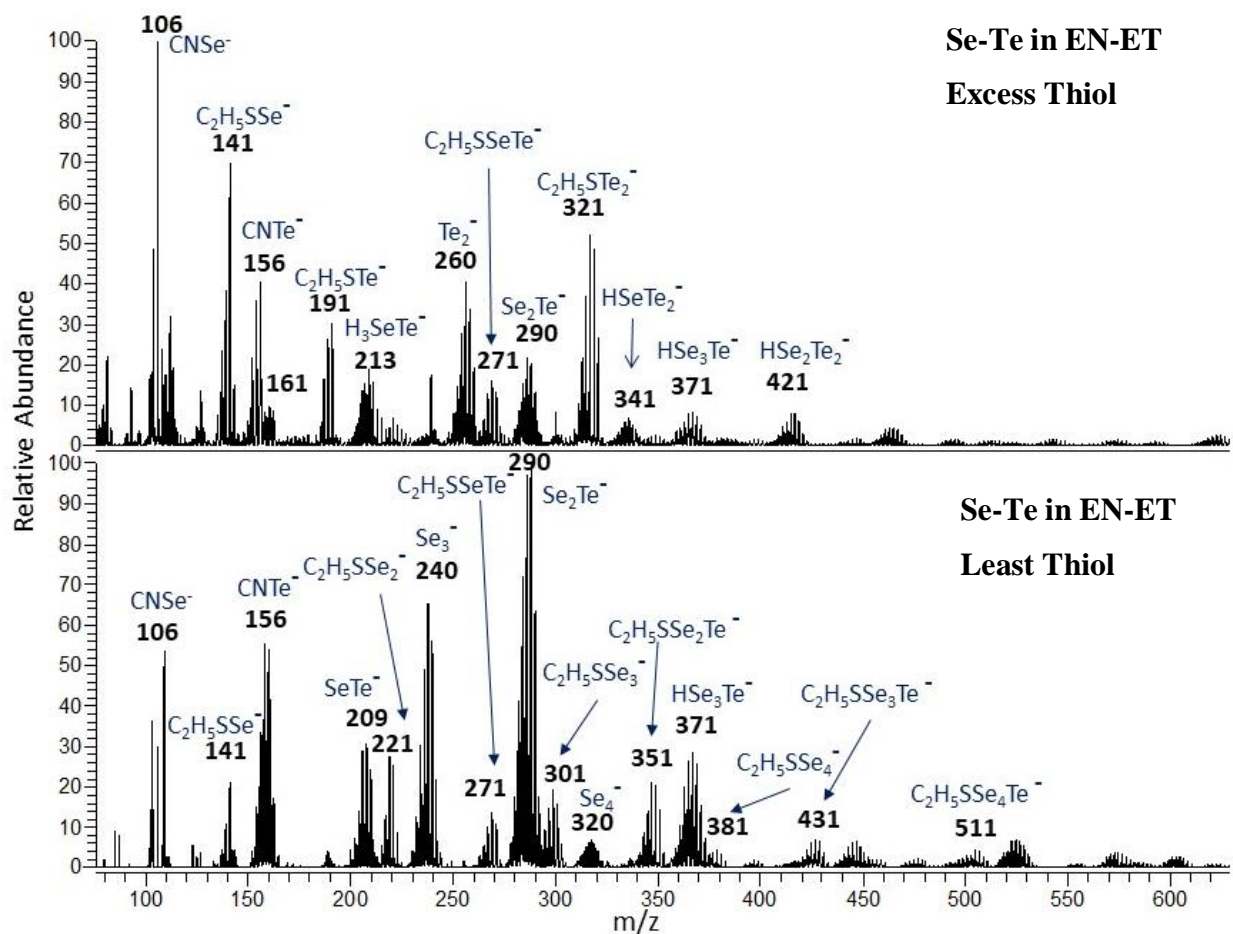


Figure 5.18 (-)ESI-MS spectra of SeTe in EN-ET at two different concentrations of thiol. The top spectrum is the excess thiol sample while the bottom spectrum is the least thiol sample. Labeled masses are for the monoisotopic mass of the corresponding assignment. Unlabeled peaks either contain no selenium or were not successfully identified.

Table 5.6 Elemental composition of ions detected using (-) ESI-MS for Se-Te solutions in BA-ET with a thiol:Se molar ratio of 0.3. For one ion, the high resolution MS signal was too low for accurate calculation of the error or calculation of the  $m/z$  with high accuracy. Assignment for this ion was based on low-resolution mass and isotopic distributions. These ions are marked in the table with \*. All  $m/z$  reported are for the monoisotopic mass.

<b>Se-Te in EN-ET</b>		
<b><math>m/z</math></b>	<b>Elemental Composition</b>	<b>Error from expected mass (+/- ppm)</b>
105.92004	CNSe	9.37
140.92810	C <sub>2</sub> H <sub>5</sub> SSe	6.60
155.90941	CNTe	4.24
209.82277	SeTe	2.73
220.84442	C <sub>2</sub> H <sub>5</sub> SSe <sub>2</sub>	3.30
239.74989	Se <sub>3</sub>	3.64
270.83386	C <sub>2</sub> H <sub>5</sub> SSeTe	1.73
289.73900	Se <sub>2</sub> Te	0.97
300.76086	C <sub>2</sub> H <sub>5</sub> SSe <sub>3</sub>	2.15
319.66688	Se <sub>4</sub>	4.20
350.75052	C <sub>2</sub> H <sub>5</sub> SSe <sub>2</sub> Te	1.73
370.66423	HSe <sub>3</sub> Te	3.14
380.67779	C <sub>2</sub> H <sub>5</sub> SSe <sub>4</sub>	2.77
430.66804	C <sub>2</sub> H <sub>5</sub> SSe <sub>3</sub> Te	3.73
511*	C <sub>2</sub> H <sub>5</sub> SSe <sub>4</sub> Te	Assigned based on isotopic pattern

## 5.5 Using New Understanding to Guide Alloy Synthesis

Previously, researchers at Purdue noted that lead chalcogenide nanoparticle synthesis appeared to be impacted by changing from monoamines to diamines (21). Our new research provides a possible lens through which to interpret these previously-observed differences. It also presented an opportunity to test whether our new understanding could predict the behavior of PbSeTe nanoparticle alloy formation in different solvents. Our findings concluded that Se and Te dissolved in butylamine-ethanethiol solutions formed mostly Se<sub>x</sub>Te<sub>y</sub> species with a limited range of cluster sizes. However, Se and Te in ethylenediamine-ethanethiol produced many different species, including RSSe<sub>x</sub>, RSTe<sub>x</sub>, RSSe<sub>x</sub>Te<sub>y</sub> and Se<sub>x</sub>Te<sub>y</sub>. We hypothesized that the relative uniformity of the species formed in butylamine-ethanethiol solution would produce a Pb alloy with equally uniform properties. We also hypothesized that since numerous different species formed in ethylenediamine-ethanethiol solutions, the resulting Pb alloy would be less uniform and may have a heterogenous composition.

To test our hypothesis, two solutions of Se and Te were used to synthesize PbSeTe nanoparticles. The first solution contained a 4:1 mol ratio of Se:Te dissolved in butylamine-ethanethiol (1:1 by volume) while the second solution contained a 4:1 mol ratio of Se:Te dissolved in ethylenediamine-ethanethiol (1:1 by volume). Each of these solutions was independently reacted with a lead acetate solutions. Each solution precipitated nanoparticles within one minute, which were then washed and analyzed using X-ray diffraction. When measured under the same conditions ( $2\theta$  between  $23-33^\circ$ ), the XRD showed clear differences between the two different sets of nanoparticles. For the butylamine-ethanethiol particles, two peaks could be seen: a PbSe peak and a fairly uniform and homogenous PbSeTe alloy peak. This result was expected: free  $\text{Se}_x$  species were known to form in the butylamine solution, which would lead to the PbSe particles. Additionally, the  $\text{Se}_x\text{Te}_y$  species seen in the butylamine solution were comparatively homogenous, so the single broad peak corresponding to a PbSeTe alloy was expected. XRD of the ethylenediamine solution particles showed three peaks: a PbSe peak, a Se rich PbSeTe alloy peak, and a Te rich PbSeTe alloy peak. These results were also expected. In the ethylenediamine solution, clusters of  $\text{Se}_x$ ,  $\text{Te}_x$ , and  $\text{Se}_x\text{Te}_y$  were observed, with the  $\text{Se}_x\text{Te}_y$  clusters exhibiting a much wider range of compositions compared to the butylamine solution. Therefore, the alloy formed was not nearly as homogenous, showing both Se and Te rich alloy formation.

## 5.6 Conclusions

In this chapter, we investigated the dissolution mechanism and species formation of selenium and tellurium in amine-thiol solvent systems. To do this, a combination of mass spectrometry, Raman spectroscopy, X-ray absorption, and NMR spectroscopy were used to analyze a variety of solutions. From the data collected, we found that the Se and Te ions formed in solution can vary significantly based on both the amine-thiol solvent system used and the relative concentration of thiol in the solution. In monoamine-monothiol solvents, Se exists in numerous configurations, not just the monoclinic  $\text{Se}_8$  rings previously observed. We observed that the addition of Se to the monoamine-monothiol solvent facilitated the formation of dialkyl disulfide. As the thiol concentration in this solution increases, thiolate ions transfer electrons to Se chains, breaking them into smaller chains and clusters until a minimum cluster size of two to four Se atoms is reached. In diamine-monothiol solvents, the thiolate in solution both breaks the Se chains into smaller clusters and reacts with sufficiently small Se clusters to form thiolate ligands. As the thiol

concentration is increased, these small Se clusters with thiolate ligands are favored and nearly no large Se clusters are left. The difference in the behavior of these two solvent systems is hypothesized to be due to the difference in basicity between the monoamine and diamine counterions.

In diamine-monothiol solutions, Te was found to form relatively small Te clusters with thiolate ligands. Perhaps due to the low solubility of Te in these solutions, very small concentrations of thiol could not dissolve the Te and larger concentrations of thiol only diluted the sample. However, co-dissolving Se and Te together resulted in significantly different solutions. In diamine-monothiol, Se and Te first forms Se ions and Se clusters with thiolate ligands. When enough of these Se nucleophiles are in solution, Se-Te-thiolate complexes are formed. As thiol concentration increases, the Se chains are broken into smaller Se and Se-Te clusters. These ions are small enough to remain stable in solution without the thiolate ligand. With excess thiol in solution, there is enough thiol to facilitate the formation of very small Te clusters. In monoamine-monothiol, the thiolate ligands remain on the Se Te complexes, even at large thiol concentrations. The insolubility of Te in monoamine-monothiol solutions likely causes this difference.

Finally, we used the findings from our Se and Te experiments to tune the synthesis of a PbSeTe material. We showed that the relative uniformity of the Se-Te species formed in butylamine-ethanethiol solution resulted in a Pb alloy with relatively uniform properties and composition while the numerous different kinds of Se and Te species in ethylenediamine-ethanethiol resulted in a less homogenous Pb alloy with heterogeneous composition. It is our belief that understanding how chalcogens dissolve in and react with amine-thiol solvent systems can allow other researchers to similarly tune the synthesis of other metal chalcogenide materials and ultimately better control the properties of the metal chalcogenides needed for next-generation photovoltaic cells and other thermoelectric devices.

## 5.7 References

1. Reinders, A.; van Sark, W.; Verlinden, P. Introduction to Photovoltaics *in* Photovoltaic Solar Energy: From Fundamentals to Applications (ed. Reinders, A.; Verlinden, P.; van Sark, W.; Freundlich, A. 2017, John Wiley and Sons, Ltd. Chichester, UK. pp 3-11

2. IPCC (2013) Summary for Policymakers. In *Climate Change 2013: The Physical Science Basis. Contribution of Working Group I to the Fifth Assessment Report of the Intergovernmental Panel on Climate Change* (eds Stocker, T.F.; Qin, D.; Plattner, G.K.). Cambridge University Press, Cambridge.
3. European Commission (2011) Energy Roadmap 2050. *Communication from the Commission to the European Parliament, the Council, the European Economic and Social Committee and the Committee of the Regions*, COM/2011/0885 final. EC, Brussels.
4. Greenpeace (2015) *Energy Revolution*, 5<sup>th</sup> edn, *2015 World Energy Scenario*, Greenpeace International, Global Wind Energy Council, Solar Power Europe (eds Teske, S.; Sawyer, S.; Schäfer, O.). Greenpeace, New York.
5. Green, M.A.; Emery, K.; Hishikawa, Y. *et al.* (2016) Solar Cell Efficiency Tables version 48 *Progress in Photovoltaics: Research and Applications*, **24**, 905-913.
6. Siebentritt, S. Basics of Chalcogenide Thin Film Solar Cells. In *Photovoltaic Solar Energy: From Fundamentals to Applications* (ed. Reinders, A.; Verlinden, P.; van Sark, W.; Freundlich, A. 2017, John Wiley and Sons, Ltd. Chichester, UK. pp 169-178.
7. Basol, B.M. (1992) Processing High Efficiency CdTe Solar Cells. *International Journal Solar Energy*, **12**, 25-35.
8. García de Arquer, F. P.; Armin, A.; Meredith, P.; Sargent, E. H. Solution-Processed Semiconductors for Next-Generation Photodetectors. *Nat. Rev. Mater.* **2017**, 2 (3), 16100.
9. Abbel, R.; Galagan, Y.; Groen, P. Roll-to-Roll Fabrication of Solution Processed Electronics. *Adv. Eng. Mater.* **2018**, 20 (8), 1701190.
10. Habas, S. E.; Platt, H. A. S.; van Hest, M. F. A. M.; Ginley, D. S. Low-Cost Inorganic Solar Cells: From Ink To Printed Device. *Chem. Rev.* **2010**, 110 (11), 6571–6594.
11. Azimi, H.; Brabec, C. J. Towards Low-Cost, Environmentally Friendly Printed Chalcopyrite and Kesterite Solar Cells. *Energy Environ. Sci.* **2014**, 7, 1829–1849.
12. Uhl, A. R.; Katahara, J. K.; Hillhouse, H. W. Molecular-Ink Route to 13.0% Efficient Low-Bandgap CuIn(S,Se)<sub>2</sub> and 14.7% Efficient Cu(In,Ga)(S,Se)<sub>2</sub> Solar Cells. *Energy Environ. Sci.* **2016**, 9 (1), 130–134.
13. Yuan, M.; Mitzi, D. B. Solvent Properties of Hydrazine in the Preparation of Metal Chalcogenide Bulk Materials and Films. *Dalt. Trans.* **2009**, 31 (31), 6078.
14. Murray, C. B.; Norris, D. J.; Bawendi, M. G. Synthesis and Characterization of Nearly Monodisperse CdE (E = Sulfur, Selenium, Tellurium) Semiconductor Nanocrystallites. *J. Am. Chem. Soc.* **1993**, 115 (19), 8706–8715.

15. Peng, X.; Wickham, J.; Alivisatos, A. P. Kinetics of II-VI and III-V Colloidal Semiconductor Nanocrystal Growth: “Focusing” of Size Distributions. *J. Am. Chem. Soc.* **1998**, *120* (21), 5343–5344.
16. Klayman, D. L.; Griffin, T. S. Reaction of Selenium with Sodium Borohydride in Protic Solvents. A Facile Method for the Introduction of Selenium into Organic Molecules. *J. Am. Chem. Soc.* **1973**, *95* (1), 197–199.
17. Webber, D. H.; Brutchey, R. L. Alkahest for V<sub>2</sub>VI<sub>3</sub> Chalcogenides: Dissolution of Nine Bulk Semiconductors in a Diamine-Dithiol Solvent Mixture. *J. Am. Chem. Soc.* **2013**, *135* (42), 15722–15725.
18. Zhang, R.; Szczepaniak, S. M.; Carter, N. J.; Handwerker, C. A.; Agrawal, R. A Versatile Solution Route to Efficient Cu<sub>2</sub>ZnSn(S,Se)<sub>4</sub> Thin-Film Solar Cells. *Chem. Mater.* **2015**, *27* (6), 2114–2120.
19. Zhang, R.; Cho, S.; Lim, D. G.; Hu, X.; Stach, E. A.; Handwerker, C. A.; Agrawal, R. Metal–metal Chalcogenide Molecular Precursors to Binary, Ternary, and Quaternary Metal Chalcogenide Thin Films for Electronic Devices. *Chem. Commun.* **2016**, *52*, 5007–5010.
20. Webber, D. H.; Buckley, J. J.; Antunez, P. D.; Brutchey, R. L. Facile Dissolution of Selenium and Tellurium in a Thiol–amine Solvent Mixture under Ambient Conditions. *Chem. Sci.* **2014**, *5* (6), 2498.
21. McCarthy, C. L.; Brutchey, R. L. Solution Processing of Chalcogenide Materials Using Thiol–amine “alkahest” Solvent Systems. *Chem. Commun.* **2017**, *53* (36), 4888–4902.
22. Zhao, X.; Lu, M.; Koeper, M.; Agrawal, R. Solution-Processed Sulfur Depleted Cu(In,Ga)Se<sub>2</sub> Solar Cells Synthesized from a Monoamine-Dithiol Solvent Mixture. *J. Mater. Chem. A* **2016**, *4* (19), 7390–7397.
23. Yu, X.; Cheng, S.; Yan, Q.; Yu, J.; Qiu, W.; Zhou, Z.; Zheng, Q.; Wu, S. Efficient (Cu<sub>1-x</sub>Ag<sub>x</sub>)<sub>2</sub>ZnSn(S,Se)<sub>4</sub> Solar Cells on Flexible Mo Foils. *RSC Adv.* **2018**, *8* (49), 27686–27694.
24. Miskin, C. K.; Dubois-Camacho, A.; Reese, M. O.; Agrawal, R. A Direct Solution Deposition Approach to CdTe Thin Films. *J. Mater. Chem. C* **2016**, *4* (39), 9167–9171.
25. McCarthy, C. L.; Brutchey, R. L. Solution Deposited Cu<sub>2</sub>BaSnS<sub>4-x</sub>Se<sub>x</sub> from a Thiol-Amine Solvent Mixture. *Chem. Mater.* **2018**, *30* (2), 304–308.
26. Miskin, C. K.; Deshmukh, S. D.; Vasiraju, V.; Bock, K.; Mittal, G.; Dubois-camacho, A.; Vaddiraju, S.; Agrawal, R. Lead Chalcogenide Nanoparticles and Their Size-Controlled Self-Assemblies for Thermoelectric and Photovoltaic Applications. *ACS Appl. Nano Mater.* **2019**, *2*, 1242–1252.
27. Deshmukh, S. D.; Ellis, R. G.; Sutandar, D. S.; Rokke, D. J.; Agrawal, R. Versatile Colloidal Syntheses of Metal Chalcogenide Nanoparticles from Elemental Precursors Using Amine-Thiol Chemistry. *Submitted*.

28. Liu, Y.; Yao, D.; Shen, L.; Zhang, H.; Zhang, X.; Yang, B. Alkylthiol-Enabled Se Powder Dissolution in Oleylamine at Room Temperature for the Phosphine-Free Synthesis of Copper-Based Quaternary Selenide Nanocrystals. *J. Am. Chem. Soc.* **2012**, *134* (17), 7207–7210.
29. Walker, B. C.; Agrawal, R. Contamination-Free Solutions of Selenium in Amines for Nanoparticle Synthesis. *Chem. Commun.* **2014**, *50* (61), 8331.
30. Noufi, R.; Axton, R.; Herrington, C.; Deb, S. Electronic Properties Versus Composition of Thin Film CuInSe<sub>2</sub>. *Applied Physics Letter*, **1984**, *45*, 301-313.
31. Schock, H.; *Properties of Chalcopyrite-based Materials and Film Deposition for Thin-Film Solar Cells.* **2004** Springer, Berlin.
32. Rau, U.; Schock, U.W. **2001** *Cu(In,Ga)Se<sub>2</sub> Solar Cells*. Imperial College Press, London.
33. Murria, P.; Miskin, C. K.; Boyne, R.; Cain, L. T.; Yerabolu, R.; Zhang, R.; Wegener, E. C.; Miller, J. T.; Kenttämäaa, H. I.; Agrawal, R. Speciation of CuCl and CuCl<sub>2</sub> Thiol-Amine Solutions and Characterization of Resulting Films: Implications for Semiconductor Device Fabrication. *Inorg. Chem.* **2017**, *56* (23), 14396–14407.
34. Zhao, X.; Deshmukh, S. D.; Rokke, D. J.; Zhang, G.; Wu, Z.; Miller, J. T.; Agrawal, R. Investigating Chemistry of Metal Dissolution in Amine–Thiol Mixtures and Exploiting It toward Benign Ink Formulation for Metal Chalcogenide Thin Films. *Chem. Mater.* **2019**, *31* (15), 5674–5682.
35. Lucovsky, G.; Mooradian, A.; Taylor, W.; Wright, G. B.; Keezer, R. C. Identification of the Fundamental Vibrational Modes Of Trigonal, Monoclinic and Amorphous Selenium. *Solid State Commun.* **1967**, *5*, 113–117.
36. Alparone, A. Density Functional Theory Raman Spectra of Cyclic Selenium Clusters Se<sub>n</sub> (n=5-12). *Comput. Theor. Chem.* **2012**, *988*, 81–85.
37. Eysel, H. H.; Sunder, S. Homonuclear Bonds in Sulfur-Selenium Mixed Crystals: A Raman Spectroscopic Study. *Inorg. Chem.* **1979**, *18* (9), 2626–2627.
38. Allen, F. H.; Kennard, O.; Watson, D. G.; Brammer, L.; Orpen, A. G.; Taylor, R. Tables of Bond Lengths Determined by X-Ray and Neutron Diffraction. Part 1. Bond Lengths in Organic Compounds. *J. Chem. Soc. Perkin Trans. 2* **1987**, S1–S19.
39. Benamar, A.; Rayane, D.; Melinon, P.; Tribollet, B.; Broyer, M. Comparison between Selenium and Tellurium Clusters. *Zeitschrift für Phys. D Atoms, Mol. Clust.* **1991**, *19* (4), 237–239.
40. Tverjanovich, A.; Rodionov, K.; Bychkov, E. Raman Spectroscopy of Glasses in the As-Te System. *J. Solid State Chem.* **2012**, *190*, 271–276.
41. Brodsky, M. H.; Gambino, R. J.; Smith, J. E.; Yacoby, Y. The Raman Spectrum of Amorphous Tellurium. *Phys. Status Solidi* **1972**, *52* (2), 609–614.

42. Clark, E. R.; Collett, A. J. Preparation, Infrared and Raman Spectra of Some Compounds of Tellurium (II). *J. Chem. Soc. A Inorganic, Phys. Theor.* **1969**, 2129–2130.
43. Hendra, P. J.; Jovic, Z. Infrared and Raman Spectra of Some Complexes between Thiourea and Tellurium (II). *J. Chem. Soc. A Inorganic, Phys. Theor.* **1967**, 735–736.
44. Mendoza-Galván, A.; García-García, E.; Vorobiev, Y. V.; González-Hernández, J. Structural, Optical and Electrical Characterization of Amorphous  $\text{Se}_x\text{Te}_{1-x}$  Thin Film Alloys. *Microelectron. Eng.* **2000**, *51*, 677–687.
45. Tverjanovich, A.; Cuisset, A.; Fontanari, D.; Bychkov, E. Structure of Se–Te Glasses by Raman Spectroscopy and DFT Modeling. *J. Am. Ceram. Soc.* **2018**, *101* (11), 5188–5197.

## VITA

### EDUCATION

Purdue University, West Lafayette, IN

**Doctoral Candidate**

GPA: 3.84

2020

Robert R. Squires Scholarship for Fundamental Research, Awarded 2019

Department of Chemistry, Analytical Division

Ohio Northern University, Ada, OH

**B.Sc. in Chemistry**

2013

GPA: 4.0

Honors: *Summa Cum Laude*

Teacher Education Program, NCATE Accredited

### PROFESSIONAL EXPERIENCE

Purdue University, West Lafayette, IN

08/2017 – 05/2018

**Laboratory Coordinator, CHM 11500**

Supervise graduate student teaching assistants for CHM 11500.

Generate all prelab assignments and keys to match learning objects for each lab.

Prepare and lead staff meetings.

Purdue University, West Lafayette, IN

08/2016 – 05/2020

**Graduate Student Teaching Assistant**

Courses Taught: Introductory Chemistry I and II, Analytical Chemistry

Taught weekly recitations and labs for 48 students each semester.

Ensured all laboratory experiments conducted by undergraduates were performed safely.

Charles River Laboratories, Ashland, OH

06/2015 – 07/2016

**Chemist III, Bioanalytical Operations/Bioanalytical Method Development**

Developed new bioassays for novel compounds using LC/MS/MS, GC/MS, GC/FID, and LC/FLD

Accurately communicated with clients about method development results.

Performed rapid validations to meet critical deadlines.

Trained new employees in data analysis and interpretation.

WIL Research Laboratories, Ashland, OH

07/2014 – 06/2015

**Chemist II, Bioanalytical Operations**

Responsible for the validation of GLP-compliant bioassays.

Troubleshoot instrument malfunctions and perform routine LC/MS/MS maintenance.

Participated in and lead process-improvement initiatives including SOP revision and maximizing the use of available cryostorage.

WIL Research Laboratories, Ashland, OH

**08/2013 – 07/2014**

**Chemist I, Bioanalytical Operations**

Performed routine chemical assays for biological samples.

Collected, analyzed, and summarized LC/MS/MS data from biological assays for Clinical and nonclinical drug trials.

Maintained compliance with GLP, EPA, and FDA regulations.

Kent State University, Kent, OH

**06/2011 – 08/2011**

**Summer Research Intern for Dr. Hanbin Mao, Associate Professor of Chemistry**

Completed chemical research funded by the National Science Foundation (grant No. 1004987)

Synthesized, extracted, and purified recombinant DNA constructs essential for studies conducted by three other researchers.

Managed primary data analysis for research that resulted in publication.

## PUBLICATIONS

1. Yu, Z.; Koirala, D.; Cui, Y.; Easterling, L.F.; Zhao, Y.; Mao, H. Click Chemistry Assisted Single-Molecule Fingerprinting Reveals a 3D Biomolecular Folding Funnel. *J. Am. Chem. Soc.*, **2012**, *134*(30), 12338-12341.
2. Dong, X.; Lu, X.; Zhang, Y.; Milton, J.; Yerabolu, R.; Easterling, L.F.; Tan, X.; Gray, M.; Kenttämäa, H.I. Investigation of the Relative Abundances of Single-core and Multicore Compounds in Asphaltenes by Using High-resolution In-Source Collision-activated Dissociation and Medium-energy Collision-activated Dissociation Mass Spectrometry with Statistical Considerations. *Fuel.*, **2019**, *246*, 126-132.
3. Niyonsaba, E.; Easton, M.; Liu, J.; Yu, Z.; Sheng, H.; Kong, J.; Zhang, Z.; Easterling, L.; Milton, J.; Kenttämäa, H.I. Identification of Protonated Primary Carbamates by Collision-activated Dissociation in Tandem Mass Spectrometry Experiments. *Org. Process Res. Dev.*, **2019**, *23*, 1159-1166.
4. Kong, J.; Hilger, R.; Jin, C.; Yerabolu, R.; Zimmerman, J.; Replogle, R.; Jarrell, T.; Easterling, L.F.; Kumar, R.; Kenttämäa, H.I. Integration of a Multichannel Pulsed-Valve Inlet System to a Linear Quadrupole Ion Trap Mass Spectrometer for the Rapid Consecutive Introduction of Nine Reagents for Diagnostic Ion/Molecule Reactions. *Anal. Chem.*, **2019**, *91*, 15652-15660.
5. Niyonsaba, E.; McKay, E.W.; Feng, E.; Yu, Z.; Zhang, Z.; Sheng, H.; Kong, J.; Easterling, L.F.; Milton, J.; Chobanian, H.R.; Deprez, N.R.; Cancilla, M.T.; Kilaz, G.; Kenttämäa, H.I. Differentiation of Deprotonated Acyl-, *N*-, and *O*-Glucuronide Drug Metabolites by Using Tandem Mass Spectrometry Based on Gas-Phase Ion-Molecule Reactions Followed by Collision-Activated Dissociation. *Anal. Chem.*, **2019**, *91*, 11388-11396.
6. Easterling, L.F.; Yerabolu, R.; Kumar, R.; Alzarieni, K.Z.; Kenttämäa, H.I. Factors Affecting the Limit of Detection for Gas-Phase Ion-Molecule Reactions in Tandem Mass Spectrometry. *Anal. Chem.*, **2020**, *92*, 7471-7477.
7. Deshmukh, S.; Easterling, L.F.; Manheim, J.; LiBretto, N.; Weideman, K.; Miller, J.; Kenttämäa, H.I.; Rakesh, A. Analyzing and Tuning the Chalcogen-Amine-Thiol Complexes for Tailoring of Chalcogenide Syntheses. *Inorg. Chem.* **2020**

### Manuscripts Not Yet Published

1. Easterling, L.F.; Manheim, J.; Kenttämäa, H.I. Towards Understanding and Utilizing Electrospray Ionization-Induced Oxidation of Sulfur-Containing Compounds in Mass Spectrometry. *In Review, Anal.Chem.*
2. Zhang, J.; Li, W.; Sheng, H.; Milton, J.R.; Easterling, L.F.; Nash, J.J.; Kenttämäa, H.I. Probing the Fragmentation Mechanisms of Deprotonated Lignin Model Compounds in Tandem Mass Spectrometry by Using Deuterium Labeling, Synthesis of Authentic Compounds, and Quantum Chemical Calculations. *In Review, Anal.Chem.*

3. Jiang, Y.; Zhang, J.; Zhu, H.; Ding, D.; Easterling, L.F.; Sheng, H.; Mazzorda, M.; Bozell, J.J.; Kenttämäa, H.I. Structural Analysis and Organosolv Process Severity Study on Switchgrass and Poplar Samples via Mass Spectrometry. *In Preparation*.
4. Feng, E.; Yu, Z.; Jiang, H.; Milton, J.R.; Hoang, T.G.; Easterling, L.F.; Ma, X.; Liu, J.K.; Nash, J.J.; Kenttämäa, H.I. Mechanistic Study on Triplet and Singlet Reactivities of Phenylcarbene. *In Preparation*.
5. Zhang, J.; Jiang, Y.; Easterling, L.F.; Anton, A.; Li, W.; Dong, X.; Bozell, J.; Kenttämäa, H.I. Compositional and Structure Analysis of Organosolv Hybrid Poplar Lignin by Using Direct Infusion Mass Spectrometry, Fast Pyrolysis Mass Spectrometry, and High-Performance Liquid Chromatography/Tandem Mass Spectrometry. *In Preparation*.